國 立 中 央 大 學

應 用 地 質 研 究 所
碩 士 論 文

Graduate Institute of Applied Geology

National Central University

Master Thesis

**Characteristics of the Chihshang Fault at Tapo-
elementary school area, Eastern Taiwan**

東台灣池上斷層於大坡國小地區的特性研究

研 究 生：費 安 托

Student: Mohammad Tri Fitrianto

指 導 教 授：黃 文 正　博士

Advisor: Wen-Jeng Huang, Ph. D.

中 華 民 國 一 百 零 九 年 六 月

June, 2020

National Central University Library
Authorization for Thesis/ Dissertation

Application Date：2020/July/29   The latest version since Sep. 2019

Applicant Name	Mohammad Tri Fitrianto	Student Number	106624604
Schools / Departments	Institute of Applied Geology	Graduate Degree	☑Master ☐ Doctor
Thesis/Dissertation Title	Characteristics of the Chihshang Fault at Tapo-Elementary school area, Eastern Taiwan	Advisor Name	黃文正

Authorization for Internet Access of Thesis/ Dissertation

This license authorizes my complete electronic thesis to be archived and read in the

• National Central University Library Electronic Theses & Dissertations System .

(✓) Released for Internet access immediately

(   ) Released for Internet access starting from: _____ / _____ / _____ (YYYY / MM / DD)

(   ) Disagree, because:_____

• NDLTD(National Digital Library of Theses and Dissertations in Taiwan).

(✓) Released for Internet access immediately

(   ) Released for Internet access starting from: _____ / _____ / _____ (YYYY / MM / DD)

(   ) Disagree, because:_____

I hereby agree to authorize the electronic versions of my thesis/dissertation and work to National Central University, University System of Taiwan(UST) and National Central Library(National Digital Library of Theses and Dissertations in Taiwan), in a non-exclusive way and without reimbursement, in accordance with the Copyright Act. The fore-mentioned authorized items can be reproduced by the authorized institution in the form of text, video tape, audio tape, disc and microfilm, or converted into other digital formats, without the limitation of time, places, and frequency for non-commercial uses.

Delayed Public Release for Paper Copy of Thesis/Dissertation
(You do not need to fill out this section if you make the paper copy of your thesis/dissertation available to the public immediately.)

• Reasons for the delayed release (choose one)

(   ) Filing for patent registration. Registration number: _____

(   ) Submission for publication

(   ) Your research contains information pertaining to national non-disclosure agreements.

(   ) Contents withheld according to the law. Please specify_____

• Delayed Until：_____ / _____ / _____ (YYYY / MM / DD)

You should submit another paper copy to National Central Library (NCL) through the NCU Division of Registrar. If you would like to delay the release of this paper copy in NCL, please fill out the "Application for Embargo of thesis/dissertation" of NCL.

Signature of the Applicant：_____   Signature of the Advisor：黃文正_____

*Please attach this form after the thesis/dissertation cover when submitting your thesis/dissertation.

National Central University

Advisor's Recommendation for Graduate Students

This thesis is by <u>Mohammad Tri Fitrianto</u> (Author) of the graduate program in <u>Institute of Applied Geology</u>, entitled: <u>Characteristics of the Chihshang Fault at Tapo-elementary school area, eastern Taiwan,</u>
which is written under my supervision, and I agree to propose it for examination.

Advisor ___黃文正___

___2020__07__16____ (YYYY/MM/DD)

National Central University

Verification Letter from the Oral Examination Committee

for Graduate Students

This thesis is by <u>Mohammad Tri Fitrianto</u> (Author) of the graduate program in <u>Institute of Applied Geology</u>, entitled: <u>Characteristics of the Chihshang Fault at Tapo-elementary school area, eastern Taiwan</u>, who is qualified for master degree through the verification of the committee.

Convener of the degree examination committee

Members

Date: __2020__07__17_____

(YYYY/MM/DD)

Abstract

Chihshang Fault is one of the most active segments of Longitudinal Valley Fault in eastern Taiwan. The Chihshang Fault is the active fault with the significant uplift rate is up to 22 mm/yr during the inter-seismic period. The previous study stated that the trace of the Chihshang Fault corresponded with the major escarpment that struck from Fuli to Wanan. Many observations had been conducted along this major escarpment to study the Chihshang Fault. One of these locations is the Tapo ES area. Pieces of evidence of surface deformation, such as the fractured concrete wall and the tilted slide platform, can be observed along the major escarpment in this area. Two boreholes were penetrated on the hanging wall and footwall of the major escarpment, respectively. However, these boreholes observation showed the continuity of the sub-horizontal layer with less evidence of significant uplift rate in between. We suspect that the upper tip of the Chihshang Fault in this area does not correspond with the the major escarpment; yet the relation between the major scarp and the Chihshang Fault will be interesting to study. Thus, to understand this phenomenon, the aim of this research is to probe the characteristic of Chihshang Fault and the relation between the Chihshang Fault with the surface deformation at Tapo ES area. We utilized 7 boreholes cores, radiocarbon (C-14) dating, Electric Resistivity Tomography (ERT), and inclinometer monitoring to support this research. In Chinyuan, 2 km to the south from Tapo ES, the Chihshang Fault has several branch faults. In this research, to differentiate the Chihshang main fault from the Chihshang branch fault, we define the Chihshang main fault as the fault with the most slip movement, which we expect to see the evidences through the structure of the rock and the inclinometer monitoring result. From the rock core, we observe the Holocene deposits that intercalate into the Lichi mélange near the boundary of these two materials. This feature is consistently observed in three boreholes. From the inclinometer, the active displacement is observed on the boundary between the Holocene deposits and the Lichi mélange. We infer that the Chihshang main fault, in Tapo ES area, separates the Lichi mélange and the Holocene deposits layer with a dip angle of 77° which the upper tip of this main fault does not correspond with the major escarpment mentioned above. Furthermore, from the insight study of the rock cores, we observe the presence of the reworked mélange near the surface with non-sheared irregular structure which indicates the result of the slumping mechanism. Thus, we infer that the recent deformation on the escarpment is affected by two mechanisms, faulting and slumping.

Keywords: Chihshang Fault, Longitudinal Valley Fault, active fault, escarpment, slumping

摘要

池上斷層是台灣東部花東縱谷斷層系列中，其中一段活動活躍的斷層，且池上斷層在震間期以約 22 mm/yr 的速率抬升，前人的研究大多認為池上斷層跡在富里至萬安地區的位置與花東縱谷及海岸山脈交界處的地形崖位置吻合，沿著此地形崖處已有許多與池上斷層相關的研究，其中一個被探討已久的地方位於大坡國小，沿著此地形崖可觀察到多個近地表正在變形的證據，像是破裂的水泥牆及變形而傾斜破壞的溜滑梯，然而，根據地形崖兩側前人認為是池上斷層上盤及下盤處的兩口鑽探岩心分析，兩口岩心層序可完全對比，且層界近乎水平，並無證據顯示池上斷層通過此處，原本預期池上斷層頂端與的形崖的位置並不吻合，因此池上斷層的位置與地形崖之間的關係是個有趣且值得被探討的問題。本研究目的為釐清此地區池上主斷層的特徵，以及釐清大坡國小內近的表變形與池上斷層之間的關係，本研究利用 7 口鑽探資料、碳十四定年、地電阻剖面資料及傾斜儀監測資料進行分析，前人研究在大坡國小南側 2 公里處觀察到池上斷層有分支斷層，為了區別主斷層與分支斷層，本研究定義池上主斷層為錯移量最大的面，此位置本研究也預期會在岩心當中以及傾斜管監測資料看見相對應的證據，根據 3 孔鑽探岩心分析結果，本研究觀察到個別在不同深度觀察到全新世沉積物與利吉混同層攪和在一起，傾斜儀監測資料也可觀察到位於全新世沉積物及利吉混同層交界處有明顯位移量，本研究定義池上主斷層為岩心中觀察到最後一塊利吉層與全新世沉積物不連續接觸面，3 孔岩心主斷層連線計算出的斷層面傾角為 77 度，主斷層頂端的位置與地形崖的位置並不一致。本研究亦藉由岩心分析，觀察到近地表處利吉混同層有非剪切構造的不規則構造，意味著利吉層有重新堆積的現象，此現象指示此區有崩移的機制，因此本研究推論地形崖處近地表變形受兩種機制影響；斷層錯移及崩移。

關鍵字：池上斷層、花東縱谷斷層、活動斷層、地形崖、崩移

Acknowledgments

The author thanks to Prof. Huang, Wen-Jeng as the advisor. He is the person who willing to spend his time, energy, and wealth to support this research. He is the person who wisely give the author many advices related to the research. He is the person who willing to share his knowledges and to discuss with the author. He is the person who always share his life experience so the author can take a lesson and become a better person.

The author thanks to Dr. Huang, Senior Research of CPC and Dr. Huang from Taichung National Museum. They willing to provide the time to discuss about rock cutting and provide a very good quality of rock scanning.

The author thanks to Yi-Wei for assisting author during the field survey.

The last but not the least, the author want to thanks to parents, wife, and friends who always pray for and support the author. The author really wants to share this achievement with them.

Table of Content

List of Figures

List of Tables

Chapter 1: Introduction

1-1 General description of Chihshang Fault

Chihshang Fault is one of the most active faults in eastern Taiwan. Mu et al. (2011) stated that Chihshang Fault produces two types of movement: co-seismic movement and inter-seismic movement. The co-seismic movement corresponded to the 1951 Chihshang Earthquake (Mw = 6.2) and Chengkung Earthquake (Mw = 6.5) (Cheng et al., 1996; Chen et al., 2005). Based on study of paleoseismology, Yen et al. (2014) stated that the approximated recurrence of this fault is about 50-110 years. Meanwhile, during the inter-seismic period, the movement of Chihshang Fault was recorded with an uplift rate of about 20 mm/yr (Yu & Liu, 1989; Hsu et al., 2018).

Based on the geological map of Taiwan Central Geologic Survey (2000), the Chihshang Fault juxtaposes the Lichi formation and terrace deposits in the south part, and transverse within the alluvium in the north part (Fig. 1.1). Chang, Q. (2012) stated that Xinwulyu River was the main factor of alluvial deposits to spread over the Longitudinal Valley. Xinwulyu River is one of the rivers that come from the Central Range. So, the deposits of this river would share a common characteristic with the formation in the Central Range, such as Pilushan Formation: slate, phyllite, quartzite; and Tananao Schist.

Based on the DEM map (Fig. 1.2), we also could learn that the major radial shape of the contour-line indicates the alluvial fan of the Xinwulyu River. From this major radial shape, the Xinwulyu River deposits almost covered the entire valley. Tributaries from the Coastal Range also supposedly have some contributions as deposits supplement on the valley area, albeit it is not as major as Xinwulyu River. Considering the Coastal Range contribution, the deposits with the characteristics of the formation of the Coastal Range also might present in the valley. These formations are Lichi formation: mélange with various type of rock clast; Tuluanshan formation: sandstone, agglomerate; and Takangkao formation: sandstone, conglomerate (Chai, B. H. T., 1972).

Morphologically, the major geomorphic scarp is marked by the uplifted terrace 3 to 6 m on the east of the Chihshang township. It extends north-northeastward to Fuli and south-southwestward to Chinyuan, attaining a total length of some 10 km. The terrace is composed of the Miocene Lichi formation, which belongs to the Coastal range (Hsu, T. L., 1962; Chai, B. H. T., 1972). On top of it, terrace deposits cap the Lichi formation (Hsu T. L., 1962). From the field observation, Chang, Q. (2012) found that the terrace has two parts: terrace gravel deposits

and uppermost secondary deposits. The terrace gravel deposits are composed of metamorphic rock gravels and lenticular coarse sand layer derived by the Xinwulyu river from the Central Range. Meanwhile, the secondary deposits, overlying the terrace gravel deposits, are composed of either sandstone gravels derived from the Coastal Range or fine-grain silt and clay. Based on a comprehensive analysis of the formation distribution and the surface deformations, it indicates that the escarpment is a tectonic scarp of the Chihshang Fault (Hsu, T. L., 1962; Jiang et al., 2012).

1-2 Tectonics of Taiwan

In 1951, there were recorded three major earthquakes in different locations in eastern Taiwan. The shake of these earthquakes corresponded with the development of surface faults. These surface faults are Chihshang Fault, Milun Fault, and Yuli Fault (Hsu, T.L., 1962). In the geological map (Fig. 1.1), these faults are indicated by a red line. The Chihshang Fault is one of the long-lineament segments of the major fault that traverse from Hualien to Taitung. This long-lineament is well-known as the Longitudinal Valley Fault (hereafter referred to as LVF).

The tectonic setting of Taiwan is the major reason for the high tectonic activity along the LVF. Taiwan is located on the boundary of the collision between the Eurasian Plate and the Philippine Sea Plate (Biq, C.C., 1972). The LVF mentioned above represents the suture of these two major plates (Fig. 1.3) (Angelier et al., 1997; Lee et al., 2001). The collision rate between the Eurasian Plate and the Philippine Sea Plate is about 82 mm/yr (Yu et al., 1997). This significant collision rate results in frequent tectonic activity along the LVF, especially the Chihshang Fault.

1-3 Review of Chihshang Fault activities related to the major geomorphic scarp

The Chihshang Fault is one of the most active faults in eastern Taiwan. The result of long-term vertical slip showed that the uplifting of the Chihshang Fault during the past seven thousand years was around 1.4-1.7 mm/yr, while the present was around 2.5-3.0 mm/yr (Chang, 2013). Paleoseismic studies of the Chihshang Fault suggested that a cluster of up to six moderate earthquakes (M6-7) had occurred in the past 800 years (Yen et al., 2014). In one of the cases during the 1951 Taitung earthquakes, several fractures were generated in the ground and buildings along the trace of Chihshang Fault. However, during the interseismic period, the

fractures were kept developing (Angelier et al., 1997). In the 1980s, Yu and Liu (1989) reported evidence of vertical active creep of the Chihshang Fault based on the leveling data from 1986 – 1988 (Fig. 1.4). Compared to the morphology, the result of the leveling study was consistent with the major geomorphic scarp near Chihshang township. The significant uplift rate, of about 21 mm/yr, was observed between two benchmarks, each of which is located on the west and east side of the geomorphic scarp at Tapo.

Until then, the aforementioned uplifting still consistent with the more recent geodetic data from 2007 to 2015. The recent geodetic data showed that the western margin of the Coastal Range, east side of the geomorphic scarp, was uplifted of about 22 mm/yr with respect to the Longitudinal Valley, west side of the geomorphic scarp (Hsu et al., 2018).

1-4 Review of Chihshang Fault characteristics along the geomorphic scarp

Several geological surveys had been conducted in different locations along the escarpment of the Chihshang Fault. Based on these surveys, the Chihshang Fault has different characteristics in different locations, those are Fuli, Chinyuan, Wanan, and Tapo (Fig. 1.2).

In Fuli, there is an outcrop of the Chihshang Fault on the riverbank. Based on the outcrop observation, the Chihshang Fault was defined as Lichi mélange that was thrust westward over the Quaternary gravel with a dip of 60° E (Yu et al., 1994) (Fig. 1.5a). Chang et al. (2001) did some field observations to study the structure of the Lichi mélange at Fuli, around Bieh river. From this observation, they described the Lichi mélange as a strongly sheared mud material that has striated scaly foliations with a regular orientation (Fig. 1.6).

In Chinyuan, Mu et al. (2011) drilled three boreholes. Based on the analysis of the borehole cores, they observed three-branch faults of the Chihshang Fault in the alluvial deposits with different dip angles. By comprehensive geodetic analysis and fault kinematics, the frontal branch fault of Chihshang Fault has a dip angle of 34° E – 42° E, which corresponds to the surface main geomorphic escarpment (Mu et al., 2011) (Fig. 1.5b).

In Wanan, three boreholes were drilled following a line perpendicular to the strike of the Chihshang Fault (Chen, W. S., 2008). Based on cores analysis of these boreholes, the Chihshang Fault is characterized as a sharp fault zone with a dip of about 65° E separating Lichi mélange in the hanging wall and alluvial deposits in the footwall (Chen, W. S., 2008) (Fig. 1.5c).

In Tapo, specifically at Tapo Elementary School area, two boreholes had been penetrated on the hanging wall and footwall with respect to the main geomorphic scarp (Taiwan

CGS, 2018) (Fig. 1.7a). Based on the observation of these two borehole cores, two lithologic units were identified: the alluvial layer with andesitic and sandstone gravel and alluvial layer with metamorphic gravel. The andesitic alluvial layer is the uppermost layer that supposedly derived from the Coastal Range with intercalating of thin fine-grained sandy layer. Two dating data of this alluvial layer had been obtained: 1390 to 1415 Cal BP at depth of about 7 m relative to the valley surface level, 1880 to 1820 Cal BP at depth of about 15.85 m relative to the valley surface level (Fig. 1.7b). Meanwhile, the alluvial layer consisting the metamorphic gravel and coarse sand layer is supposedly derived from the Central Range. The lithologic contact between the alluvial layer sourced from the Coastal Range and the alluvial layer sourced from the Central Range was observed in both two boreholes. However, from the core correlation, they found the vertical throw of this lithological contact of about 1.5 m. If the Chihshang Fault presence in between these two boreholes, supposedly, the vertical throw of the lithological contact has higher magnitude than what has been observed from the two boreholes. The vertical throw should be about 39 m by assuming the uplifting already started since the deposition of the alluvial layer sourced from the Coastal Range (about 1800 yr BP) and uplift rate from Hsu et al. (2018) of about 22 mm/yr.

1-5 Aims and structure of this thesis

With the active movement during co-seismic and interseismic period, the Chihshang Fault might produce significant hazard in the eastern Taiwan. Therefore, we aim to study about this fault, especially at Tapo Elementary School (hereafter refer to Tapo ES) area. This school is located right next to the major geomorphic scarp that has been inferred as the tectonic scarp of the Chihshang Fault. Moreover, some school facilities: slides, stairs; were built traverse this major scarp. Tracing this main fault will be one of the important things to assess the hazard of the area in the future. However, the study of the two boreholes by Taiwan CGS (2018) barely gives us any clues about the presence of the Chihshang main fault, yet give us encouragement to study further about its characteristics. This thesis aim is to probe the characteristic of the Chihshang main fault at Tapo. Several surveys, such as field observation, boreholes coring, Electric Resistivity Tomography, inclinometer monitoring, and C^{14} dating, were conducted to reach this aim.

This thesis consists of four chapters: (1) Introduction; (2) Data Description; (3) Methodology and Results; (4) Discussion and Conclusions. The Introduction briefly presents an overview of the geological setting of the Chihshang Fault and its activities. The data

description will describe the data collection from all related surveys. Methodology and results will describe the methods used for processing the data along with the main results. Discussion and conclusions will interpret the character of the Chihshang main fault activities at Tapo based on cores observation, C^{14} dating data, 2D resistivity tomography, and inclinometer monitoring.
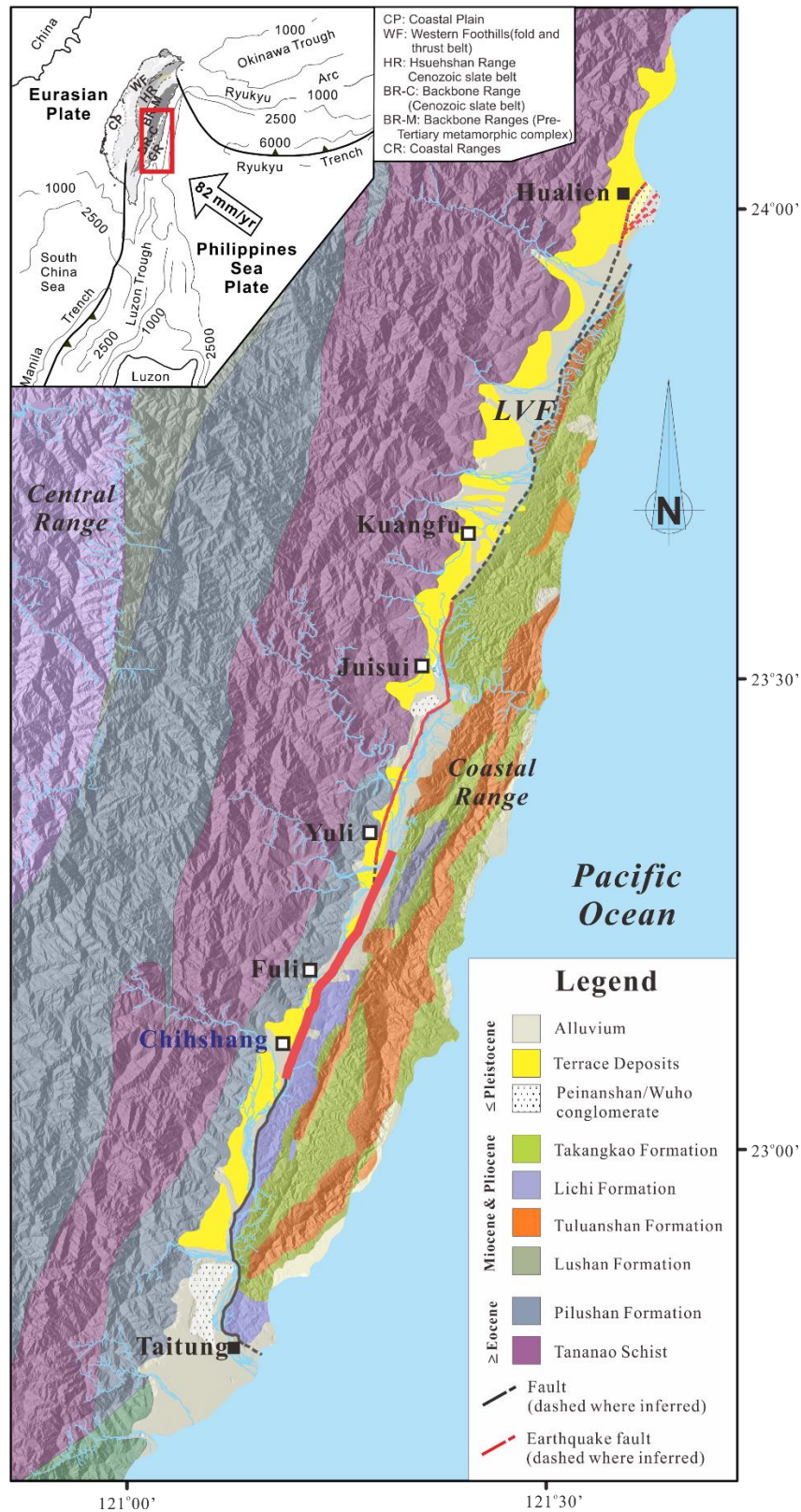
Figure 1.1 Map of southeast Taiwan showing the geological setting (modified from Taiwan geologic map on scale of 1 to 500000 by TCGS, 2000) along with the inset map of Tectonic setting of Taiwan. Red rectangular on the inset map highlights the southeast Taiwan. Chihshang Fault is indicated by red bold line (Shyu et al., 2007).
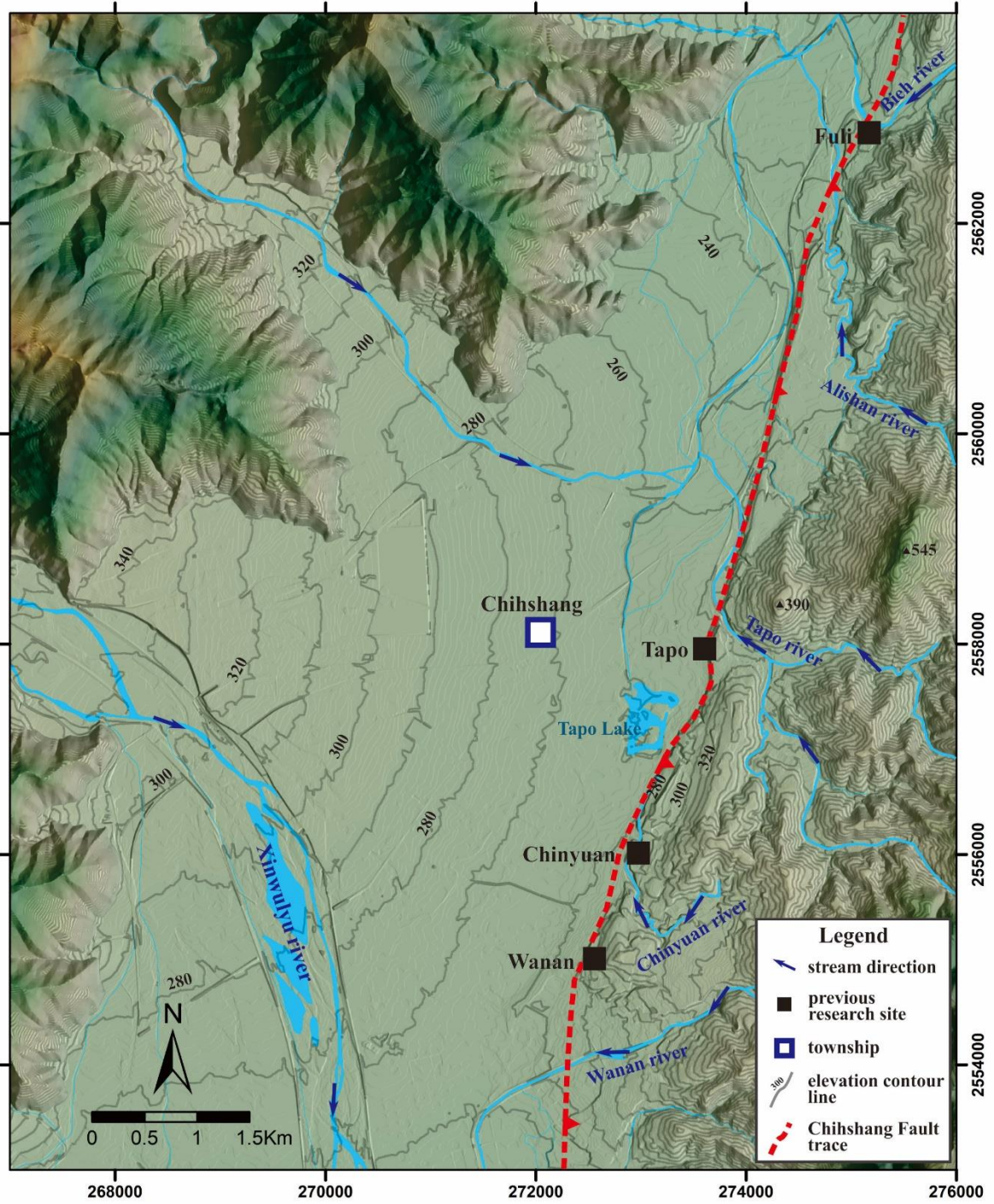
Figure 1.2 Topographic map of Chihshang based on 5m DEM along with previous research site locations of Chihshang Fault. Red dashed-line indicates the Chihshang Fault trace (from Jiang et al., 2012).
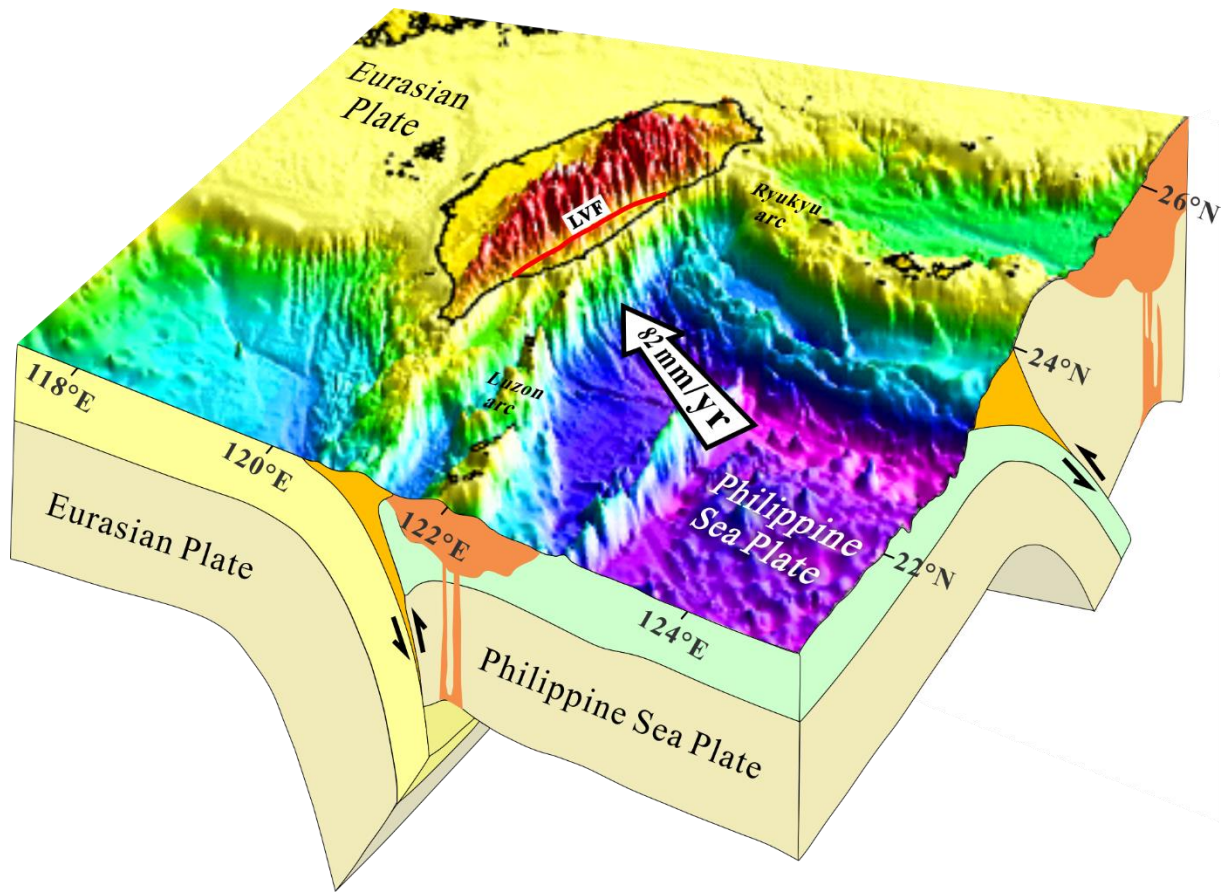
Figure 1.3 Diagram of tectonic setting of Taiwan (modified from Tseng, Y. C., 2019).
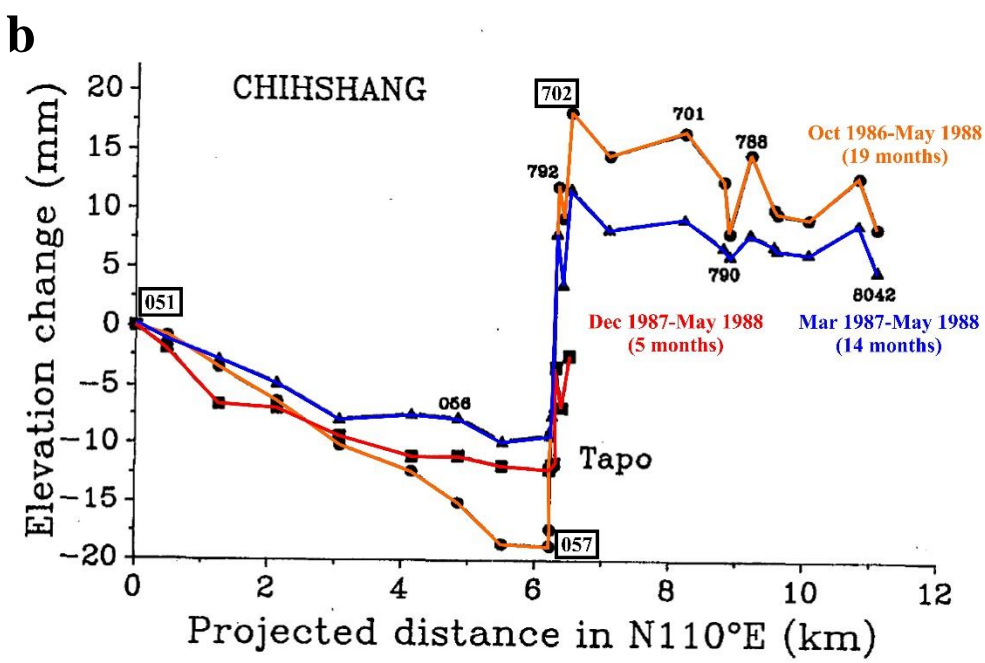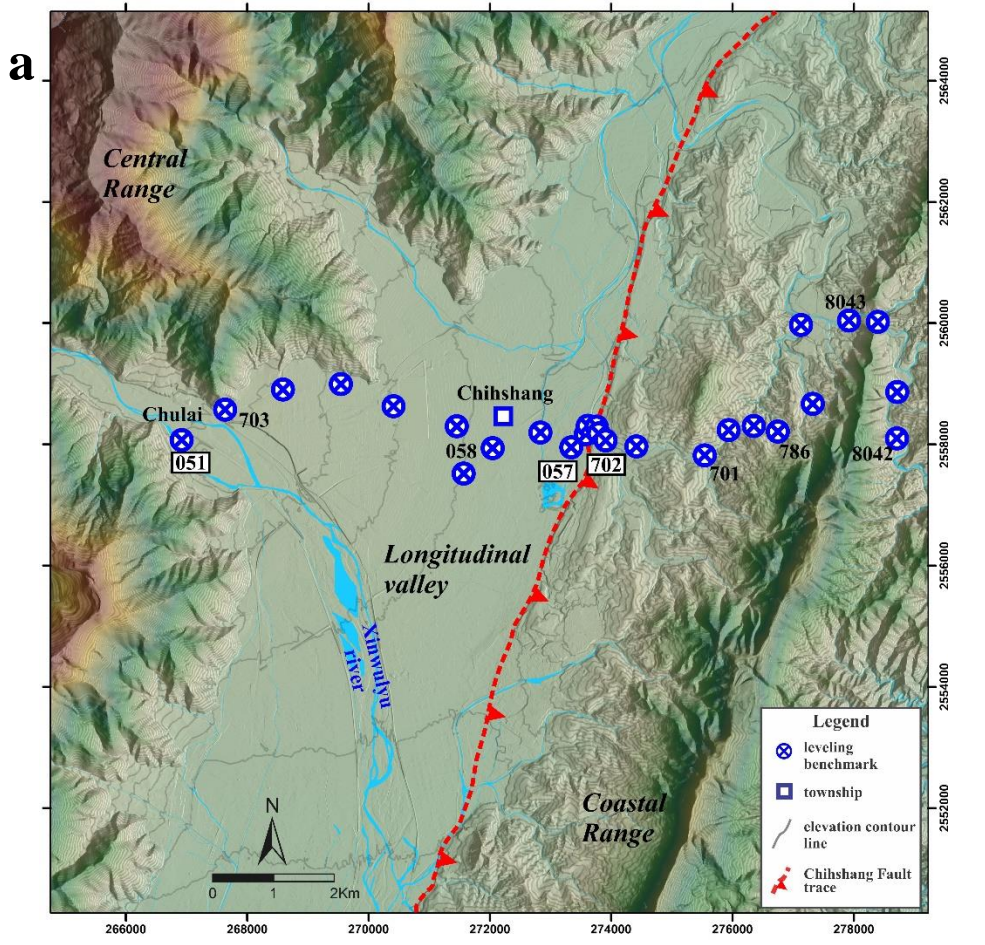
Figure 1.4 Results of leveling measurement at Chihshang (modified from Yu & Liu, 1989). (a) Leveling route at Chihshang. Red dashed-line indicates the Trace of the Chihshang Fault (adapted from Jiang et al., 2012). (b) Elevation changes of bench marks relative to BM 051 during 1986 to 1988 (modified from Yu & Liu, 1989).

a

5 m

East   West

b

WNW   T1   T2   ESE

0   20   40   60   80   100   120   140   160

0

-10

-20

depth (meter)

-30

-40   Alluvial
                   deposits

-50

-60   ?   Lichi
                                                                          mélange
-70

-80

-90

-100
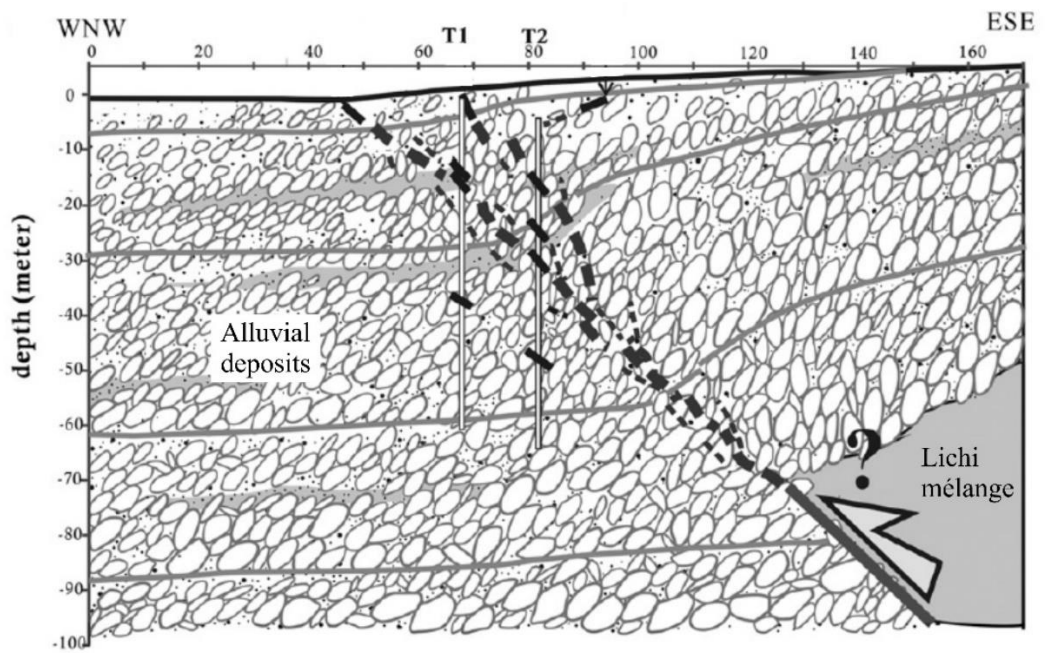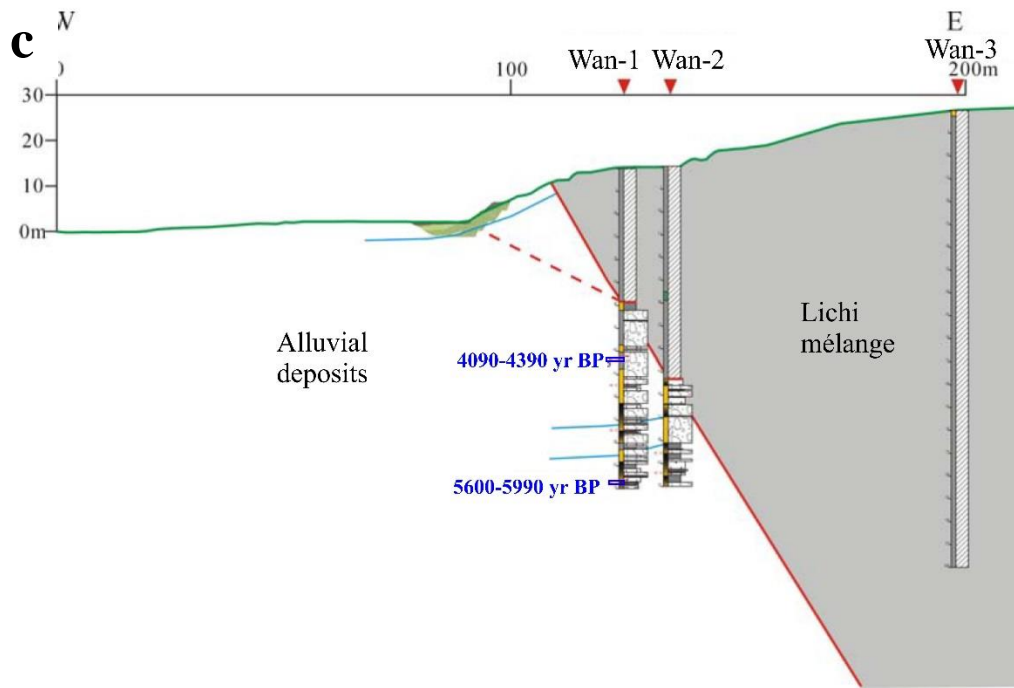
Figure 1.5 Chihshang Fault architecture at three research locations (Fig. 1.2). (a) Outcrop of Chihshang Fault at Fuli (after Yu et al., 1994). The Lichi mélange, in the east side, thrusted over the Holocene deposits, in the west side. (b) Chihshang Fault architecture at Chinyuan site (from Mu et al., 2011). (c) Chihshang Fault architecture at Wanan site (after Chen, W.S., 2008).
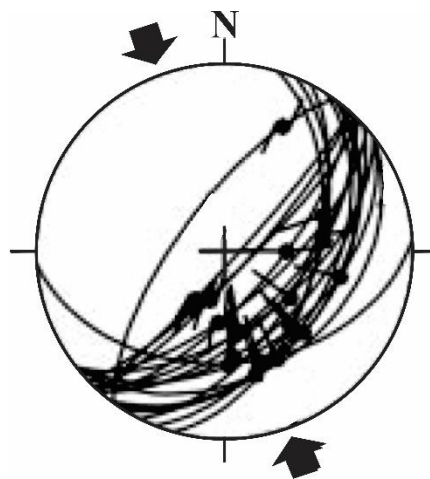
Figure 1.6 Stereographic plot of striated scaly foliations measured in Fuli, around Bieh River area. Thin curves with dots indicate striated fault attitude. Dot with inward directed segment indicates reverse slip. Dot with outward directed segment indicates normal slip (after Chang et al., 2001).
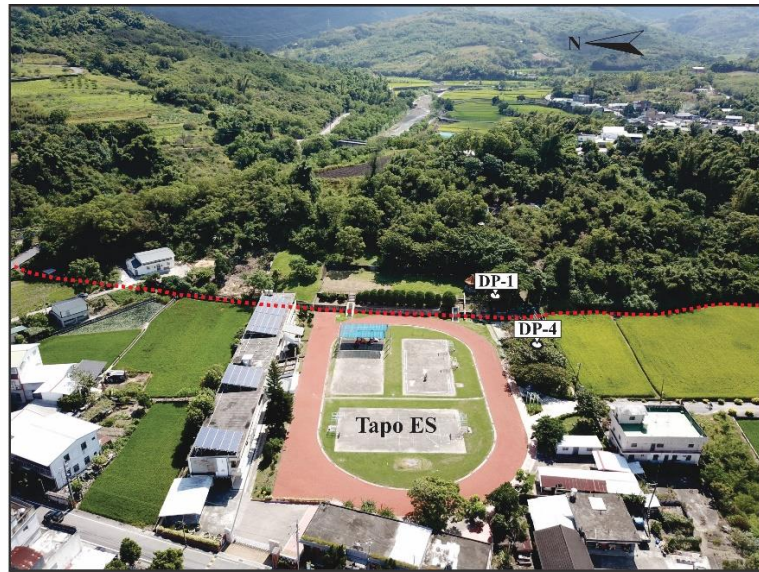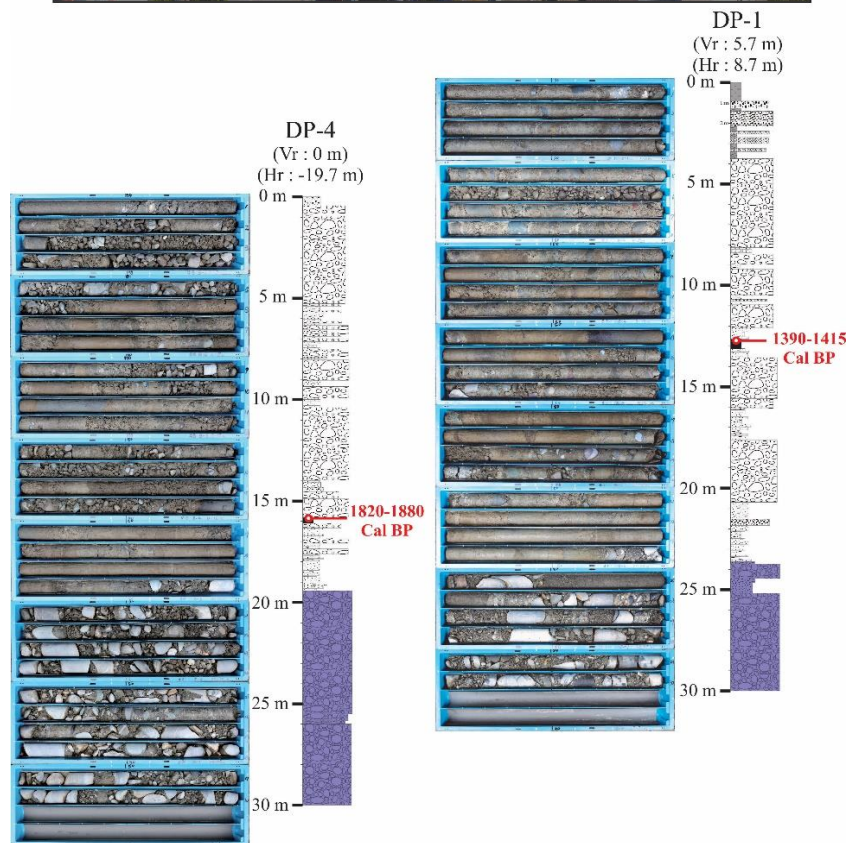
Figure 1.7 Boreholes at Tapo Elementary School (TCGS, 2018). (a) Oblique view of Tapo Elementary School (Tapo ES). Red dashed-line indicates major geomorphic scarp. White circle with label indicates the borehole location. (b) Core image along with the core logs. Vr indicates the relative elevation of the upper end of the borehole with respect to the surface level of the Tapo ES yard. Hr (+) indicates the relative horizontal distance of the borehole from the toe of the major geomorphic scarp to the east. Hr (-) indicates the relative horizontal distance of the borehole from the toe of the major geomorphic scarp to the west. Red label indicates the calibrated dating data from the organic sediment that was obtained from the core.

Chapter 2: Methodology

2-1 Field survey

In the early period of this research, we conducted field survey to observe several aspects related to geomorphology and geology. Our main objectives on this field survey are to observe the major escarpment related the Chihshang main fault activity, observe the surrounding outcrops, and analyze the rock cores which we described in the following chapter. We utilized several items, such as hoes, geologic hammer, camera, and Unmanned Aerial Vehicle (UAV) drone.

We utilized the DJI Mavic pro UAV drone to capture the aerial view. It has a cruising range of 7 Km, four vision sensors, a camera with 4K resolution (3840 x 2160 pixels), and 3-axis mechanical gimbal. It supported us in observing the lineation of the escarpment and other morphological conditions around the research area.

Based on the observation along the escarpment at Tapo ES area, we described that the strike of this escarpment was about N28^{o}E with the vertical distance between toe and tip of the escarpment was about 1.5 m. We hardly observed the material along the escarpment, since it was covered by the concrete wall. However, along this concrete wall, we could clearly observe some evidences of deformation.

We also observed the hill area westward from the escarpment (hanging wall). The ground of this hill area mainly consists of mélange material with some clasts of rocks. On the top of the hill, we found sediment deposits such as gravel and fine-grained sand layers. Further observation results are described in the following chapter.

2-2 Electric Resistivity Tomography (ERT)

We utilized the ERT method to image the subsurface structures in Tapo ES area. Two ERT survey lines were deployed perpendicular to the escarpment orientation (Fig 2.1). The detailed description of this measurement is provided by Chang et al. (2018) in their paper. Furthermore, the ERT survey data has been processed by Professor Chen, C.C., National Central University (2016). From this processing of resistivity data, we obtained the inverted resistivity model along the aforementioned survey line (Fig 2.2).

Based on the inverted resistivity model (Fig 2.2), we observed the resistivity value of the research area in the range of between 3 Ω-m - 300 Ω-m. In general, the result of two ERT

survey lines share a common characteristic. The high-resistivity value (>20 Ω-m) tends to distribute on the west side, while the low-resistivity value (<9 Ω-m) is distributed on the east side of the model and on the top of the high-resistivity area mentioned before. In between low-resistivity area and high-resistivity area, we considered as the resistivity gradation zone with the value ranging of between 9 Ω-m - 30 Ω-m.

The resistivity is a physical property of a material that represents the ability to resist the electric current to pass through. This resistance ability would be related to some other properties, such as water content, mineral content, and porosity. The high-water content in a rock might be enough to make a significant anomaly of low resistivity in the resistivity model. For example, dry sandstone would have relatively high resistivity value compare to the wet sandstone (Telford et al., 1990). Another property, such as porosity, should be in consideration as well. The material with low porosity, such as mudstone, would be easier for electric current to pass through; compare to the material with higher porosity such as sandstone. Based on this basic knowledge, the variations of resistivity value in our study would be representative of the variety of rock characteristics.

Although the general condition of both ERT results share a common characteristic, we still could observe some differences in some part of the inverted resistivity model between ERT 1 and ERT 2. In the resistivity model of ERT 2, the low-resistivity value distributes near the ground surface from DP-4 to DP-1; while in ERT 1, the low-resistivity value only distributes beneath the escarpment. The distribution characteristic of this low-resistivity value would be related to the presence of the running water in the gulley on that area. For the ERT 1 case, the gulley is transverse on the foot of the escarpment perpendicular with the ERT 1 survey line. This setting might correspond to a narrow area of low-resistivity value beneath the escarpment as showed in the resistivity model of ERT 1. Meanwhile, for the ERT 2 case, the gulley heads to the west from the foot of the escarpment parallel with the ERT 2 survey line. This setting corresponds to a long distribution of low-resistivity area near the ground surface.

These ERT results supported us in providing the possible image of the subsurface structure and to plan the borehole location in the research area. Afterward, this ERT result would be integrated with the borehole core data to approximate the detailed subsurface structure image.

2-3 Core analysis

In total, we collected cores from seven boreholes: the four boreholes, DP-1, DP-4, DP-6 and DP-7, are from Taiwan CGS (2018) and Chang et al. (2018); the rest three boreholes, DP-7A, DP-7B, and DP-8, are the most recent boreholes. The objective of core analysis is to get the comprehensive subsurface structure information in the area, including the trace of the Chihshang main fault. To achieve this objective, these boreholes are located fairly along the line perpendicular to the major scarp (Table 2.1) (Fig.2.1) and parallel to the ERT survey lines.

We hired two experienced engineers to operate the drilling machine and to help us collect the cores (Fig.2.3). The drilling process was time-consuming because it was dependent on the weather condition and type of subsurface material. Each core was taken out from the borehole in every one-meter length by the drilling machine. This core was taken out in wet conditions, so we had to wait a few minutes until the core was a little dry before did further step of analysis. After the drying, we scratch tiny part the core surface to clean the core from the dirt that might adhere during the core taking process. Based on core observation, we generally classified three distinct lithologic units: the Lichi mélange, the alluvial layer which consist of intercalation between the andesitic gravel layer with the fine to very fine sandy layer, and the alluvial metamorphic gravel layer.

Furthermore, to advance the result of observation, we bisected some cores parallel with the cylindrical core axis to observe the inner part of the core. This bisecting procedure was conducted to confirm whether the rock structure that we observed from the cylindrical core surface was consistent with this bisecting core surface or contrary.

Table 2.1 Boreholes specification at Tapo ES.

Name of the borehole	Coordinate (TWD 97)		Elevation of the borehole upper end	Depth of borehole
	X	Y	(m)	(m)
DP-1	273653	2558124	274.2	30
DP-4	273625	2558126	268.5	30
DP-6	273689	2558107	280.4	28
DP-7	273686	2558108	279.7	16
DP-7A	273703	2558102	287	82
DP-7B	273696	2558105	283.6	50
DP-8	273698	2558104	283.6	32

2-4 Radiocarbon dating (^{14}C)

The presence of the fault commonly can be identified by the nonlateral continuity of a layer. Core correlation among the boreholes is one of the methods that we did to trace this nonlateral continuity. However, sometimes the fault would be hard to trace from the core correlation; especially, while the hanging wall and footwall have a common characteristic material; for instance, the Chihshang Fault, which was discovered within the Holocene deposit in Chinyuan site. Therefore, the absolute dating methods would be necessary to comprehend the tracing of the continuity of the layer among the boreholes. Since the Chihshang fault has a significant uplift rate, supposedly, we could find a significant difference of age from one borehole to the others.

There are several absolute dating methods: Dendrochronology, Radiocarbon (^{14}C), Uranium-Thorium (U-Th), Luminescence, Cosmogenic exposure. As we learned from the references, our study area is almost covered by the alluvial deposits with the Holocene age. The Radiocarbon (^{14}C) dating would be the one of the methods that could cover the require age, yet convenience to use. Thus, we sampled some organic sediment and charcoals from the cores for this dating method. Afterward, these samples were processed by Beta Analytic Radiocarbon Dating Laboratory to obtain the dating data along with the calibrated data.

2-5 Inclinometer monitoring

2-5-1 General description of inclinometer data

We utilized one unit of Shape Accel Array Field (SAAF) Inclinometer (Fig.2.4) to monitor the subsurface deformation by installing it into the borehole. SAAF is a string of rigid segments separated by flexible joints. The total length of SAAF that we utilized is 10 m with the length of each segment is 0.5 m. In each segment, it has the Micro Electro Mechanical Systems (MEMS) sensor, which can measure the tilt angle relative to gravity's direction (Fig. 2.5a and 2.5b). By applying the triangular formula, the tilt angle could be transformed into the horizontal displacement magnitude (Fig. 2.5c) (adapted from Measurand Company, 2017). With the length of a segment is of 0.5 m, the horizontal displacement can be obtained by

$$d = 0.5 \times \sin(\theta), \tag{2.1}$$

where d is the horizontal displacement in meter, θ is the tilt angle of the sensor relative to the gravitational force orientation. Based on this concept, we could get the horizontal displacement, North-South and West-East, at every 0.5 m in 10 m-length.

16

We did the inclinometer monitoring in two boreholes at different times. In DP-7, we did the inclinometer monitoring from 6 May 2016 to 10 October 2018 with the sampling rate of 5 minutes. In DP-8, the monitoring was conducted from 19 October 2018 to 3 March 2020 with the sampling rate of 10 minutes. The inclinometer was linked to the internet; therefore, the data could be download in a privy website.

2-5-2 Data processing

As we had mentioned previously, the inclinometer monitoring data were the horizontal displacement magnitude in every half-meter. Supposedly, the data would be started from zero since there should be no displacement recorded at the beginning of monitoring. In fact, the initial data has a particular value. By assuming there are no movement on the first-time measurement, we could perform the data by

$$X_{i,j} = x_{i,j} - x_{1,j}, \qquad i = 1, 2, 3, \dots, n \ ; \ j = 1, 2, 3, \dots, 21 \tag{2.2}$$

where $X_{i,j}$ determines the corrected data, $x_{i,j}$ determines the magnitude of horizontal displacement, i determines the order of data in the matter of time, n determines the total measurement data of a specific depth level, and j determines the order of data in the matter of depth level. The length of our inclinometer instrument is 10 meters with a measurement point in every half-meter, so totally, we have 20 measurement points and 1 reference point, which is represented by j in the formula. After this correction, the data was ready to perform in a graph.

By analyzing the trend of the time series versus displacement difference graph, we observed several data that had significant movement during the first monitoring period. This anomaly data was observed at all depth levels. One of the possibilities, this anomaly might be the result of the borehole recovery effect. So, we cut about the first-month monitoring data to minimize the influence of the borehole recovery effect. In final, we preserve the inclinometer data of DP-7 from 6 June 2016 to 18 October 2018 and DP-8 from 11 November 2018 to 3 March 2020. Afterward, we did the shifting again by utilized equation 3.2.

We observe another possible error that we found in the inclinometer monitoring data for every half meter depth. We found a jump displacement magnitude in one inclinometer axis within five minutes-data; however, there is no significant displacement in another axis. We argue that it would relate to the systematical error. To discover this error, we had to observe the data by screening the graph of time series versus displacement difference for every half-meter depth. The time series versus displacement difference graph could be obtained by

$$\Delta X_{i,j} = x_{i,j+1} - x_{i,j}, \qquad i = 1, 2, 3, \dots, n \ ; \ j = 1, 2, 3, \dots, 21 \tag{2.3}$$

where $\Delta X_{i,j}$ determines the displacement difference between two adjacent measurement points, i determines the order of data in a matter of time, n determines the total measurement data of a specific depth level, and j determines the order of data in the matter of depth level.

Figure 2.1 Bird view image of research area along with configuration of Electric Resistivity Tomography (ERT) survey line and boreholes.
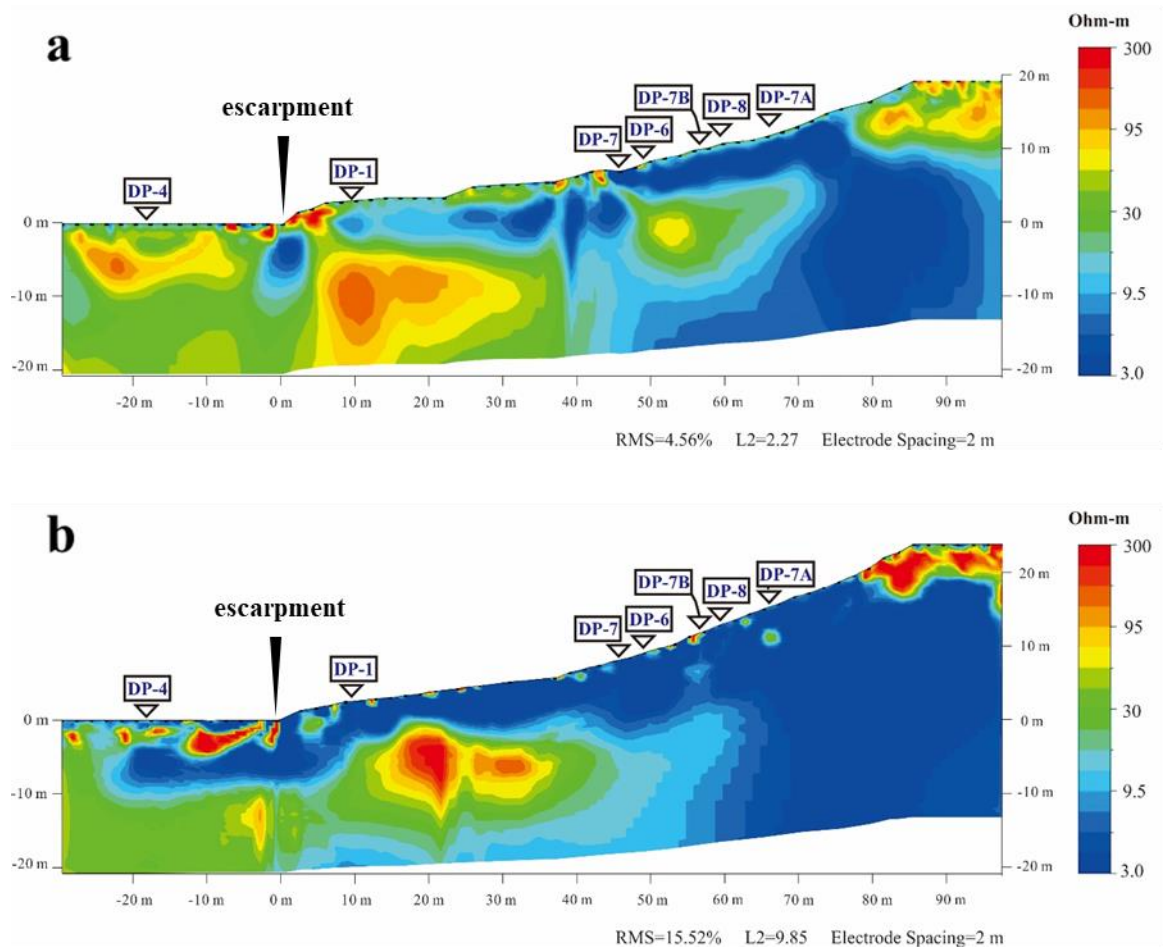
Figure 2.2 Resistivity section (TCGS, 2018). The white triangle indicates the location of the upper end of the borehole. The x-axis indicates the relative distance to the escarpment. The y-axis indicates the relative elevation to the toe of the escarpment. (a) Inverted resistivity model of ERT 1. (b) Inverted resistivity model of ERT 2.

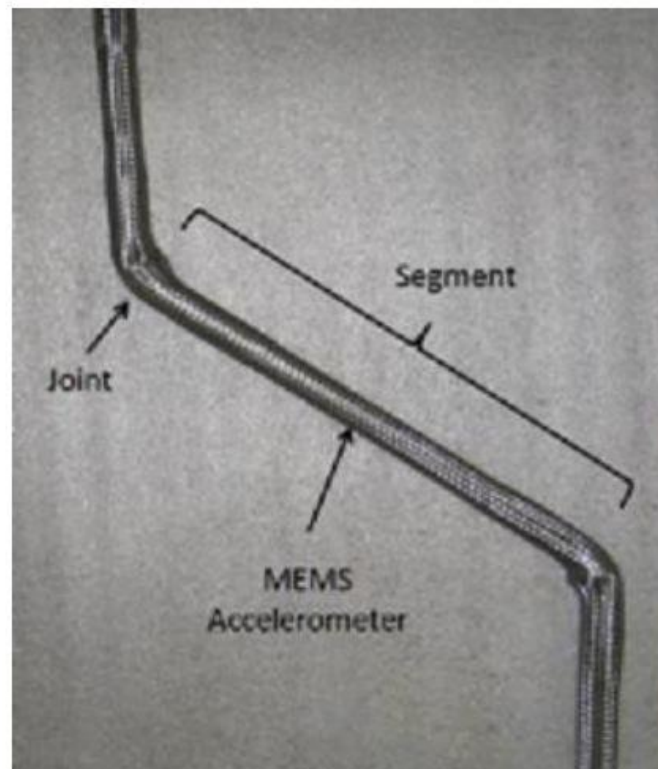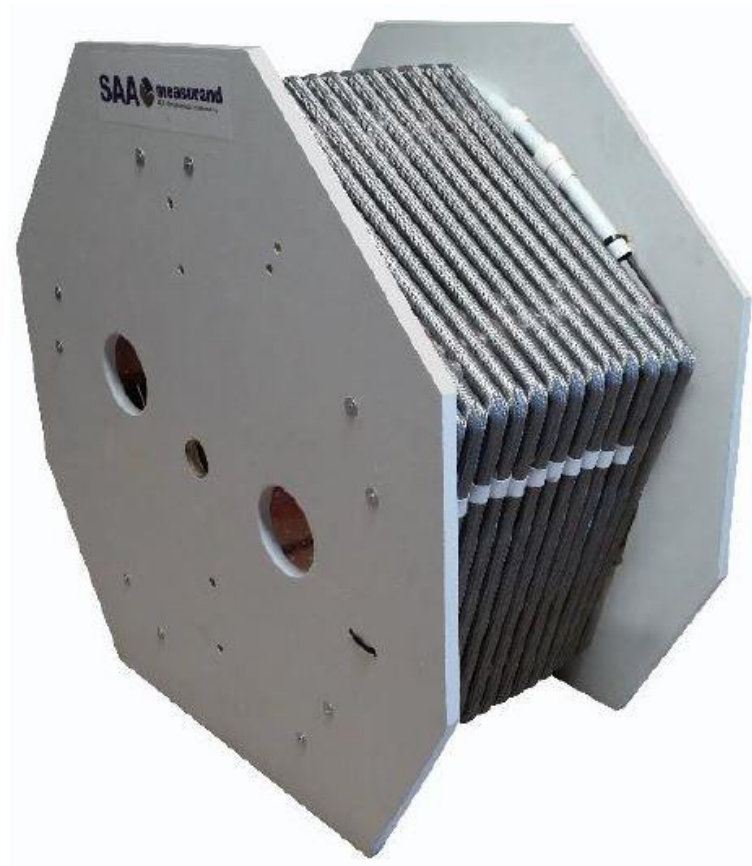Figure 2.3 Photograph of the operation of the drilling machine.

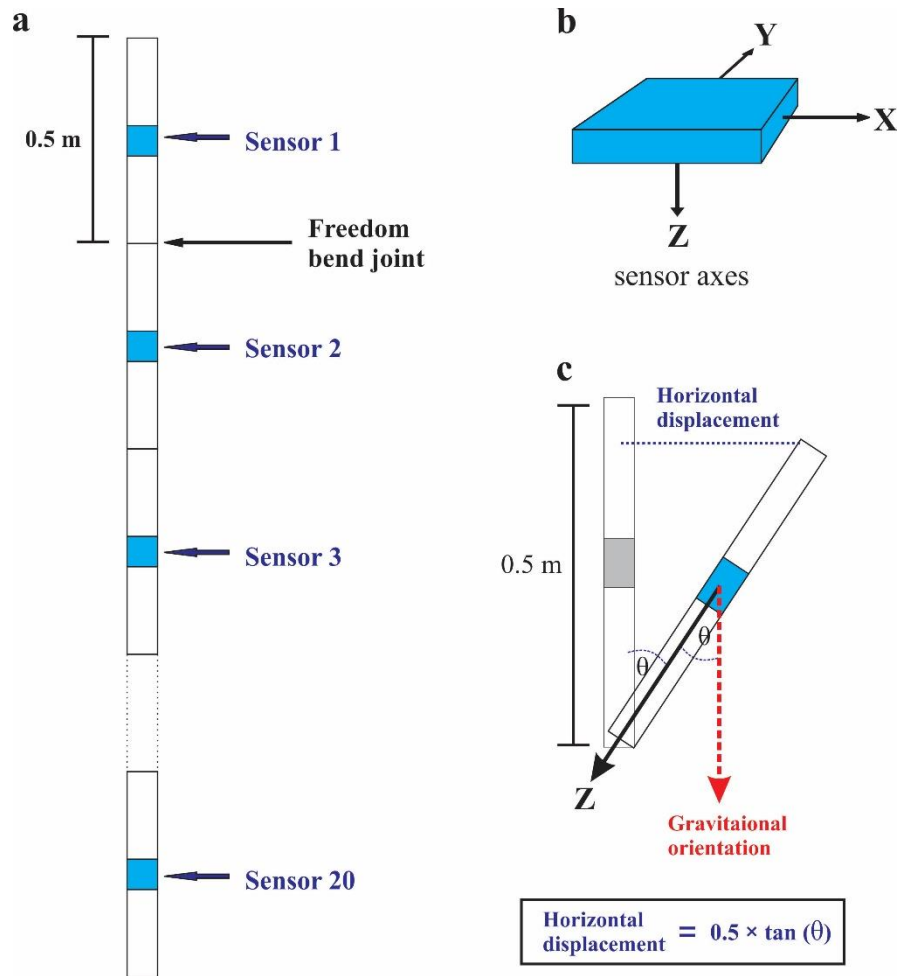Figure 2.4 Image of SAAF inclinometer (Measurand Company).

Figure 2.5 Principle measurement of SAAF inclinometer (adapted from Abdoun et al., 2007). (a) Schematic of SAAF arrangement. (b) Sensor axes: X and Y are the horizontal axes; Z is the vertical axes. (c) Principle of displacement measurement by SAAF (adapted from Measurand Company, 2017).

Chapter 3: Results

3-1 Field survey

3-1-1 Damaged man-made structures

At Tapo ES, the concrete wall was built along the major escarpment related Chihshang Fault activity. We confirmed several damages along this wall. In the south part of the Tapo ES area, the upper half-part of the concrete wall seemed to be popped out (Fig 3.1b). While in the north part of the Tapo ES area, a part of the concrete wall has been torn apart (Fig. 3.1c). There is a particular man-made structure built on both of damaged concrete wall. We conceived that this man-made structure was built to withstand the more extensive damage that might occur in the future.

Meanwhile, right above the damaged wall, the platform of a slide has been tilted (Fig. 3.1b). The slide was built by straddling the escarpment, until then it deformed due to ground movement. Two rod-type creep meters were installed by Lee et al. (2003) right next to the slide to monitor the ground surface deformation. The result of the creep meter monitoring showed the average shortening of about 16.2 mm/yr. Thus, we could confirm that the tilted slide could be affected by the active ground deformation.

Around the hill eastward from the escarpment, we observed other damage on the man-made structure, which was the open crack on a concrete wall (Fig. 3.1d). This concrete wall traces north-south orientation with a length of about 50 m. From this figure, the opening is oriented north-south. So, we can roughly infer that the compressional forces that work on this wall are approximately oriented west-east. Some other similar cracks can be observed along this wall. However, the crack with significant aperture only generated on the south part of the wall.

3-1-2 Evidence of local landslide

In 2017, we observed the evidence of a local landslide occurred near the top of the hill eastward from the escarpment (Fig 3.1e). The scale of this local landslide is about 50 m length and 20 m wide. These slumping materials are contained of mud with some clasts of sandstone and igneous rock. However, in the 2018 field survey, the evidence mentioned above was hard to observe because of weathering and vegetational cover.

3-1-3 Alluvial deposits at the top of the hill

The hill eastward from the escarpment is highly covered by the vegetation and has a variety of dip slope angle of about 20°-30° increasing as it goes to uphill. During such a condition, to make the drilling machine got on a certain position, an excavation was necessary to create an access road. This excavation not only help us to create an access to the drilling point, but also create an access to the outcrops around the hill.

During the field survey, we did some observations around this hill. This area mainly consists of mélange material with fragments of sandstone and andesitic rock (Fig 3.2a). Near the peak of the hill, we observed an obvious outcrop of the sediment deposits (Fig 3.2b). These deposits are alluvial layers sourced from the Coastal Range, which are the andesitic gravelly layer and fine-grained sand layer (Fig 3.3). The width of this alluvial layer and the fine-grained sand layer is about 1 m and 0.5 m, respectively.

Down further, the alluvial layer sourced from the Central Range was observed. This alluvial layer contains metamorphic gravel with very coarse sand. The width of this alluvial layer is about 0.5 m without reached the lower boundary. However, if we consider the mélange material surrounding this outcrop, we could approximate that the mélange might present at a depth of about 3 m below the alluvial layer.

3-2 Core analysis result

3-2-1 Cylindrical core analysis

We observed three distinct lithological units: Lichi mélange, alluvium layer sourced from the Coastal Range, and alluvial gravel sourced from the Central Range (Fig 3.4, Fig 3.5, Fig 3.6, Appendixes: from A.1 to A.20). The Lichi mélange consists dominantly of mud matrix with fragments of sandstone and andesitic (Fig 3.7). These fragments have variated size, shape, and fracture density.

The alluvium sourced from the Coastal Range is quite obvious to be observed since this layer has a bright brown color. This layer consists of sandstone gravel and andesitic gravels (Fig 3.8a). In general, these gravels have an angular to subangular shape with a diameter range of about 5-10 cm. The fine-grained sand layer with the various thickness (a few centimeters to 5 meters) were observed at the particular depth and interlayered with the alluvium gravel sourced from the Coastal Range (Fig 3.8b).

The alluvial layer sourced from the Central Range contains metamorphic gravel, such as slate and some portions of quartzite, with the interlayers of coarse sand material (Fig 3.9). The shape of the gravel is rounded with a diameter range of about 15-20 cm.

We observed the thickness variation of the mélange among the boreholes. In DP-6 and DP-7, the thickness of the mélange is about 13 m. In these two boreholes, the mélange overlies the alluvial gravel. In DP-7B and DP-8, the thickness of the mélange layer is about 15 m and 30, respectively. Meanwhile, in DP-7A, we observed the mélange layer thickness reach of about 60 m. If we correlate the DP-7B, DP-8, and DP 7A, we approximate the dip angle of lithological contact between the overlying mélange with the alluvial layer of about 80°.

3-2-2 Half-Cylindrical core analysis

We bisected some part of the mélange units in our core to advance our observation. We argued that the inner part of the core would be more conserved than the outer surface and lesser geometric effect. Nevertheless, we did not bisect all of the core parts due to the matter of time. We bisect some parts of the core that was more priority to be observed.

Before we bisected the core, we conducted three preparation steps, such as cutting the core, drying the core, and fixing the core by epoxy. We did the cutting in the first step due to the limitation of the Rock Cutting machine. This machine is only able to cut the core with a maximum length of about 0.2 m. Therefore, we manually divided the one-meter core into 0.2-meters core by utilizing a hacksaw.

The next step was drying the core. Since the epoxy only works appropriately on a dried object, so it was necessary to dry the core before the fixing. This drying process was conducted at Sediment Analysis Lab of National Central University, using the constant temperature oven. The drying process spent about 3 to 5 days with a constant temperature of about 52°C.

Dr. Huang, Senior Researcher of CPC, suggested us to fix the core using epoxy to prevent the core to break. Two kinds of epoxy liquid, resin and hardener, were mixed with ratio 15:2, respectively. Afterward, we lubricated all of the core surfaces with the resin-hardener mixture. The hardening process of the core spent about 1 to 2 days.

The final step was the core bisecting. This bisection process was conducted at Sediment Analysis Lab of National Central University, Taiwan, using the Rock Cutting Machine. We bisected the core with the orientation perpendicular with the strike of the observed shear plane in the one-meter core.

3-3 Radiocarbon dating results

We collected 2 samples of charcoal on DP-7B cores and utilized 4 radiocarbon dating data from Taiwan CGS (2018) and Chang et al. (2018). All of the samples were collected from the alluvial layer sourced from the Coastal Range that we observed in the borehole cores; then, these samples were dated by Beta Analytic Radiocarbon Dating Laboratory.

Practically, the concentration of radiocarbon in the atmosphere is variate in respect to the time due to many factors, such as geomagnetic and solar modulation of the cosmic-ray flux, and the carbon cycle (Reimer et al., 2013). This variety would affect the radiocarbon age. Therefore, calibration would be necessary to precise the radiocarbon dating data. All dating data were calibrated by the Beta Analytic Radiocarbon Dating Laboratory based on the INTCAL13 database. The specific information of the radiocarbon dating data is provided in table 3.1.

The provided radiocarbon dating data represent the age of the death of the related material. Therefore, this dating data, in the particular sediment layer, does not always represent the age of that layer. The age of a layer could be younger or at least as old as the corresponding radiocarbon date. To minimize the misinterpretation of the age matter of a layer, we need to utilize more radiocarbon dating data by gathering the dating data from other related studies.

Chen, W. S. (2008) reported two dating data of the alluvial deposits (Fig. 1.5) in Wanan, southward from Tapo ES. He reported that the age of the alluvial deposits in that area ranging from about 4090 to 5990 yr BP. Comparing the dating data in Wanan and Tapo ES, we inferred that the two-dating data in DP-7B, 8154-8189 and 10006-10062 Cal yr BP, apparently did not represent the appropriate age. Thus, we infer that the corresponding material is the colluvial deposits.

Table 3.1 Radiocarbon dates on the corresponding borehole at Tapo ES.

Sample name	Material	Borehole name	Sampling depth (m)	Elevation (m)	Conventional date (yr BP)	Calibrated date (1σ) (Cal yr BP)
CHIHSF-DP1_1270	Organic sediment	DP-1	12.7	261.5	1540 ± 30	1390 – 1415
CHIHSF-DP4_1585	Organic sediment	DP-4	15.85	252.65	1900 ± 30	1820 – 1880
CHIHSF-DP6_1475	Organic sediment	DP-6	14.75	265.65	2070 ± 30	1995 – 2065
CHIHSF-DP6_1955	Organic sediment	DP-6	19.55	260.85	2400 ± 30	2355 – 2460
CHIHSF-DP7B_2635	Charcoal	DP-7B	26.35	257.25	8910 ± 30	10006 – 10062
CHIHSF-DP7B_2947	Charcoal	DP-7B	29.47	254.13	7340 ± 30	8154 – 8189

3-4 Inclinometer record

We performed the monitoring data as the incremental displacement graph (Fig 3.7). This graph shows a plot of displacement versus depth. The colored line would represent the cumulative displacement at the corresponding date. The inclinometer monitoring period of DP-7 and DP-8 is from 6 June 2016 – 18 October 2018 and 11 November 2018 to 30 August 2019, respectively.

There is a fundamental concept to understand the incremental displacement graph. The cumulative displacement in a specific depth is the relative displacement to a fixpoint. In this case, we apply the lower point of the graph as a fixpoint. Therefore, from this graph we learn that there were active movements in DP-7 and DP-8 relative to the lowest point.

In DP-7, the displacement was oriented to the North-Northwest with the cumulated displacement of the upper point of about 40 mm within two years (Fig. 3.7). We observed the significant increase of the displacement magnitude at depth of from 9 m to 8 m and 13.5 m to 12 m. Meanwhile, at depth of above 8 m, the displacement magnitude tended to be gradually increasing upward. This phenomenon might correspond to the presence of the shear

deformation within the corresponding depth. At the bottom depth, of about 13.5 m to 15 m, no significant displacement was recorded.

In DP-8, the inclinometer data show more irregular displacement compared to DP-7 (Fig. 3.8). At a depth of about 26 m to 26.5 m, the displacement magnitude tended to be in the initial position. While the uppermost depth, at a depth of from 22 m to 21 m, the displacement was significantly increase. However, we could infer that the displacement was mainly oriented to the northwest relative to the lowest point with the upward increasing magnitude.
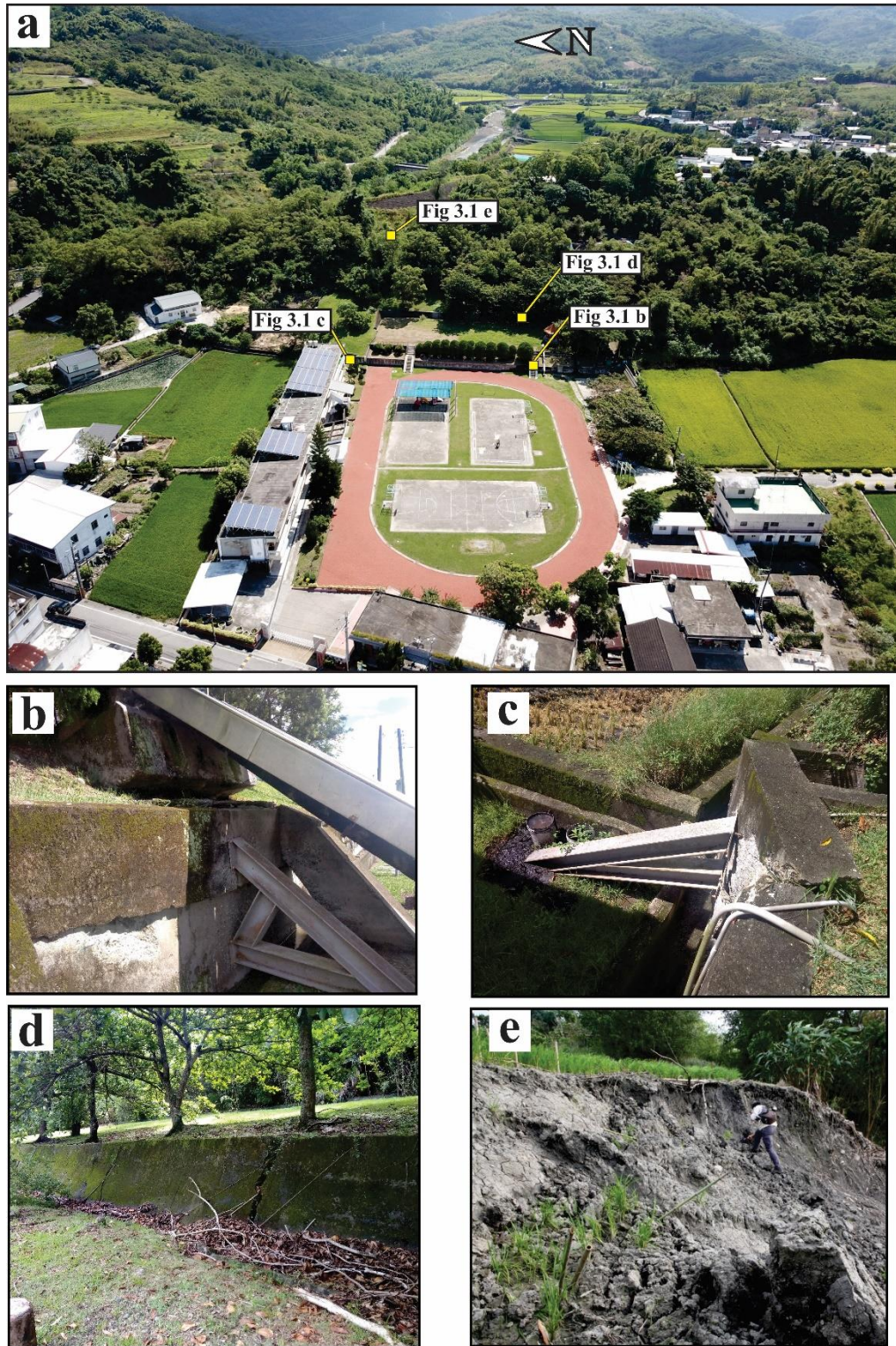
Figure 3.1 Photograph at Tapo Elementary School (Tapo ES) area. (a) Oblique view of Tapo ES area. It was taken on 5 October 2018 by UAV drone. (b) Photograph of tilted platform of the slide. (c) Photograph of teared apart concrete wall that was built on the escarpment. (d) Photograph of deformed concrete wall that located on the hanging wall relative to the escarpment. (e) Photograph of landslide evidence. It was taken on 26 March 2017.
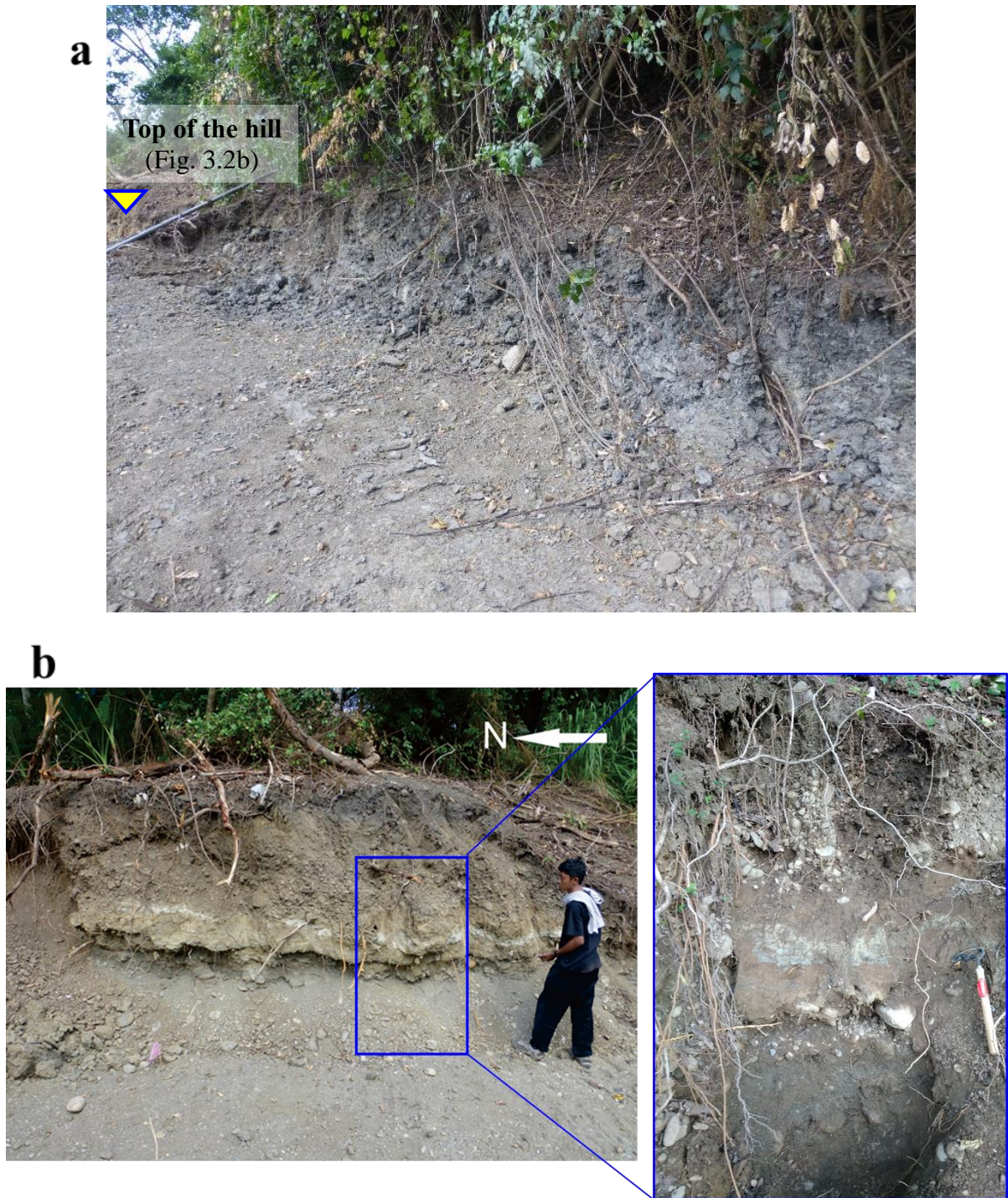
Figure 3.2 Photograph of outcrop at the hill area eastward from Tapo ES. (a) The mélange without internal strata present on the outcrop as shown in this figure. (b) Photograph of outcrop on the top of hill (left) along with the close-up view of the outcrop (right).
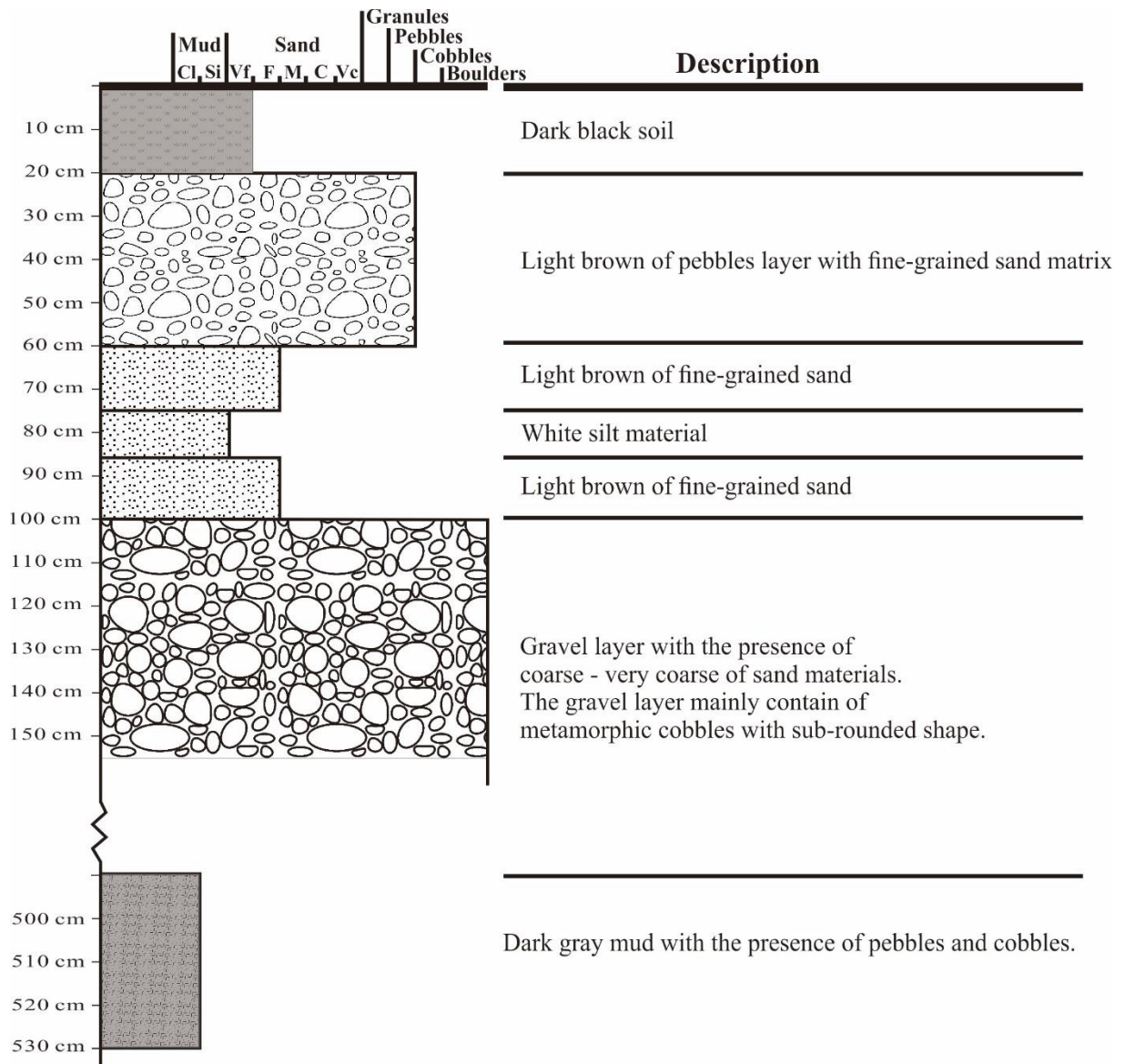
	Mud	Sand		Granules Pebbles Cobbles Boulders	Description

Dark black soil

Light brown of pebbles layer with fine-grained sand matrix

Light brown of fine-grained sand

White silt material

Light brown of fine-grained sand

Gravel layer with the presence of
coarse - very coarse of sand materials.
The gravel layer mainly contain of
metamorphic cobbles with sub-rounded shape.

Dark gray mud with the presence of pebbles and cobbles.

Figure 3.3 The geological columns of the outcrop on the top of the hill area (Fig. 3.2) eastward from Tapo ES.
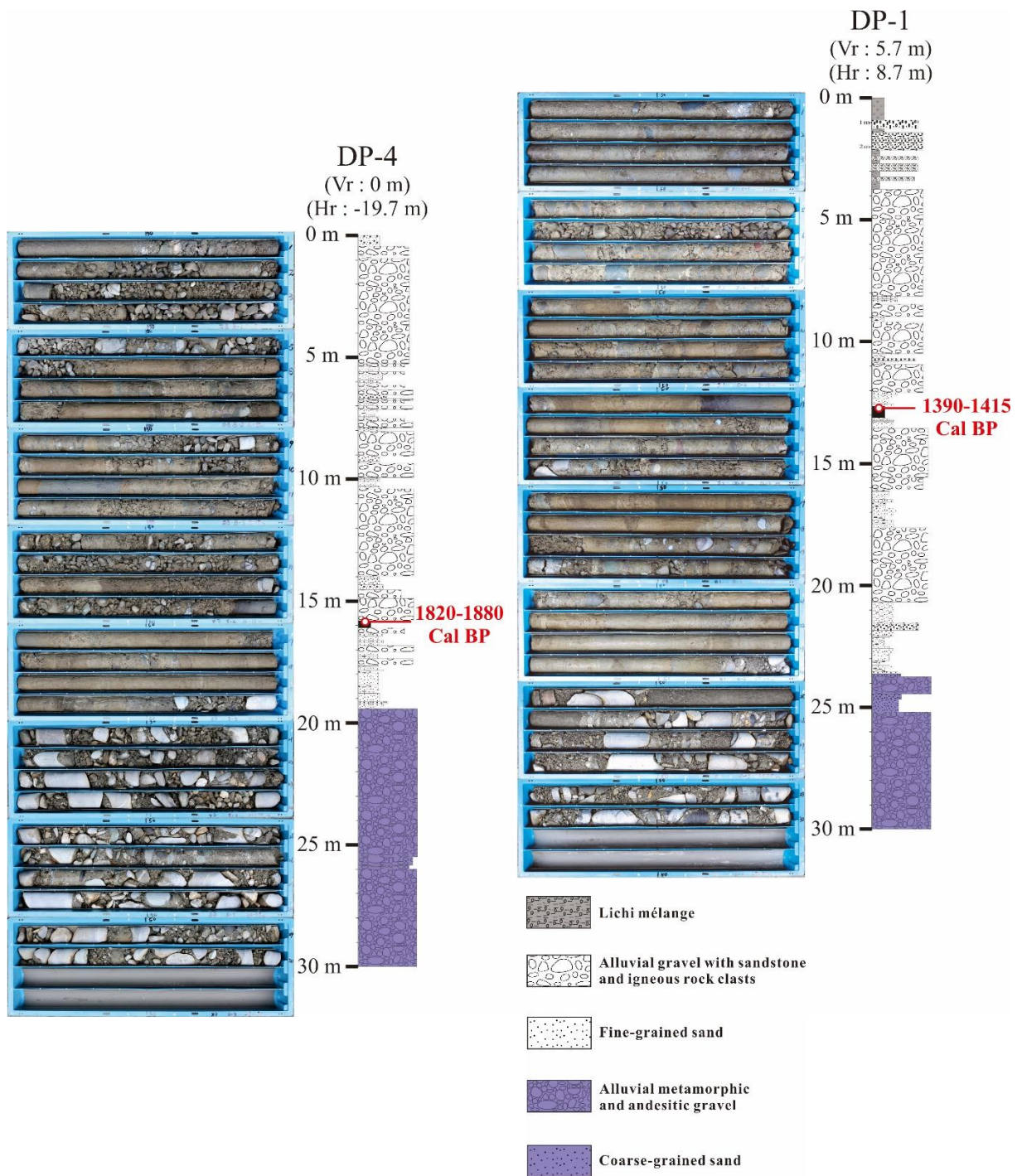
32

Figure 3.4 Photograph of the core and architecture of the core logs DP-1 and DP-4. Vr indicates the relative elevation of the upper end of the borehole with respect to the surface level of the Tapo ES yard. Hr (+) indicates the relative horizontal distance of the borehole from the toe of the major geomorphic scarp to the east. Hr (-) indicates the relative horizontal distance of the borehole from the toe of the major geomorphic scarp to the west. Red label indicates the dating results.
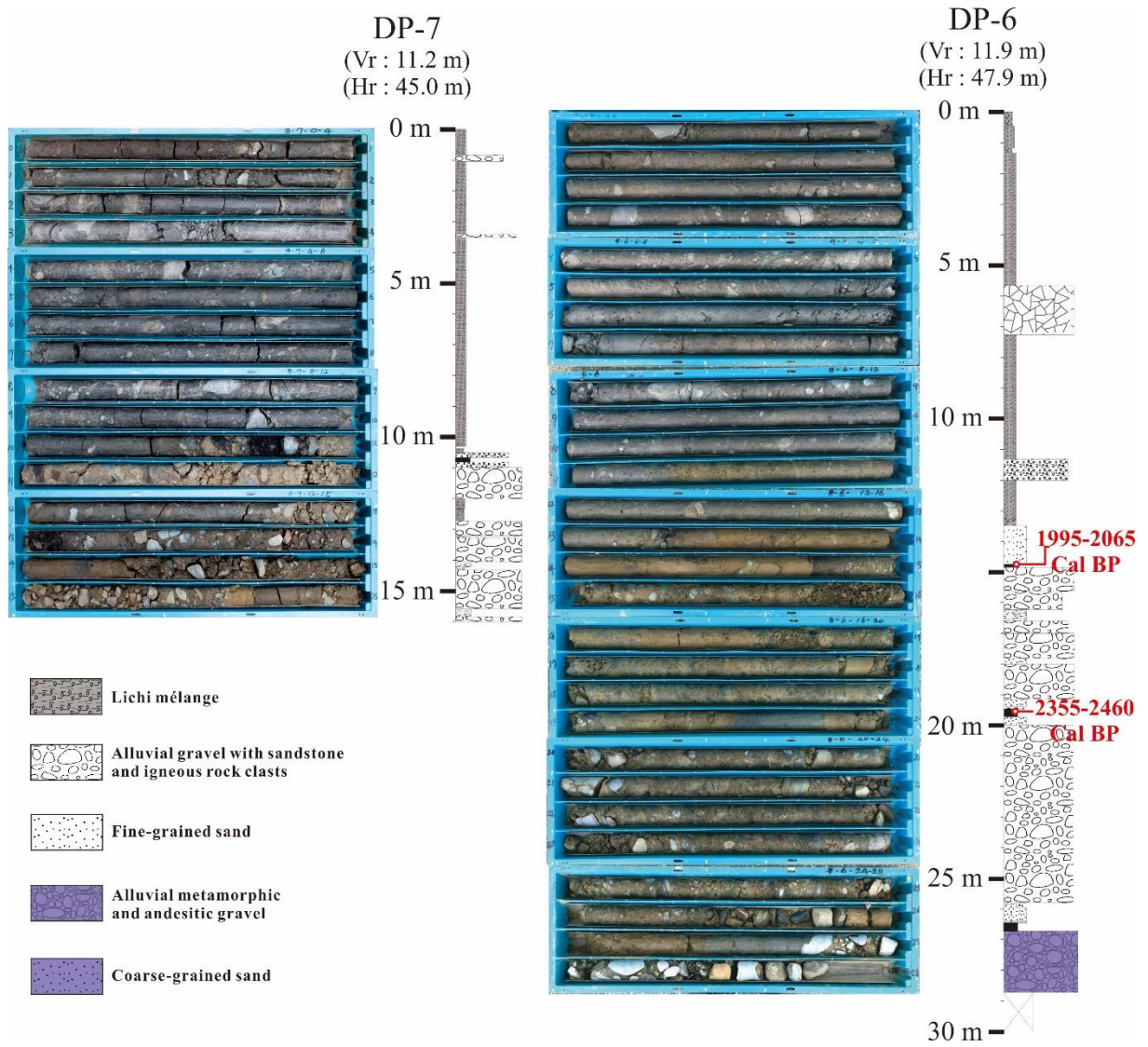
DP-7
(Vr : 11.2 m)
(Hr : 45.0 m)

DP-6
(Vr : 11.9 m)
(Hr : 47.9 m)

0 m

5 m

10 m

15 m

0 m

5 m

10 m

1995-2065
Cal BP

2355-2460
Cal BP

20 m

25 m

30 m

Lichi mélange

Alluvial gravel with sandstone and igneous rock clasts

Fine-grained sand

Alluvial metamorphic and andesitic gravel

Coarse-grained sand

Figure 3.5 Same as Figure 3.4 for borehole 7 and 6.

34

DP-7B
(Vr : 15.1 m)
(Hr : 54.0 m)

DP-8
(Vr : 15.1 m)
(Hr : 57.4 m)

DP-7A
(Vr : 18.5 m)
(Hr : 64.0 m)

10006-10062 Cal BP

8154-8189 Cal BP

Lichi mélange

Alluvial gravel with sandstone and igneous rock clasts

Fine-grained sand

Alluvial metamorphic and andesitic gravel
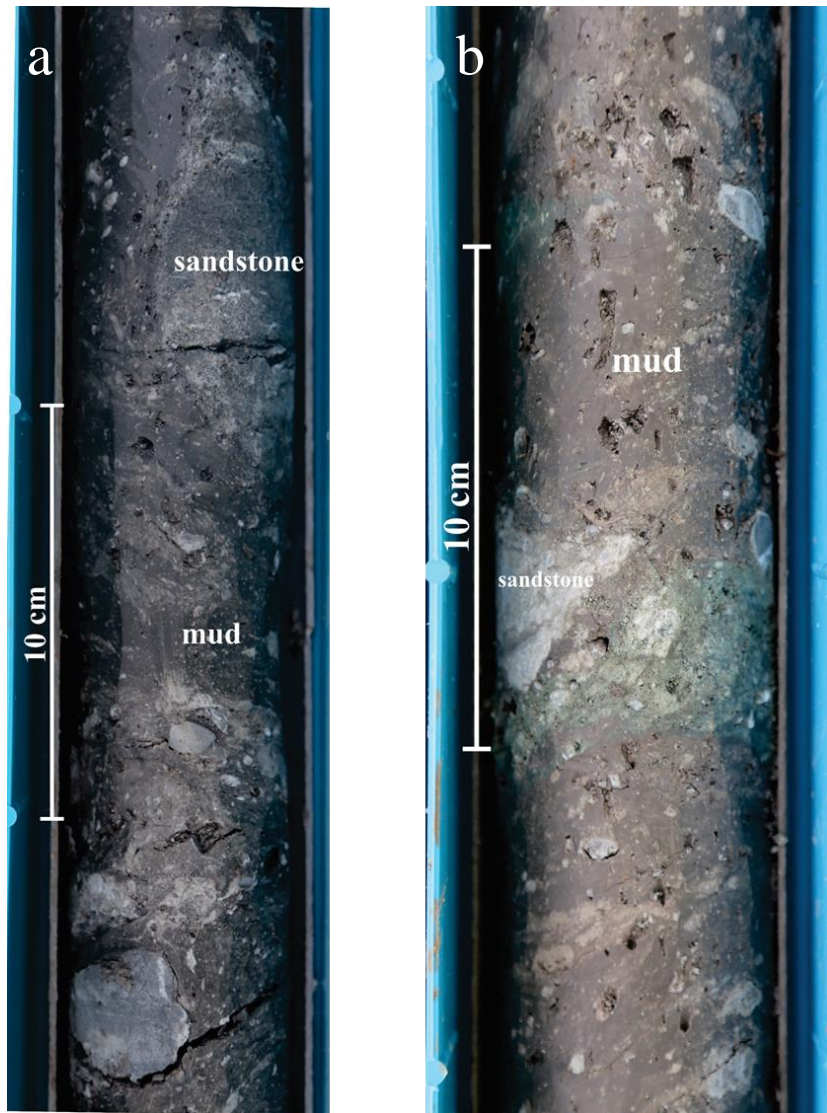
Coarse-grained sand
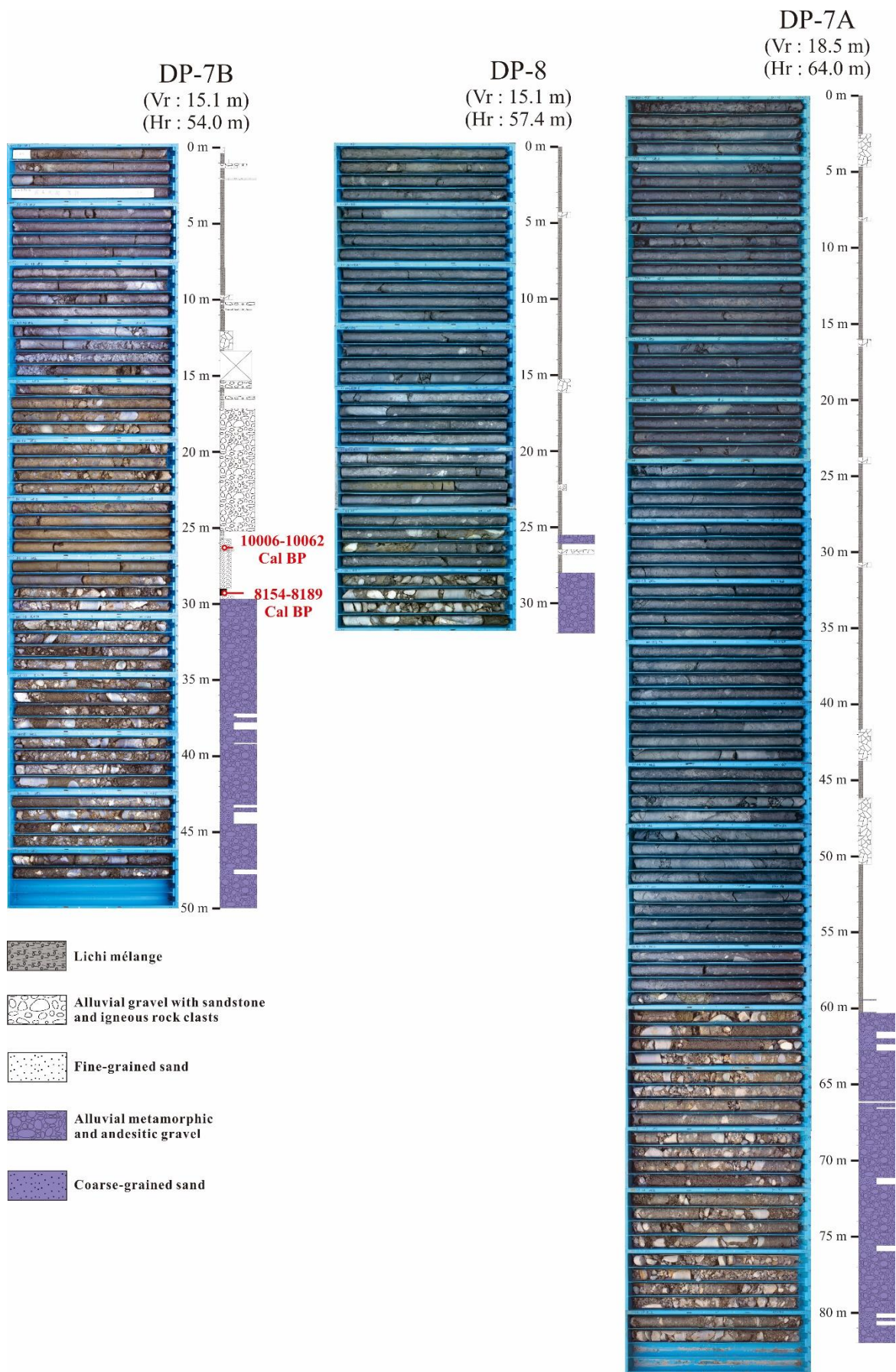
Figure 3.6 Same as Figure 3.4 for borehole 7A, 7B, and 8.

35

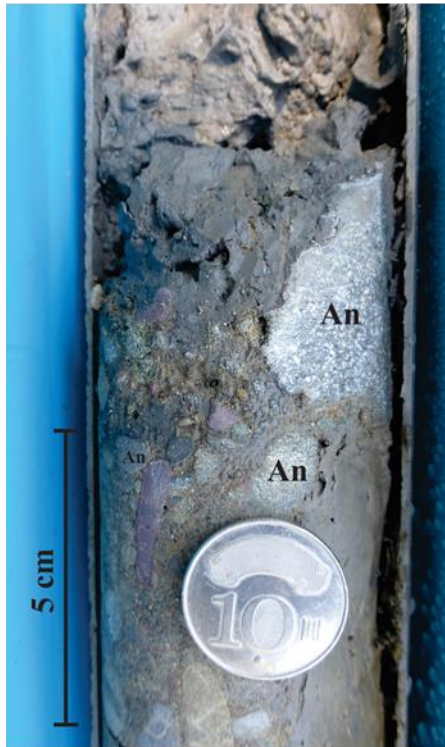Figure 3.7 Close view of mélange material. (a) Rock core of DP-7 at depth 8.5 – 8.7 m. (b) Rock core of DP-6 at depth 5.4 – 5.6 m.

Figure 3.8 Close view of alluvium sourced from the Costal Range (AlCoR). Label "An" indicates the andesitic pebble. (a) Rock core of DP-7B at depth 15.5 – 16.5 m. (b) Rock core of DP-1 at depth 12– 12.3 m.

Figure 3.9 Close view of alluvium sourced from the Central Range (AlCeR). (a) Rock core of DP-8 at depth 29.8 – 30 m. (b) Metasandstone of AlCeR. (c) Rock core of DP-7B at depth 44.3 – 44.4 m.
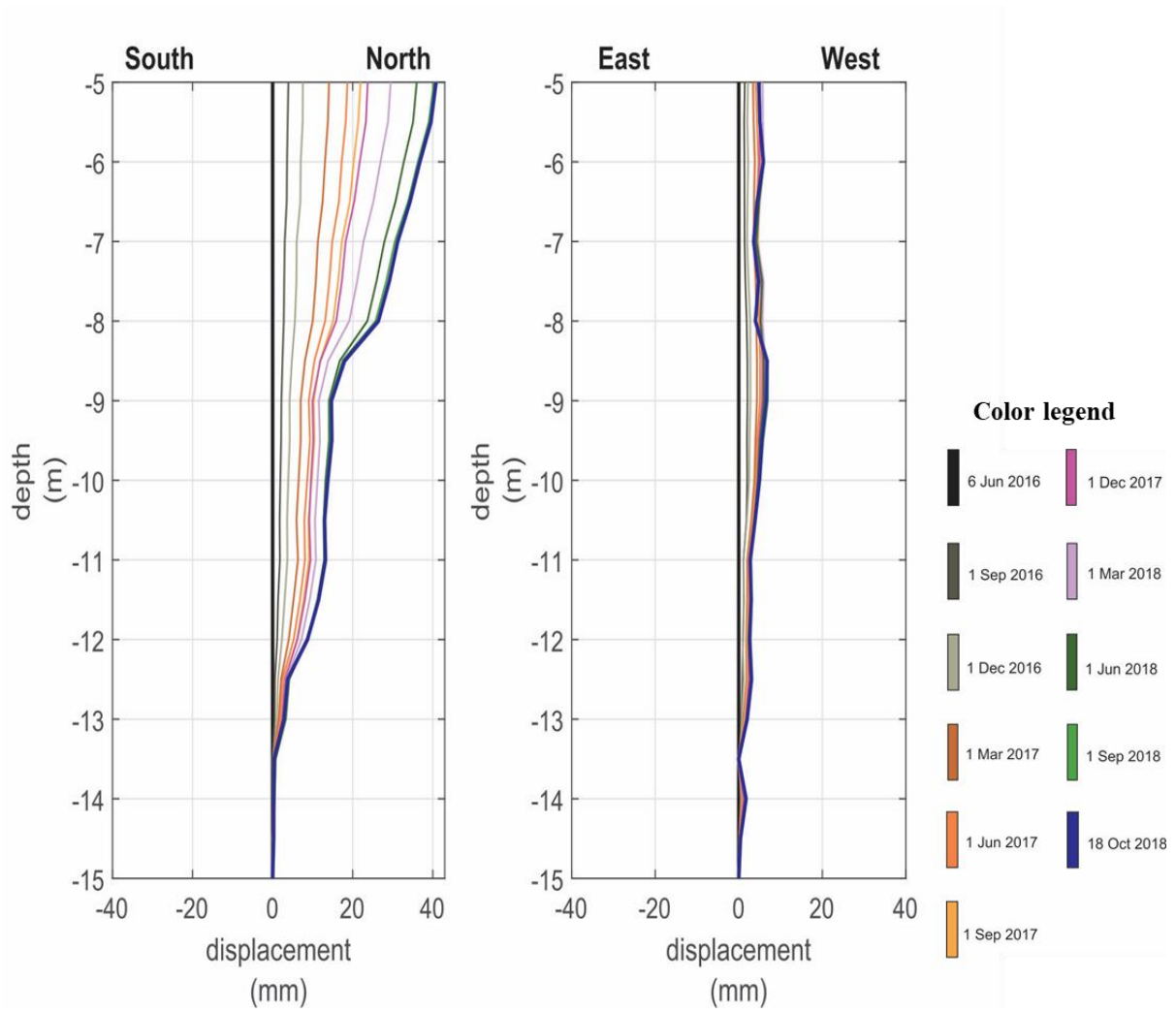
Figure 3.10 Incremental displacement graph of inclinometer data in borehole 7.
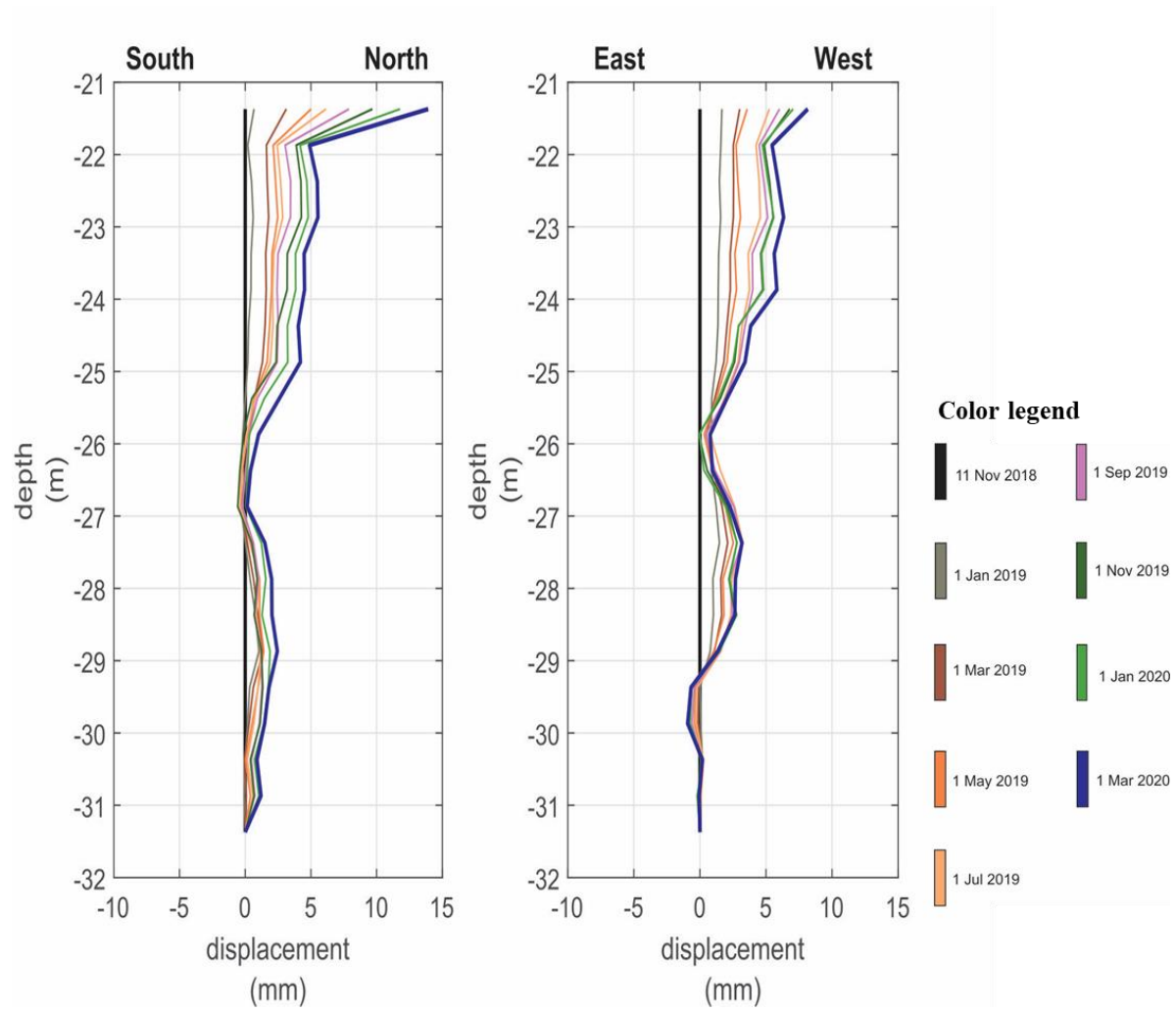
Figure 3.11 Same as Figure 3.10 for borehole 8.

Chapter 4: Discussion

4-1 The trace of Chihshang main fault at Tapo ES area

As we studied from several references in the first chapter, the escarpment was inferred as an upper tip of the Chihshang Fault trace in a particular area. It supposedly means that the eastern region of the escarpment should be the hanging wall, while the western region of the escarpment should be the footwall of Chihshang Fault. Yu & Liu (1989) and Hsu et al. (2018) inferred that the Chihshang Fault is an active fault with an uplift rate of about 20 mm/yr. Thus, we expected that there would be a contrast characteristic between the hanging wall and the footwall materials. However, we cannot find any evidence of this contrast characteristic materials from the study of two borehole cores, DP-1 and DP-4, which are located on the hanging wall and footwall of the escarpment, respectively (Fig. 3.4). Instead, we observe the depth level difference of the lithological contact between the alluvium sourced from the Coastal Range and from the Central Range in between these two boreholes is only 1.5 m. It means that its uplift rate has a low-magnitude. However, this conclusion will contradict the fact that the Chihshang Fault has a significant uplift rate, of about 22 mm/yr.

Moreover, the dating data in each of these two boreholes show that the shallower layer has a younger age compared to the deeper one. This result is a common sense in the principle of superposition. If a fault is supposedly located right beneath the escarpment, then we suspect that it will be the branch of the Chihshang main fault.

In this research, we aim to image the possible subsurface structure by integrating the ERT survey with the rock core observation. The ERT survey provides us the inverted resistivity model that covers a long area; however, it brings several possible interpretations. On the other hand, the rock core provides more detail information about the subsurface structure such as lithology; however, it is only restricted in one particular location. By integrating the core observation with the ERT result, we can approximate the high-quality subsurface structure in our research area.

From the inverted resistivity model (Fig. 2.2), the resistivity values are distributed from 3 to 300 Ohm-m. Such phenomena could be explained by the variety of the physical properties, such as porosity, the salinity of the contained water, or the conductive metallic minerals content of the subsurface material (Telford et al., 1990). For example, the dry to moist clays materials would have a resistivity range of about 7-43 ohm-m (Telford et al., 1990). Thus, the low-resistivity in our research area probably due to the presence of the clay material. Meanwhile,

the high-resistivity value (more than 10 Ohm-m) might be affected by the conductive metallic minerals of the igneous rock, or the presence of the gravel layer with relatively high-porosity. By integrating the resistivity model and the core logs (Fig. 4.1), we confirm that the presence of mélange material and gravel layers are correlated with the low-resistivity and high-resistivity area, respectively.

As we studied from some references, the Chihshang Fault is the high-dip angle contact between the Lichi mélange and the Holocene deposits (Yu et al., 1994; Mu et al., 2011; Angelier et al., 2000). Therefore, the contact between two distinct materials would be one of the important clues to trace the fault. From the resistivity model, we observe two-domains of resistivity value from the western to the eastern area. By considering the suitable correlation between the core logs and ERT results, we expect that the resistivity degradation zone between two-resistivity domains is related to the lithological contact. This interpretation motivated us to do further observation by penetrating another three boreholes, DP-7A, DP-7B, and DP-8, around this resistivity degradation zone. Based on core observation of three boreholese mentioned above, we observed the high-dip angle of lithological contact, of about 77º (Fig. 4.2).

Furthermore, we observe a common characteristic of this lithological contact among these three boreholes. There are some intercalation materials of the Holocene sediment within the mélange body near the lithological contact area (Fig 4.3, Fig 4.4, Fig 4.5). This characteristic might indicate that the fault scratched the footwall materials, which are the alluvial layer, then mixed with the hanging-wall mélange material. Albeit this evidence indicates the presence of the fault, we need to confirm whether this lithological contact is the active Chihshang main fault or not.

One of the characteristics of the Chihshang Fault is actively creeping. Therefore, we installed one-unit of 10 m-length inclinometer in DP-8 by passing through the lithological contact mentioned above to confirm the most recent deformation. By integrating the inclinometer monitoring result (Fig. 3.8) and core observation (Fig. 4.4), we confirm that there are some recent active horizontal displacements around the lithological contact.

By considering the strike of the Chihshang fault of about N18ºE (Angelier et al., 2000), we transformed the North-West oriented of the inclinometer data into the parallel-normal to the strike of the fault (Fig. 4.6a). From this transformation, we observe that the displacement has a trend in normal and parallel to the strike of the fault, which mean an oblique sense. This result is consistent with the earlier studies (Lee & Angelier, 1993; Yu & Kuo, 2001).

Based on these analyses, we infer that the lithological contact is the active Chihshang main fault with the upper tip is located about 55 m to the east from the escarpment with dip angle of about 77°.

4-2 The movement characteristics in the fault zone

The inclinometer data in DP-8 shows an untypical movement at a particular depth level (Fig.4.6a). At a depth of about 26 m to 26.5 m, the displacement magnitude tended to be in the initial position. It might be explained by the Poisson effect as a result of the pressure of the tectonic force. Nevertheless, if we integrate this inclinometer data with the core observation (Fig. 4.3), the untypical movement is corresponded with the presence of intercalated gravel. Therefore, the alternative argument for the untypical movement would be the result of the disturbance from this intercalated material.

The other untypical movement could be observed at a depth of 21 m to 22 m. At this depth level, the displacement significantly increased (Fig. 4.6a). From the core observation at the correspond depth, we observe shear plane with the dip angle of about 50°. From this observation we conclude that this shear plane is recently move and we infer that this shear plane as the branch fault as the Chihshang Fault. The reason that the branch fault has more significant horizontal displacement than the main fault is because the branch fault has smaller dip angle than the main fault. In common sense, the low dip angle of a fault will result in a high-magnitude of horizontal movement.

4-3 The gravitational effect at Tapo Elementary School

4-3-1 Evidence of reworked material based on core observation

As we discussed above, the Chihshang main fault is located about 55 m from the escarpment to the east. However, the mechanism of deformation on the escarpment would be necessary to study. There are some possibilities that might affect the deformation of the escarpment at Tapo ES, such as branch fault, propagation of the hanging wall material, and gravitational effect. We try to analyze all the possibilites based on provided data in this study.

The possibility of branch fault was the first thought to be considered. The branch fault of Chihshang Fault had been inferred at Chinyuan site based on three boreholes core observation and kinematic analysis (Mu et al., 2011). This site is located about 2.5 km to the south from Tapo site. By considering this distance which not that far, the similar mechanism

might occur at both locations. However, we only observe 1.5 m vertical throw of the lithological contact continuity between two-boreholes, DP-1 and DP-4. Based on several studies of geodetic measurement, the Chihshang Fault has a high-uplift rate of about 22 mm/yr. By considering one of the dating data from the boreholes, which is 1880 yr BP, then, the vertical throw should reach of about 47 m. Consequently, if the fault is supposedly presence right beneath the escarpment, then we suspect that it will be a branch fault with a relatively low-uplift rate.

The other possibility is the propagation of the hanging-wall material. This phenomenon might occur if the hanging-wall material consists of soft material, such as mud. The hanging-wall materials may propagate as it reaches the free surface. The distance of this propagation depends on several factors such as: rheology of the material, or the dip angle of the corresponding fault. For the low-dip angle fault, the hanging-wall materials may propagate with a quite far distance due to the continuous force from the fault activity. In another case, for the high-dip angle fault, the hanging-wall materials supposedly propagate for relatively short distance. In fact, the dip angle of the Chihshang main fault at Tapo ES area is high, of about 77°; however, the distance from the tip of the main fault to the escarpment is quite far, of about 55 m. We argue that this propagation mechanism might occur, but not be the only reason to explain the deformation along the escarpment.

Chang et al. (2018) proposed another possibility, which is the gravitational effect. The gravitational effect might occur while the angle of the scarp exceeds the angle of repose in unconsolidated materials (McCalpin & Carver, 2009). The gravitational effect, or slumping, could be a potential reason to explain the great distance of the mud propagation from the fault tip.

If the slumping mechanism plays a role in this area, we supposedly able to observe two kinds of structure, rework of Lichi mélange and the in-situ Lichi mélange. Based on field observation at Fuli, around Bieh River area, Chang et al. (2001) defined the in-situ Lichi mélange as strongly sheared mud with striated foliation. From the stratigraphic plot of striated foliation in their paper (Fig. 1.4), we could learn that the in-situ Lichi mélange has regular oriented foliation. Meanwhile, for the reworked mélange, the in-situ material is supposedly remolded and reconstituted. Based on sedimentary patterns study on the exposures, Horne, G.S. (1970) described one of the structures of the slumped material as the slump fold with irregular geometry and disharmonic style features.

Based on core observation, we confirmed the structure of reworked and in-situ Lichi mélange. We took several core samples of DP-8 at different depth levels; 7.8 m to 8.0 m, 8.21 m to 8.4 m, 8.65 m to 9.0 m, 9.0 m to 9.25 m, 11.8 m to 12.0 m, and 15.0 m to 15.2 m (Fig.

4.7). At the deeper depth, we observe the regular orientation of the lenticular shape of silt and clay within the mud body, which indicates the in-situ Lichi mélange (Fig. 4.8). Meanwhile, at the shallower depth, the mud structures tend to be more irregular and chaotic; however, the material contents are still the same with the in-situ Lichi mélange (Fig. 4.9 a, b & c). We infer that this material is the rework of Lichi mélange as a result of the slumping mechanism. These irregular structures were not only observed in DP-8 but also other boreholes; one of them is DP-7 (Fig. 4.10).

Furthermore, we found different characteristic within the irregular structure in DP-7 between depth level of above 8.5 m and below 8.5 m (Fig. 4.10). The upper reworked mélange mainly contains large clasts of sandstone and igneous rock ($\geq$ 2 cm), while the lower mélange contains smaller clasts ($\leq$ 2 cm). These kinds of characteristics were also observed in the other four cores, DP-6, DP-7A, DP-7B, and DP-8. We suspected that this particular characteristic corresponds to each layer of the reworked mélange that was settled in different environment condition and different period.

We classified the Lichi mélange near the surface based on structure characteristics; those are the in-situ Lichi mélange, reworked mélange, and other materials such as breccia, gouge and fractured rock since these materials were observed within the mélange (Fig. 4.11). In total, we compiled 6 characteristics; they are reworked mélange with small fragment dominant, mélange with large fragment dominant, in-situ mélange, gouge, breccia and gravelly reworked mélange (Fig. 4.12).

4-3-2 Active movement of reworked material based on inclinometer data

To infer if the slumping mechanism contribute in the recent surface deformation on the Tapo ES area, we need to confirm that the reworked material is recently moving. Regarding to this case, this is necessary to analyze the inclinometer data in DP-7 since this borehole is penetrated through the reworked mélange.

Based on this inclinometer data, we observe active movement above the depth level of 13.5 m (Fig. 4.13). If we integrate between inclinometer data and core observation (Fig. 3.5), we could infer that the reworked material actively moves toward north-northwest relative to the overlain alluvial layer; yet this orientation is not quite what we expect. The geometry of the basal of the reworked material, or the complex movement of the slumping material will be the possibilities to explain this typical movement characteristic.

Furthermore, as we described in Chapter 3.4, there is a movement characteristic in DP-7 (Fig. 4.13). Generally, there are two blocks that move with different displacement rates

relative to the base point. The first block is from a depth level of 8 m to the shallower depth, and the second block is from a depth level of 9 m to 13.5 m. The first block moves more rapid compared to the second block. Regarding to the depth level, the first block corresponds with the presence of the reworked mélange dominated by large fragment. Meanwhile, the second block corresponds to the presence of the reworked mélange dominated by small fragment. We infer that these two blocks represent two layers which were settled in different periods.

4-4 Subsurface structure at Tapo Elementary School area

We approximated the subsurface structure by proceeding the stratigraphic correlation among the boreholes. This correlation was based on the principle of sedimentary original horizontality and also the dating data consideration (Fig. 4.14).

In general, the underlying alluvium containing metamorphic gravel would be easier to correlate since its distinguishable characteristic. If we trace the upper boundary of this layer, we find a vertical jump from DP-1 to DP-6. One of the possibilities is the presence of the branch fault in between these two layers. Another possibility is some portions of this alluvium upper layer has been eroded. In DP-6 and DP-7B, we observed the weathered material, which is brownish sand and gravel, on the upper boundary of this alluvium layer. This feature indicate that this upper boundary had been explored on the surface previously. However, in DP-1 and DP-4, the weathered material is absence, but we observed the non-weathered material, the grayish gravel, on the upper boundary of this alluvial layer. Correspond to this observation, we infer that some portions of this alluvium metamorphic gravel in DP-1 and DP-4 has been eroded away in the previous time.

Another vertical jump can be observed from DP-7B to DP-8. One of the possible interpretations is the presence of small branch fault in between the two boreholes; however, we hardly observe the evidence of the branch fault from the core. Another possible interpretation is that this layer has been folded due to the activity of the Chihshang main fault.

In 2013, Chang, Q. classified the terraces along the Chihshang Fault (Fig. 4.15). These terraces were composed of the deposit from the Central Range and the Coastal Range. From her classification, the top of the hill on the east side of the Tapo ES is the terrace labeled as T4. This T4 is correspond with the presence of the alluvial layer that we observed on the top of the hill (Fig. 3.2).

Chang, Q. (2013) also proposed the schematic of terrace formation mechanism (Fig. 4.15). From this study, we learned that the terrace was formed due to river deposition and fault

activity. The terrace that we observed on the top of the hill might represent the deposit that used to settle at the same elevation of the corresponding valley surface, then, it was uplifted due to the Chihshang Fault activity.

In DP-7B above the alluvial layer, at a depth of about 25-30 m, we clearly observed thick (about 4 m-thick) clayey fine-grained sand layer. On the bottom part of this layer, a half meter-thick of clay dominant is presence. This material characteristics are also observed in DP-6 at a depth of about 26-27 m. However, in DP-6, the thickness of this layer is thinner (about 0.5 m-thick) compare to that observed in DP-7B. The structure of this layer is chaotic instead of layering between the clay and fine-grained sand. We inferred that this feature represents the colluvial wedge, which is the result washed out on the nearby hill then settled near the toe of the fault scarp. Another layer with this common feature can also be observed in the shallower depth, in between DP-6 at depth of 13.5 to 15 m and DP-7 at depth of 14 to 14.3 m.

In DP-6, at a depth of 20 to 25.5 m, we observed a thick andesitic and sandstone gravel (about 5.5 m-thick) lying above the colluvial wedge mentioned above. This layer horizontally continues to borehole DP-7B at a depth of 17 to 25 m. Near the lower boundary, the gravel has some grading of the grain size, which indicates that the river used to contributed in the settlement of this gravel. In DP-8, this gravel layer is totally replaced by the presence of the massive Lichi mélange at the corresponding depth. Considering the thickness that remain constant, supposedly some part of this layer was overlying the Lichi mélange and have been uplifted due to the Chihshang Fault activity.

Above the gravel layer mentioned before, the overlying material is the sequence between andesitic gravel and fine-grained sand. Based on the dating data, this sequence approximately started to settle in 2355 to 2460 yr BP. This sequence can be observed in DP-6 and some upper portions in DP-7 with horizontal continuity, which indicates no active fault in between these two boreholes. In DP-7B, this sequence is absent and the Lichi mélange with some intercalated sediment is presence. Above this sequence, we observed two different colluvium settlement, which are colluvial gravel and colluvial sand. Based on the dating data, these colluvial were settled at most 1995 to 2065 yr BP.

From the result of dating data, we can see that the deposit in the eastern area, represented in DP-6, is older than the western area, represented in DP-1 and DP-4, at the relatively same elevation. This phenomenon indicates the presence of the discontinuity in between DP-6 and DP-1. The possible argument for the discontinuity is due to the erosional event which occurred in about 2000 years ago and have relation with the erosion of some portions of alluvium metamorphic gavel mentioned before.

In DP-6 and DP-7, we observed the sequence between reworked mélange and the colluvial sand at depth of about 10 to 14 m. Based on the displacement characteristic that was monitored by the inclinometer, we inferred that the Chihshang Fault is branching into the reworked mélange. This typical sequence is absent in DP-1, which indicates that the settlement only restricted near the Chihshang main fault. In DP-1 and DP-4, we observed the alluvium containing with andesitic pebbles lies at about the same elevation with the aforementioned sequence.

Within this reworked mélange, we observed the continuity of the in-situ Lichi mélange at a particular depth (indicated by red dashed-line in Fig. 4.14). From the correlation, we found that the lower trace of this Lichi mélange correspond to the trace of the Chihshang main fault. A common feature, which is the arrangement of in-situ Lichi mélange, breccia, intercalated sediment in mélange, can be observed along this trace. We traced this kind of arrangement along the Chihshang main fault in DP-7A at depth of about 59 to 60 m, in DP-7B at depth of 11 to 17 m and DP-8 at depth of 25 to 29 m. We still can observe the arrangement between breccia and the in-situ Lichi mélange in DP-6 at depth of 4 to 8 m and the presence of in-situ Lichi melange in DP-7 at depth 4 to 5 m. If we trace these features among the boreholes, we found the continuity. Thus, we infer that the trace of the Chihshang main fault continues to the shallows deep and truncates some settlements of the reworked mélange.

Meanwhile in DP-7 and DP-6 at depth of 0 to 4 m, the in-situ Lichi mélange is overlain by the reworked mélange. If we trace the upper boundary of the in-situ Lichi mélange in between DP-7 and DP-6, apparently the reworked mélange truncates the in-situ Lichi mélange and overprint the upper tip of the Chihshang main fault. Next to the escarpment in DP-1, we observed the mixture between mud with the clasts of rock which we inferred still correlate with the reworked mélange that we observed in DP-7 and DP-6. Therefore, we conclude that two mechanisms, faulting and slumping, correspond to the recent surface deformation at Tapo ES area. Based on all correlation mentioned above, we approximated the section model of the Chihshang main fault at this research area (Fig. 4.16).

4-5 Reconstruction of the evolution of the Chihshang Fault movement

We approximated the evolution of the Chihshang main fault movement started from the present condition to backward (Fig. 4.17). Thus, in stage 1, we have the subsurface structure model that still correspond to what we conclude previously. In this stage, the major escarpment is corresponded with the front side of the slumping material. In stage 2, we undo the slumping

events (ReMe4), so we have the major escarpment that correspond with the upper tip of the Chihshang main fault. In stage 3, the alluvium sourced from the Coastal Range (AlCoR4) was not settled yet, thus the ground surface was the fine-grained sand sourced from the Coastal Range with the rework mélange distributed near the toe of the Chihshang Fault scarp. At that period, the major scarp corresponded with the upper tip of the Chihshang main fault.

In stage 4, we undo the Chihshang main fault that was thrusting over the rework mélange (ReMe3). In this stage, the upper tip of Chihshang main fault was concealed by the reworked mélange and the scarp might be referred to the front side of the reworked mélange settlement. The sequence between the thrusting of the Chihshang main fault over the reworked mélange and the slumping were occurred up to the stage 7. In this stage, the scarp might be referred to the upper tip of the Chihshang main fault.

In stage 8, we undo the settlement of the colluvium (Co4) that deposited near the toe of the major scarp of Chihshang main fault. Then, up to stage 10, the sequence between the thrusting of the Chihshang main fault over the reworked mélange and the slumping were occurred. In stage 11, we undo the alluvium deposit sourced from the Coastal Range, and in stage 12, we undo the colluvial deposit which was settled near the toe of the scarp of Chihshang main fault.

The following stage, stage 13, we undo the alluvium sequence between the gravel and fine-grained sand sourced from the Coastal Range with the range time from 1390 to 1880 yr BP. The undoing of this sequence corresponded with the recovery of the Chihshang main fault movement that had uplifted the Lichi mélange for about 11 m, by assuming the uplift rate of about 22 mm/yr. We also infer the recovery of the layer that used to cover the Lichi mélange on that period. This concept is based on the principle of terrace formation proposed by Chang, Q. (2013), which inferred that the alluvium deposit was used to settle and cover the hanging wall of the Chihshang Fault.

In stage 14, we recovery the layers that had been eroded away which we suspect due to the incision of the creeks or tributaries from the Coastal Range. In stage 15, we undo the alluvium sequence between gravels and fine-grained sand. From the dating data, this alluvium sequence was settled during 1995 yr BP to 2460 yr BP. In this stage, the upper tip of the Chihshang main fault was concealed by the alluvial gravel deposit (AlCoR1) sourced from the Coastal Range.

In stage 16, we undo the settlement of the alluvial gravel (AlCoR1). At that period, the major scarp was referred to the upper tip of the Chihshang main fault with some colluvial deposit (Co1) on the toe of the scarp. In stage 17, we undo the colluvial settlement (Co1) thus

we had the major geomorphic scarp corresponded with the upper tip of the Chihshang main fault, yet the Lichi mélange was mainly covered by the alluvium deposit sourced from the Central Range. The initial position of the alluvium deposit that overlay the Lichi mélange will be discussed in the following subchapter to approximate the uplift rate of the Chihshang Fault.

4-6 Uplift rate of the Chihshang Fault at Tapo

We approximate the uplift rate based on two observations; inclinometer data and the elevation of the alluvial deposit on the top of the hill. Both observations have different principle to approximate the uplift rate and not the direct method to measure the uplift rate, thus we will correlate the result of these two observations with the previous study.

4-6-1 Uplift rate based on inclinometer data

As we explained in the previous chapter, we utilized the inclinometer to monitor the horizontal displacement beneath the surface. In the most recent period, the inclinometer was installed through the Chihshang main fault in DP-8 to monitor the activity of the fault. As we recognized, some active displacement is recorded. Although in this research, the inclinometer monitors the horizontal displacement, yet we can infer the uplift rate (U) by the following equations.

$$U = d \times \tan(\alpha) \tag{4.1}$$

with d is the horizontal displacement in meter and α is the apparent dip along the horizontal displacement vector. The apparent-dip can be calculated by the following equations.

$$\alpha = \tan^{-1}(\tan \delta \times \cos \theta) \tag{4.2}$$

with δ is the true-dip angle and θ is the angle between true- and apparent-dip direction.

We utilized the inclinometer data in DP-8 at depth of about 22 to 24 m (Fig 4.18). We considered this ranging of depth due to the consistency of the displacement magnitude. We expect that by restricting the analysis only for the consistent displacement, we can minimize the effect of displacement that not represent the movement of the Chihshang main fault, such as Riedel shear, or disturbance from the intercalated material. The accumulate horizontal displacement data for 17 months monitoring (11 Novermber 2018 to 1 March 2020) at a depth of 22 to 24 m are provided in table 4.1.

We obtain the mean value of the horizontal displacement of about 7.6 mm/yr with direction to 49.4º NW. Thus, the apparent dip will be 76.4º. By using this mean value and the

apparent-dip of fault, we obtain the approximate uplift rate of about 22.5 mm/yr with the slip rate of about 23.2 mm/yr.

4-6-2 Uplift rate based on the elevation of the alluvial deposit on the top of the hill

As we described in the previous chapter, we observed the alluvial metamorphic gravel deposit lies above the Lichi mélange on the top of the hill, eastward from the escarpment. By finding the relation between the alluvium on the top of the hill and in the borehole, we can approximate the uplift rate from two parameters, the vertical throw and the age of the alluvium.

One of the characteristics of the alluvial metamorphic gravel on the top of the hill is the brownish color as a result of weathering. This evidence can support us to relate between the alluvium on the top of the hill and the alluvium in the borehole. We observed the evidence of weathered alluvial metamorphic gravel in DP-7B at two different depth, 29.5 m and 45 m. Based on the terrace forming proposed by Chang, Q. (2013), the upper weathered alluvial gravel supposedly correspond to the T2, while the lower weathered alluvial gravel correspond to the T4. In her thesis, the upper hill near the Tapo ES was classified as T4; thus, we will assume that the weathered alluvial metamorphic gravel on the top of the hill correspond with the weathered alluvial metamorphic gravel at depth of 45 m in DP-7B. The elevation of the upper hill is about 24.5 m relative to the valley, so, we can calculate the vertical throw of two weathered alluvial gravel of about 54.4 m

Next step, since we do not have any dating data of the corresponding alluvium layer, we try to approximate the age. From this study, we get the oldest age of the layer that overlies the alluvial metamorphic gravel of about 2355 to 2460 Cal yr BP. Meanwhile in Wanan site, from Chen, W. S. (2008), the youngest age of the alluvial metamorphic gravel, which located a bit lower than the depth of the corresponding weathered alluvial metamorphic gravel in DP-7B, is ranging of 4090 to 4390 Cal yr BP. Thus, we assume the age of the alluvial metamorphic gravel on the top of the hill of about 2500 to 4000 yr BP. Then, with the vertical throw of about 54.4 m and the ranging age of about 2500 to 4000 yr BP, the approximate uplift rate is ranging from 13.6 to 21.8 mm/yr.

Table 4.1 Accumulated horizontal displacement of inclinometer data from November 2018 to March 2020.

Depth (m)	Horizontal displacement (mm)	
	Normal to the fault strike, N72ºW	Parallel to the fault strike, N18ºE
21.87	6.7	3.0
22.37	7.3	3.4
22.87	7.7	3.3
23.37	6.7	2.5
23.87	6.9	2.5
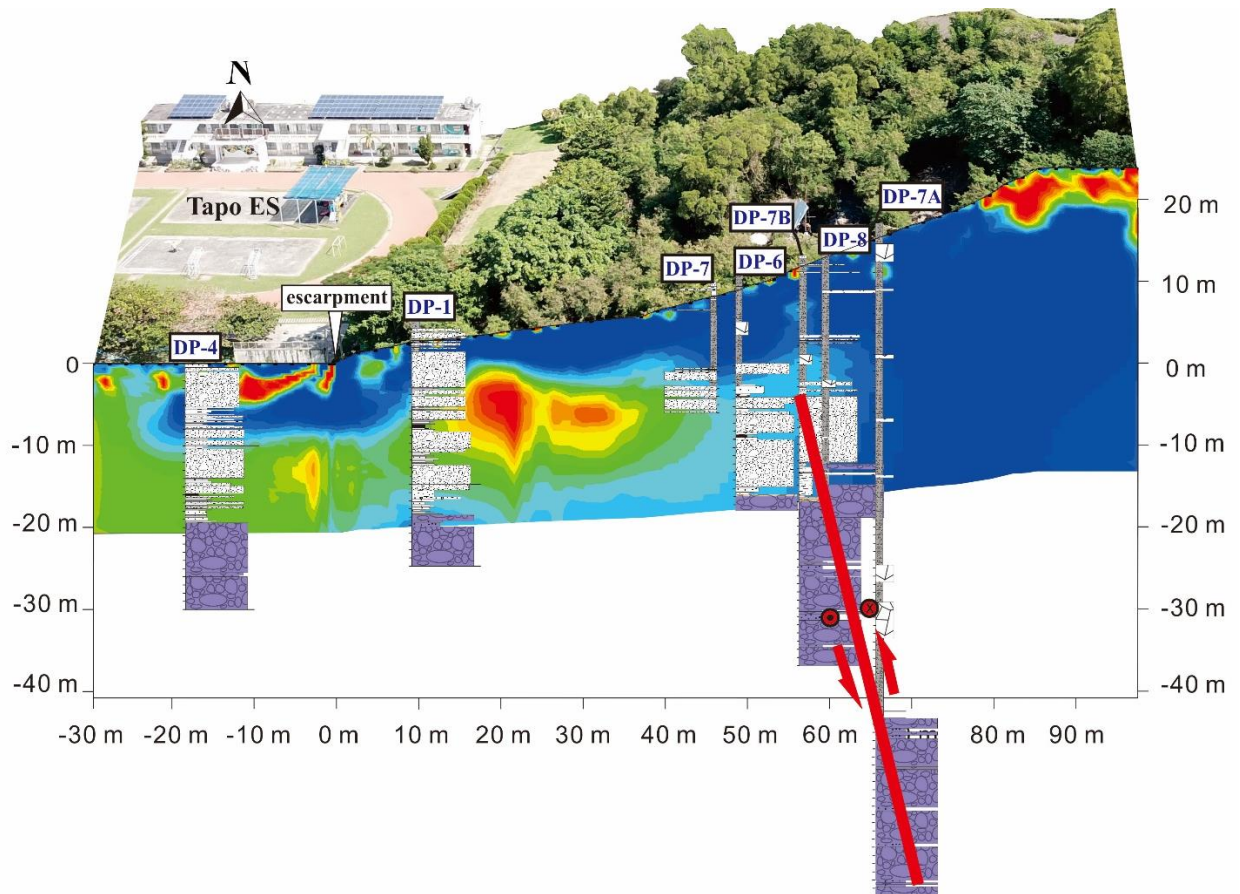
Figure 4.1 Three-dimension (3-D) perspective view shows the integration of core logs and inverted resistivity model. X-axis indicates depth relative to the toe of the escarpment. Y-axis indicates the horizontal distance relative to the toe of the escarpment.

Figure 4.2 Photograph of the lithologic contact between the mud and the Holocene sediment. (a) Photograph of lithological contact between mud (left side) and fine-grained sand (right side) on borehole core 7B at depth of 16 m. (b) Photograph of lithological contact between sand (left side) and mud (right side) on borehole core 8 at depth 28 m.
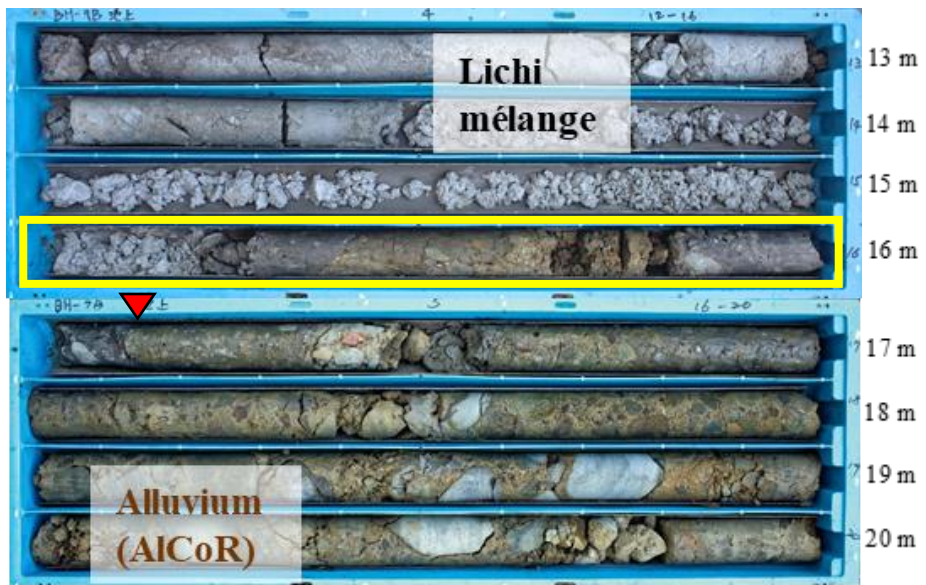
Figure 4.3 Photograph of the rock core of DP-7B at depth of 12 m to 20 m. Red triangle points the lithological contact. Yellow rectangular highlights the mixed zone near the lithological contact between Lichi mélange and Holocene deposit.
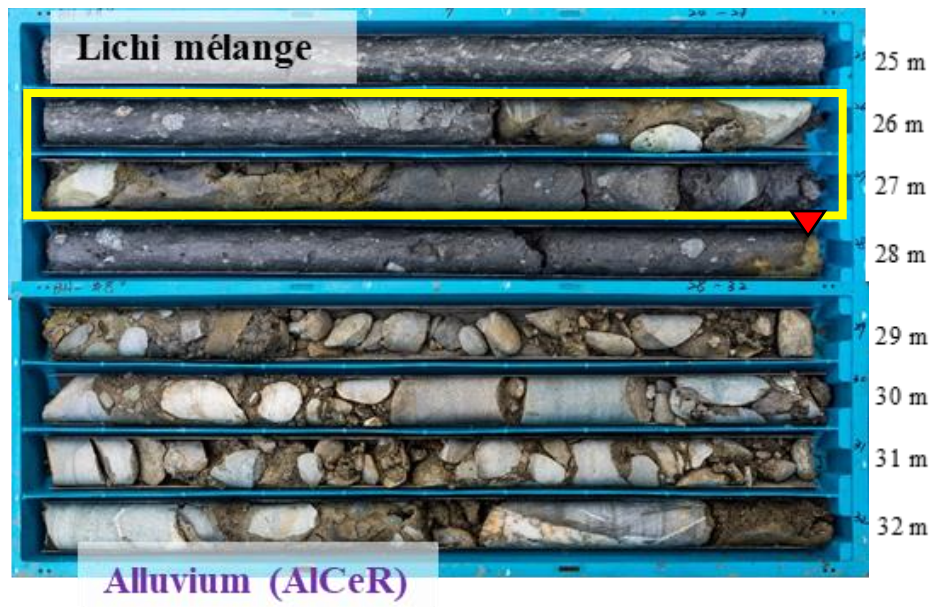
Figure 4.4 Same as Figure 4.3 for DP-8.
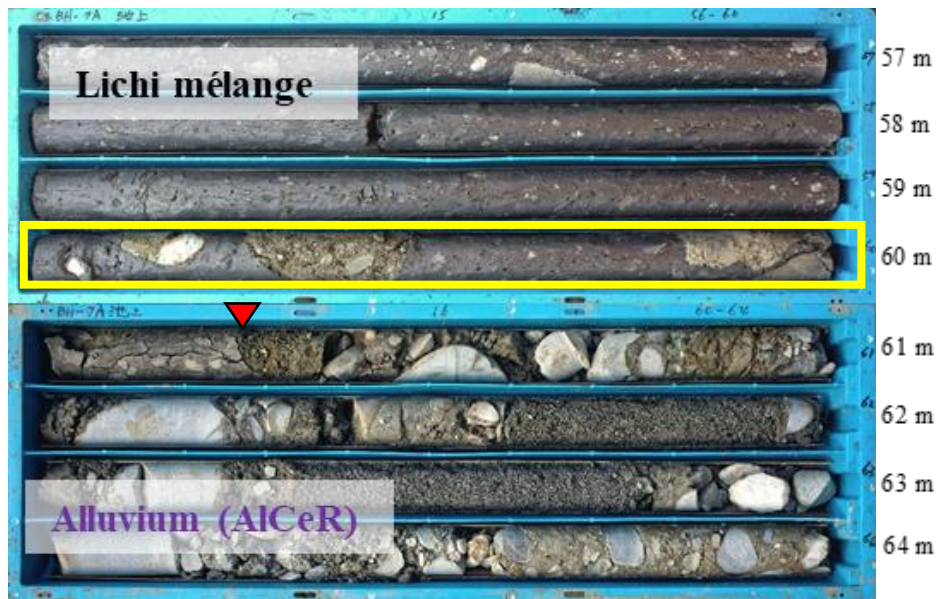
Figure 4.5 Same as Figure 4.3 for DP-7A.
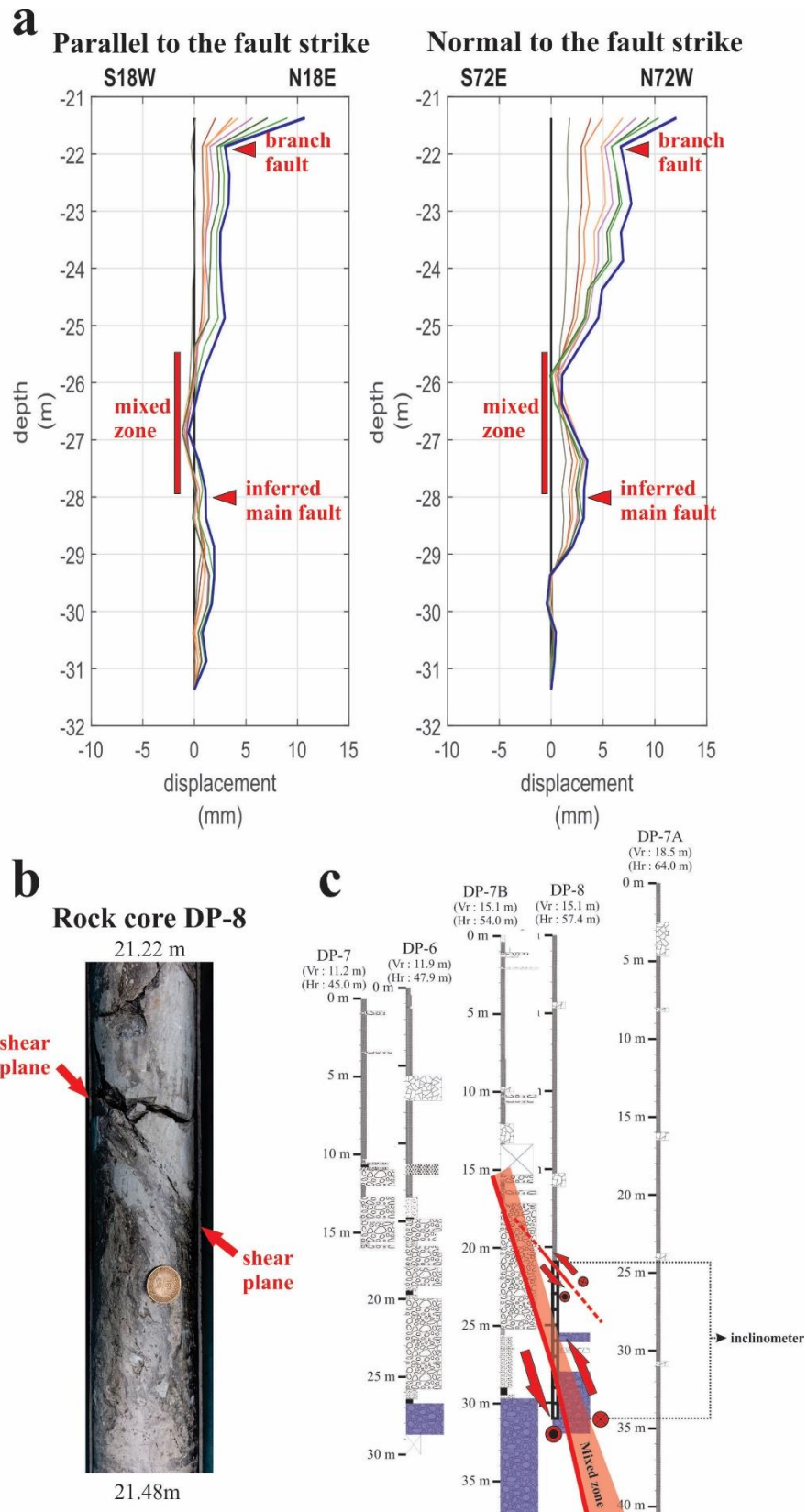
Figure 4.6 (a) Incremental displacement graph of inclinometer data in DP-8 by projecting to fault axis (N18°E to S18°W) along with interpretation label based on core observation. (b) Close view of shear plane in rock core DP-8. (c) Core logs along with the trace of main fault, branch fault, and mixed zone.
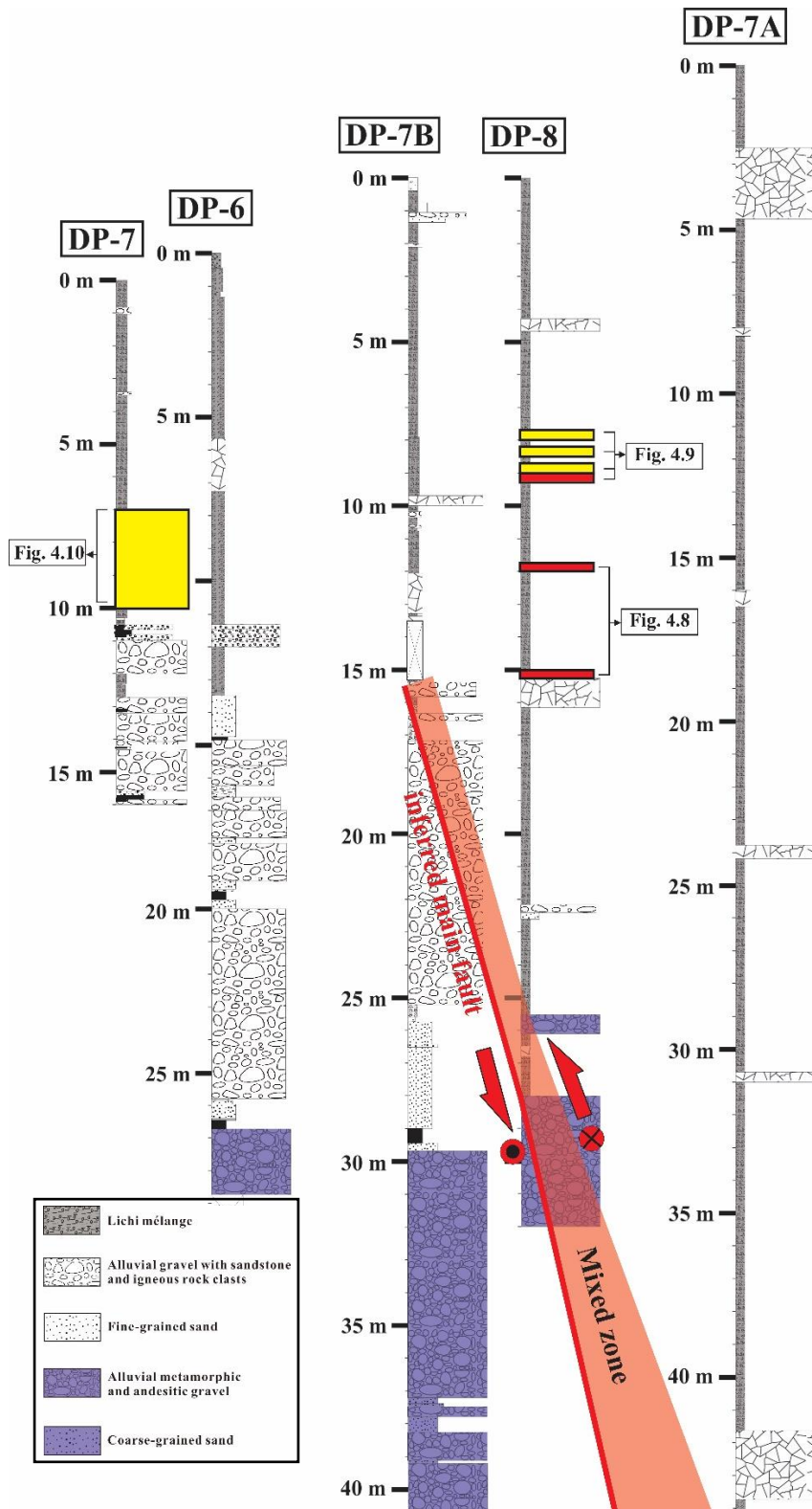
Figure 4.7 Core logs of borehole 7, 6, 7B, 8, and 7A with proportional vertical and horizontal position. Number with unit of length, meter, indicates the depth level from the ground surface. Colored rectangle indicates the part of the core that is analyzed by bisection. Yellow rectangle indicates the observed reworked mélange. Red rectangle indicates the observed in-situ mélange. The observation figures provided in Figure 4.8, Figure 4.9, and Figure 4.10.

57
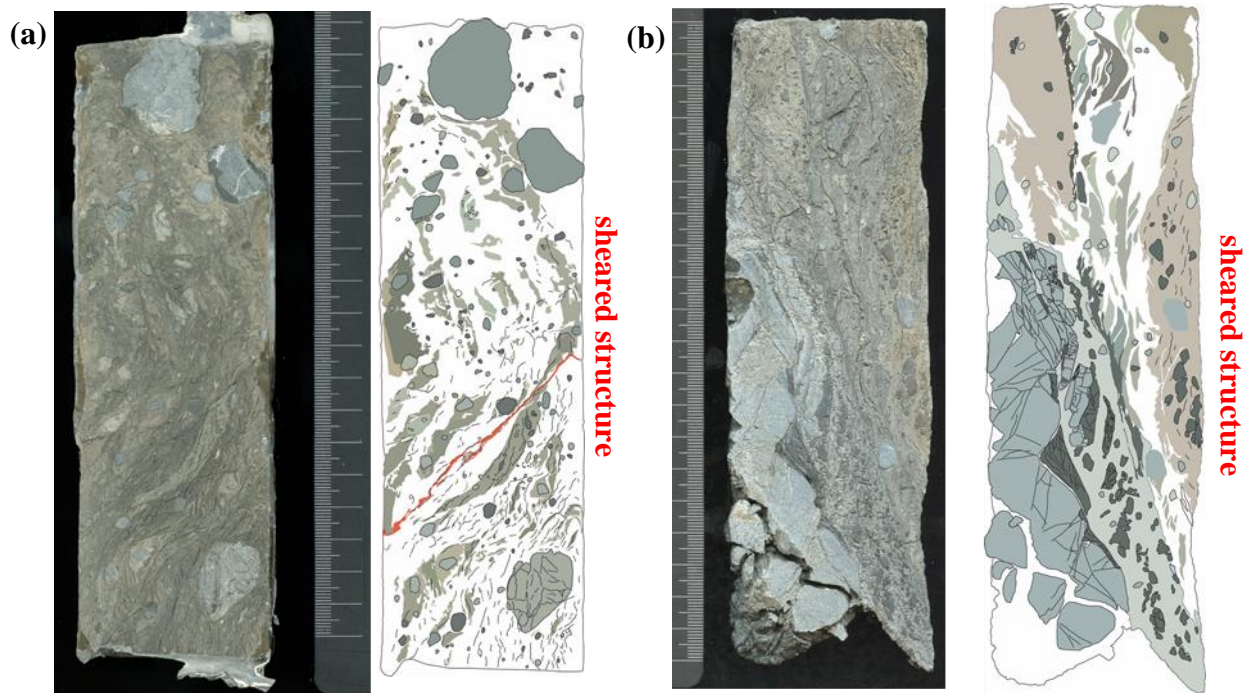
Figure 4.8 Photograph of half-cylindrical core along with the sketch of the mud structure in borehole DP-8. Colorless area (white) indicates the mud material. Colored area indicates fragment that embedded in the mud body. Black-line indicates crack. (a) DP-8 core sample at depth of 11.8 m to 12.0 m. (b) DP-8 core sample at depth of 15.0 m to 15.2 m.
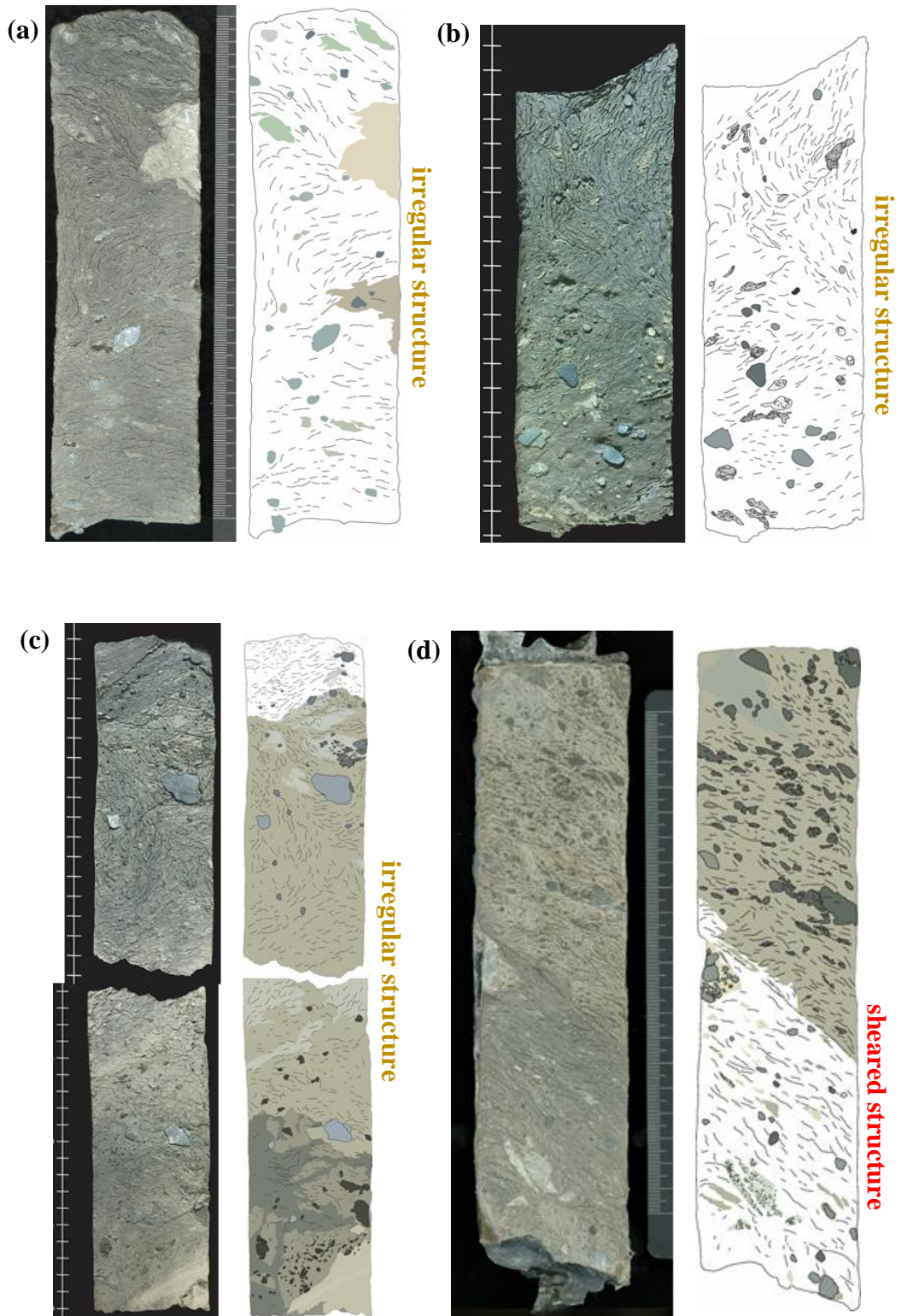
Figure 4.9 Same as Figure 4.8. (a) DP-8 core sample at depth 7.8 m to 8.0 m. (b) DP-8 core sample at depth 8.21 m to 8.4 m. (c) DP-8 core sample at depth 8.65 m to 9.0 m. (d) DP-8 core sample at depth 9.0 m to 9.25 m.
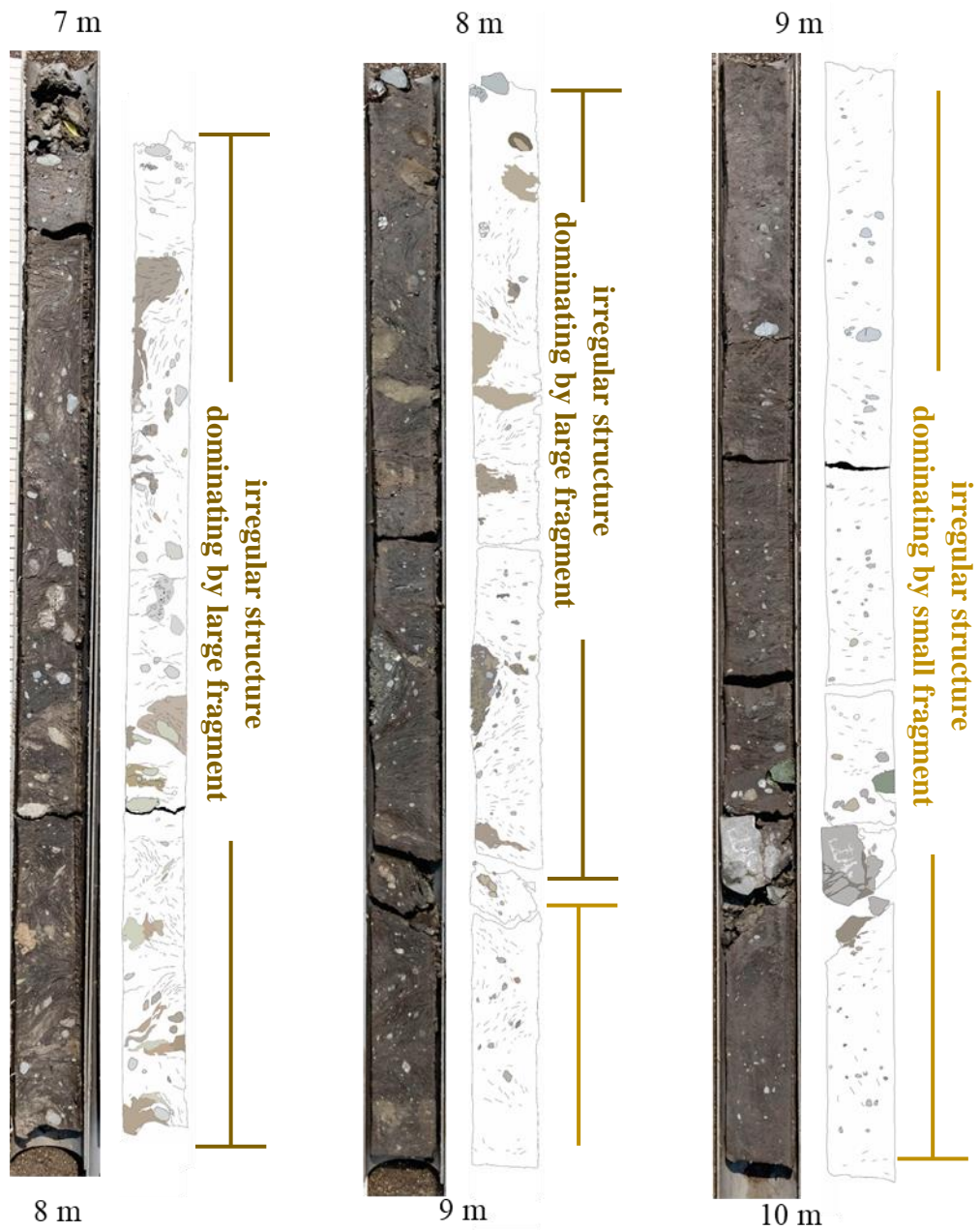
Figure 4.10 Photograph of half-cylindrical core along with the sketch of the reworked mélange body in borehole DP-7. Colorless area (white) indicates the mud material. Colored area indicates fragment that embedded in the mud body.
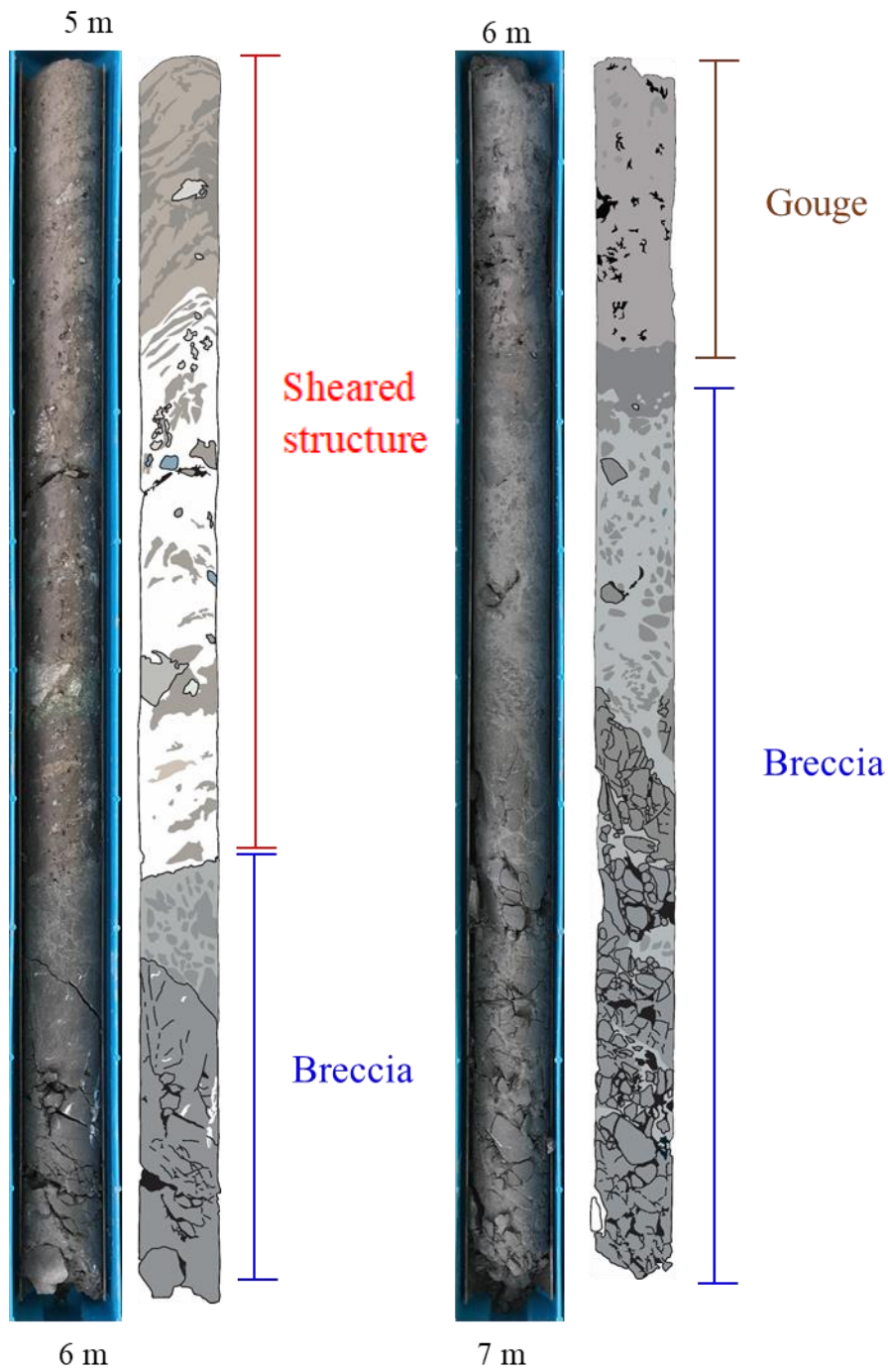
Figure 4.11 Photograph of core along with the sketch of the mélange body in borehole DP-6. Colorless area (white) indicates the mud material. Colored area indicates fragment that embedded in the mud body.
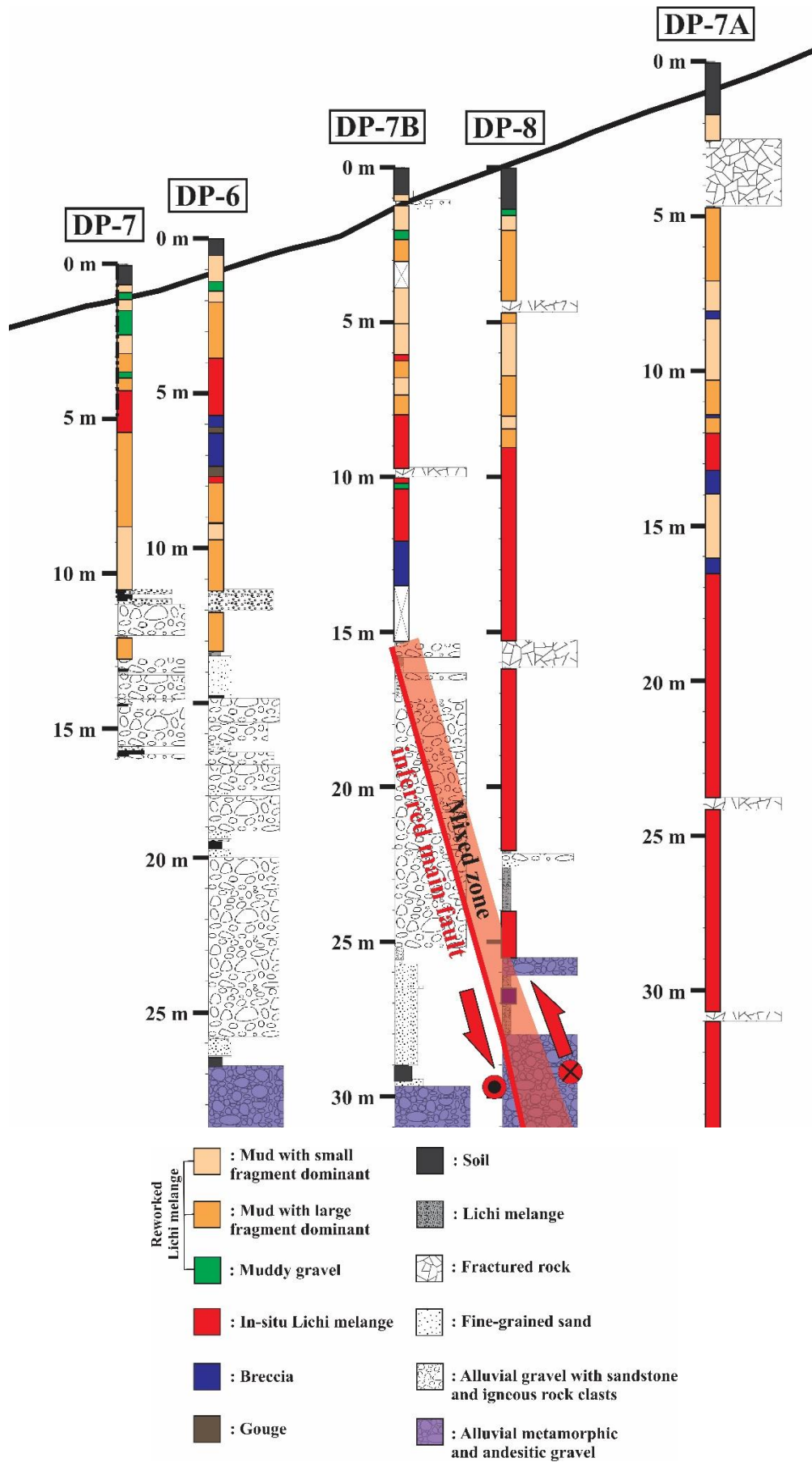
Figure 4.12 Core logs with Lichi mélange classification.
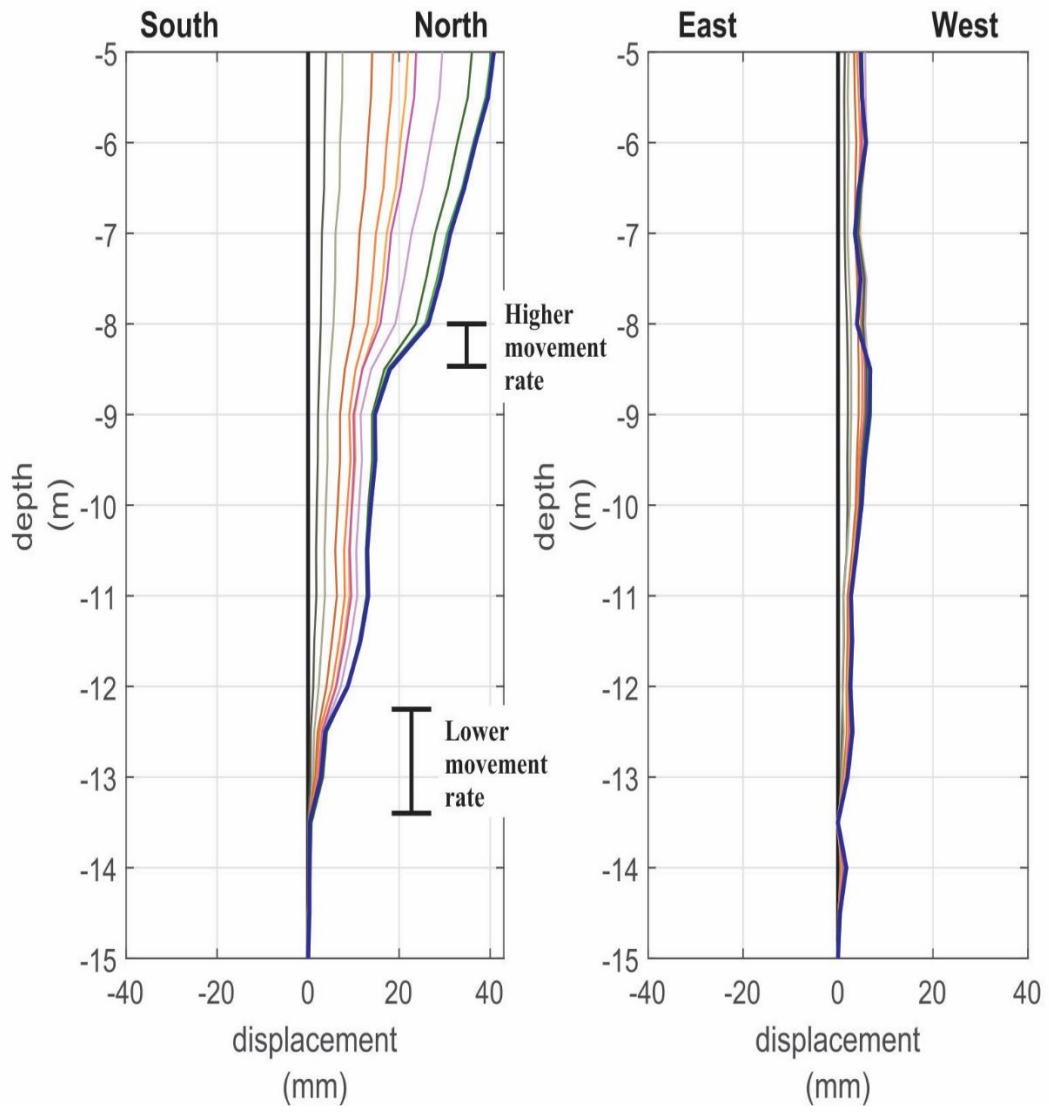
Figure 4.13 Incremental displacement graph of inclinometer data in DP-7 along with general classification of moving rate.
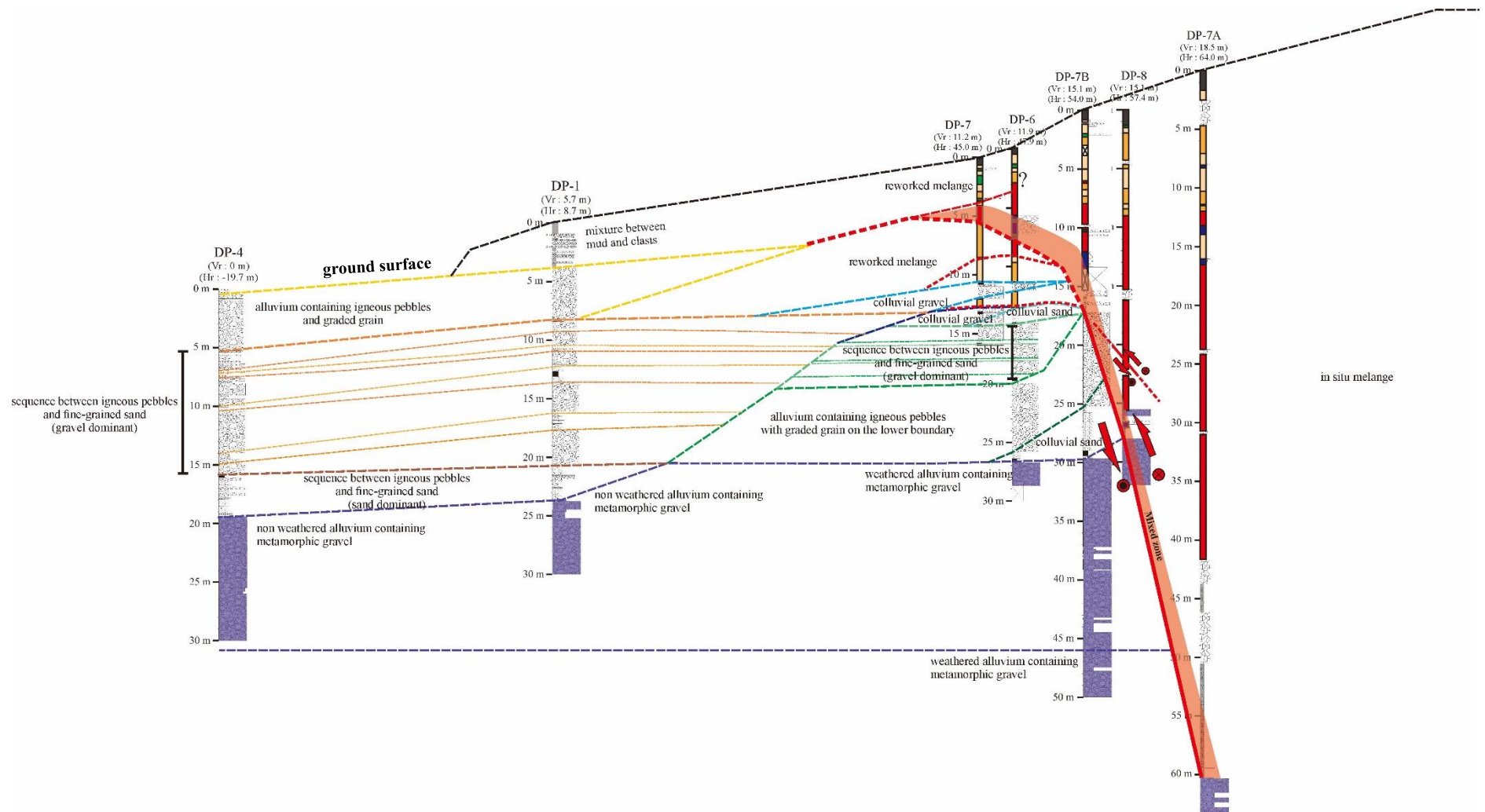
Figure 4.14 Core correlation. Bold-red-dashed line indicates the trace of the main Chihshang Fault. Thick-dashed colorful lines indicate correlation of the certain layer boundary among the boreholes.

64
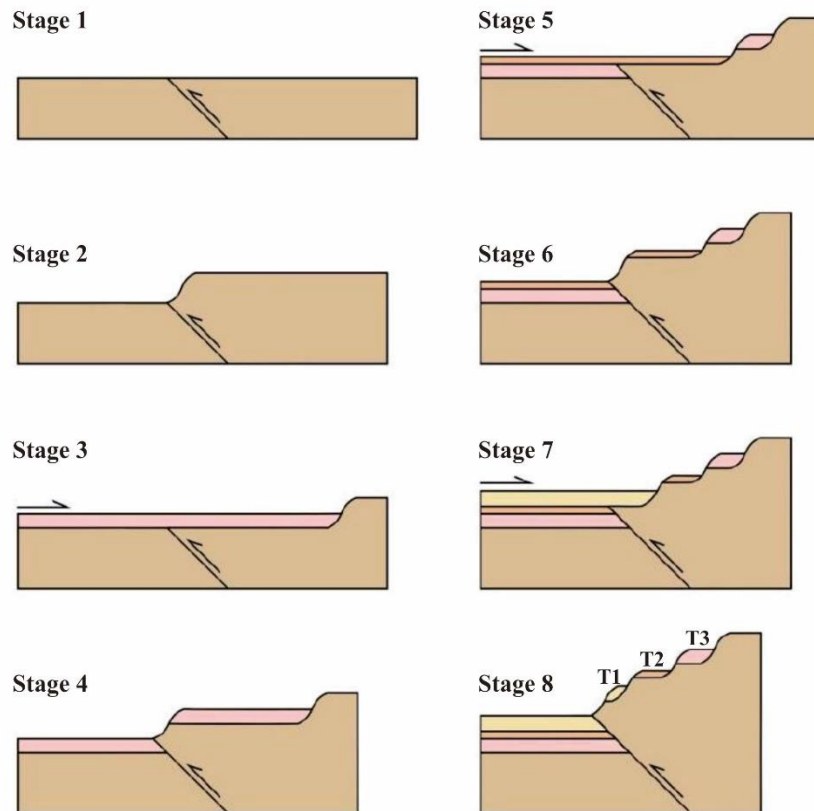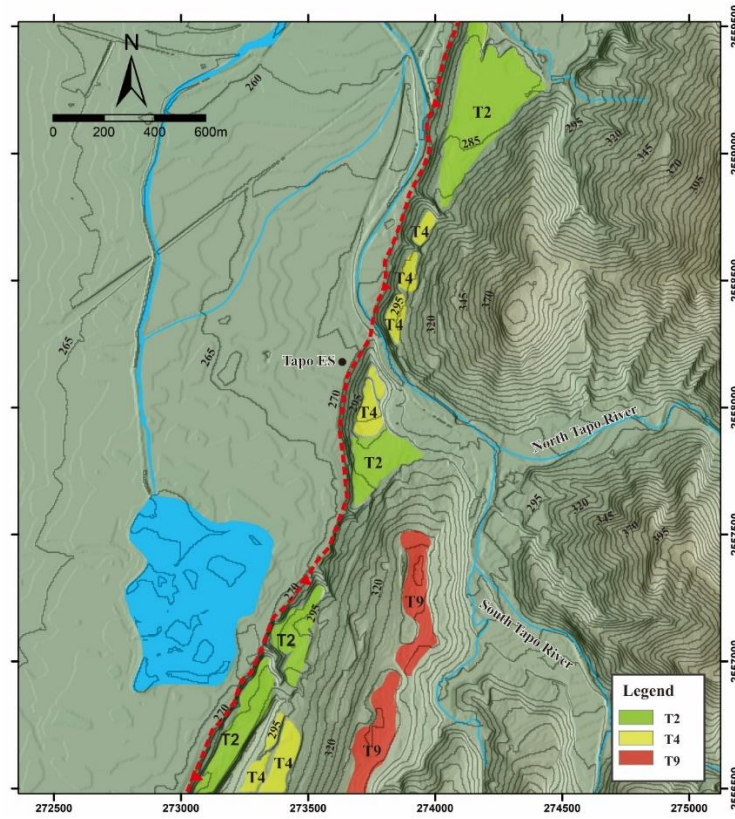
Figure 4.15 Map of terraces distribution along the Chihshang Fault with the schematic diagram of terrace formation mechanism (after Chang, Q., 2013).
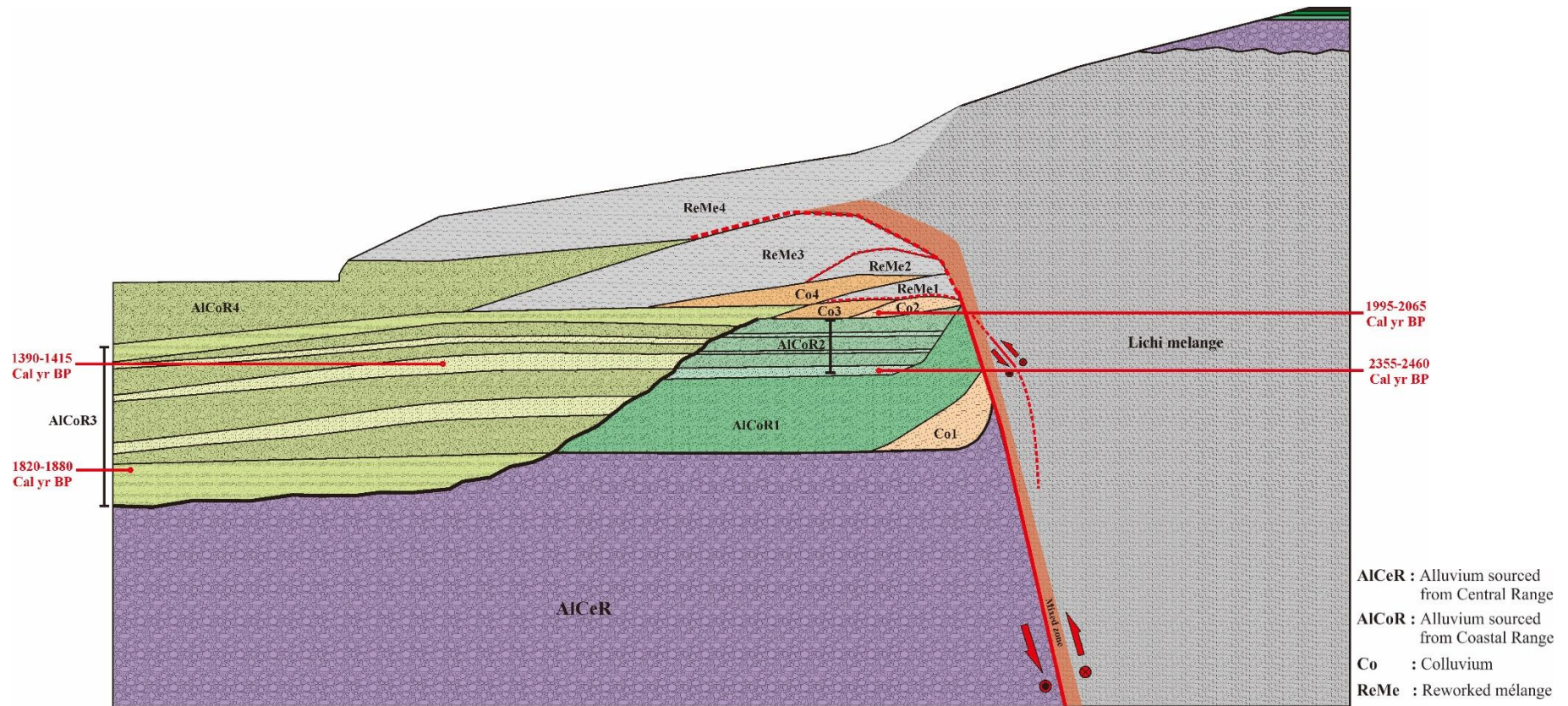
Figure 4.16 Diagrams of subsurface structure around the main Chihshang Fault with the core logs. The red line indicates the Chihshang Fault. The red arrows and the red circle with the symbol indicate the movement sense of the Chihshang Fault. The dot symbol in the red circle indicates the corresponding block relative to fault or sliding plane is moving outward the paper. The cross symbol in the red circle indicates the corresponding block relative to the fault or sliding plane is moving inward the paper. Red label indicates the dating data at the corresponding point.

Present day
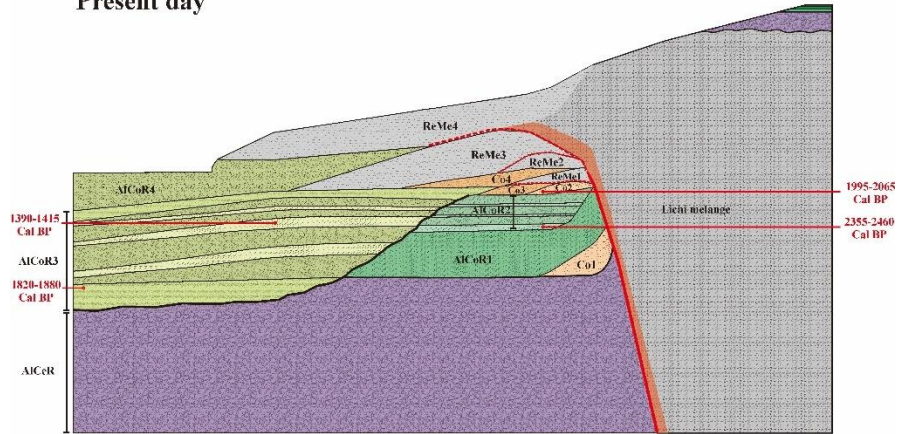
Restoration 1: Undoing the slumping
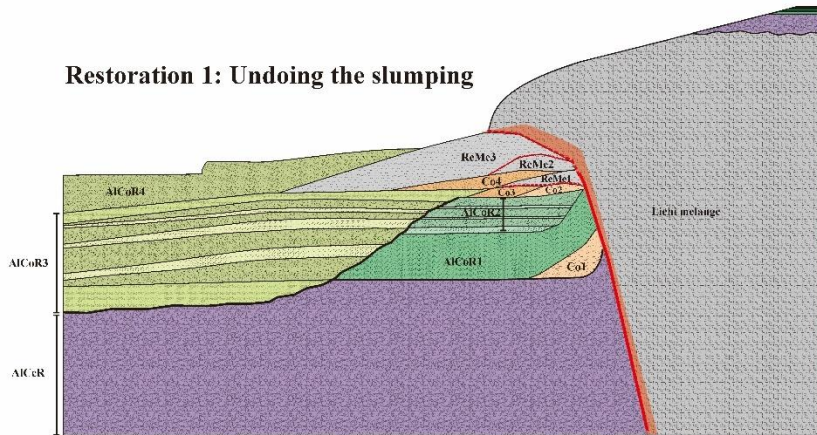
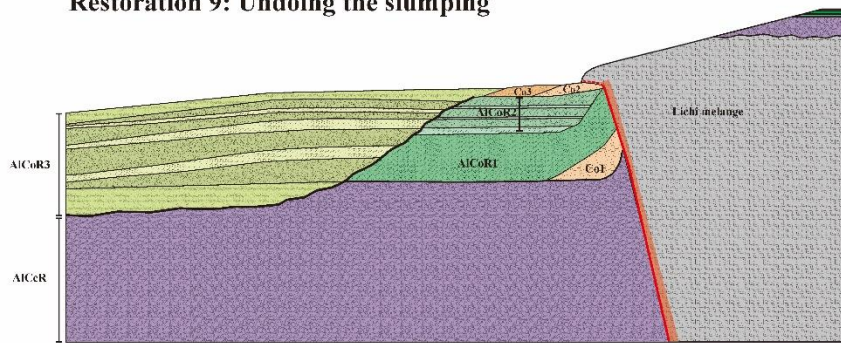**Restoration 2: Undoing the alluvium sourced from the Coastal Range**
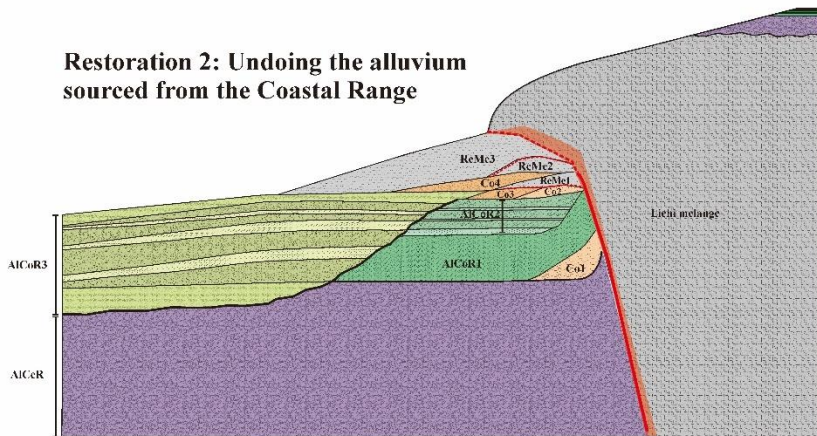
Restoration 3: Undoing the faulting
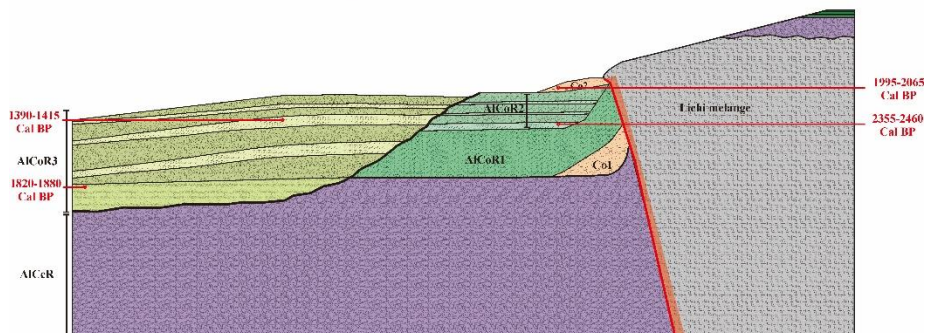
Restoration 4: Undoing the slumping

Restoration 5: Undoing the faulting

Restoration 6: Undoing the slumping

Restoration 7: Undoing the colluvium settlement
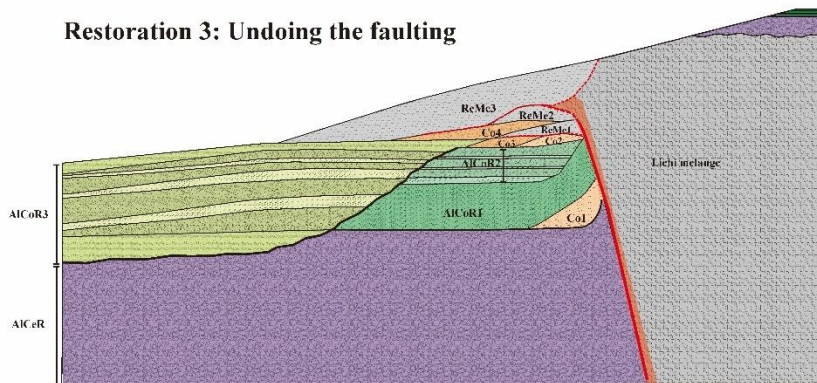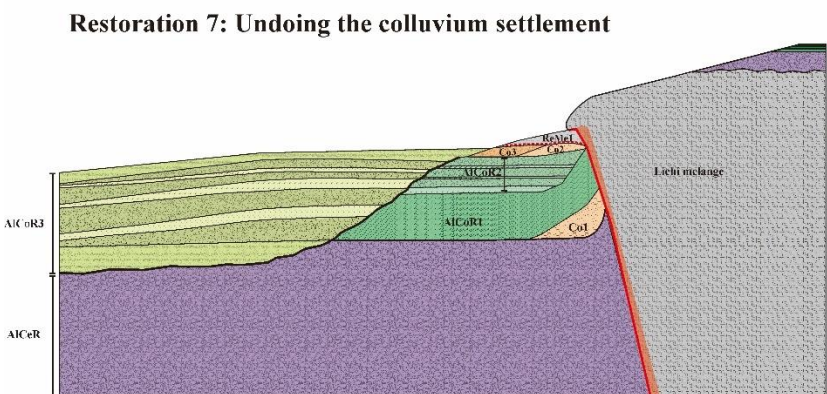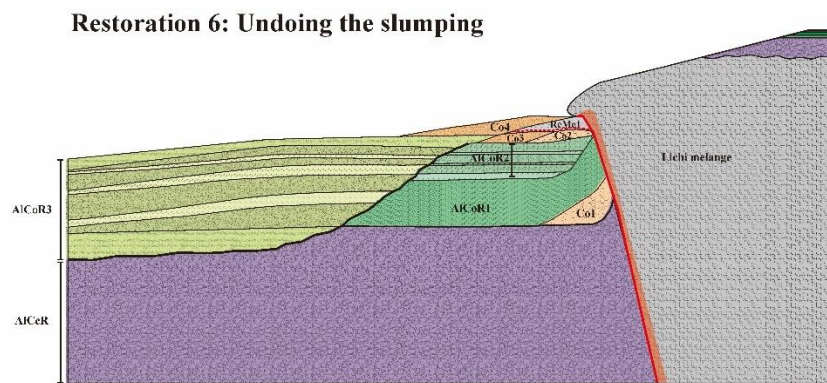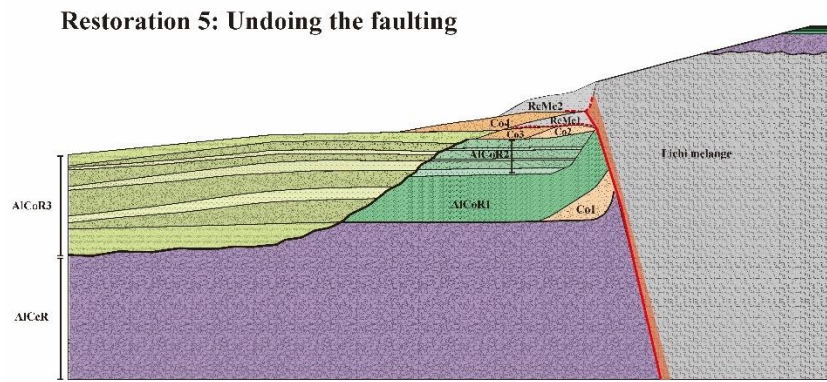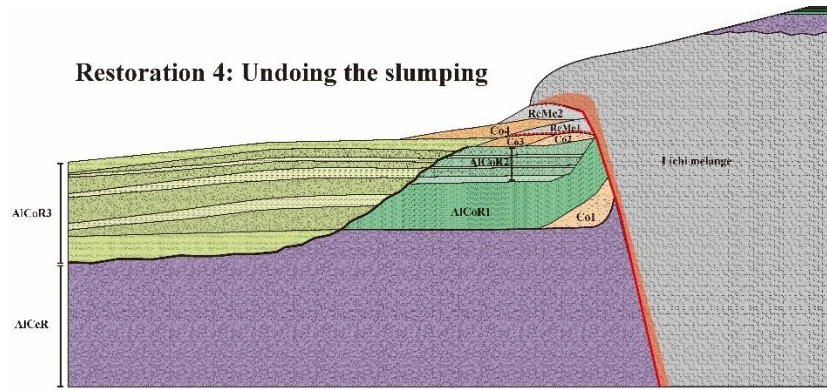
Restoration 8: Undoing the faulting
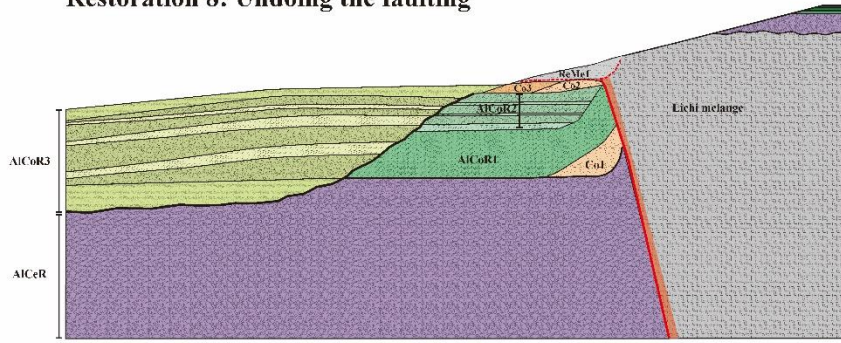
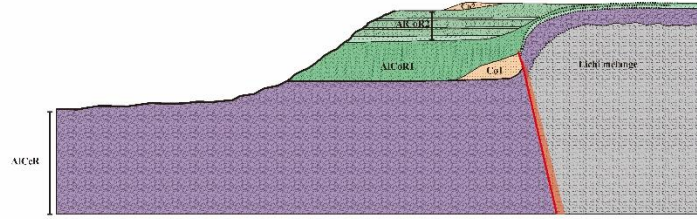**Restoration 9: Undoing the slumping**

Restoration 10: Undoing the alluvium settlement sourced from Coastal Range
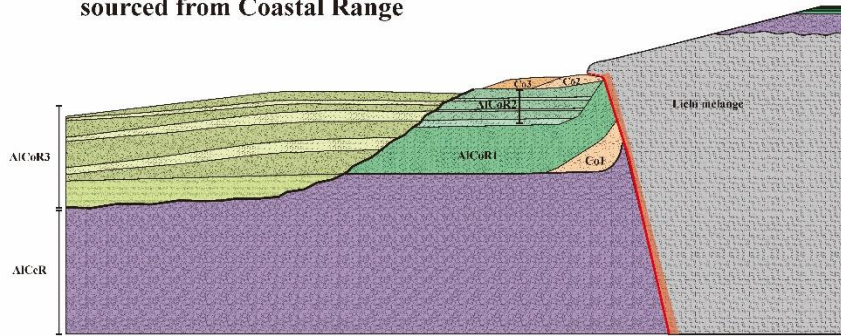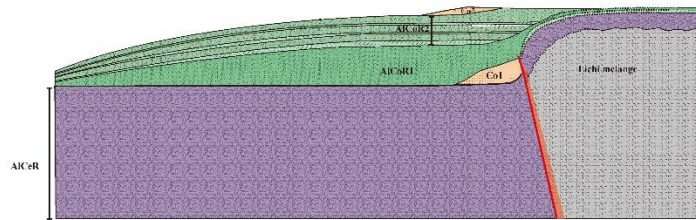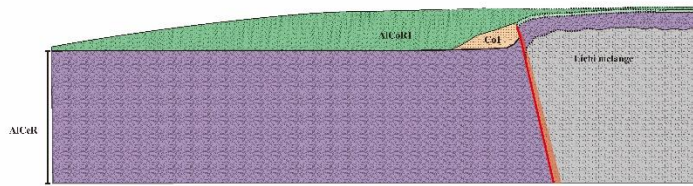

Restoration 11: Undoing the colluvium settlement

Restoration 12: Undoing the sequence of alluvium sourced from Coastal Range and undoing the uplifting of the hanging wall from 1390 to 1880 yr BP
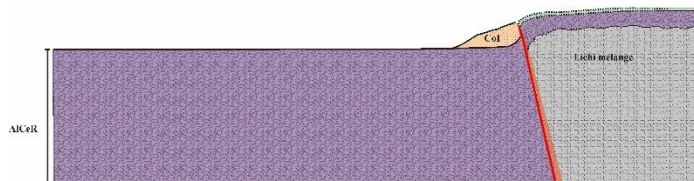
Restoration 13: Recovery the eroded part of the layers

Restoration 14: Undoing the sequence of alluvium sourced from Coastal Range

Restoration 15: Undoing the alluvium settlement sourced from Coastal Range

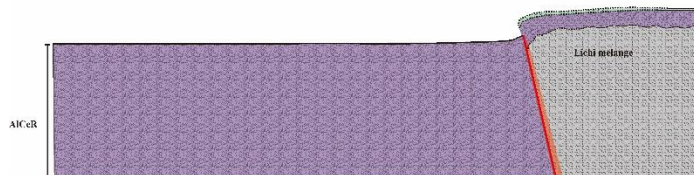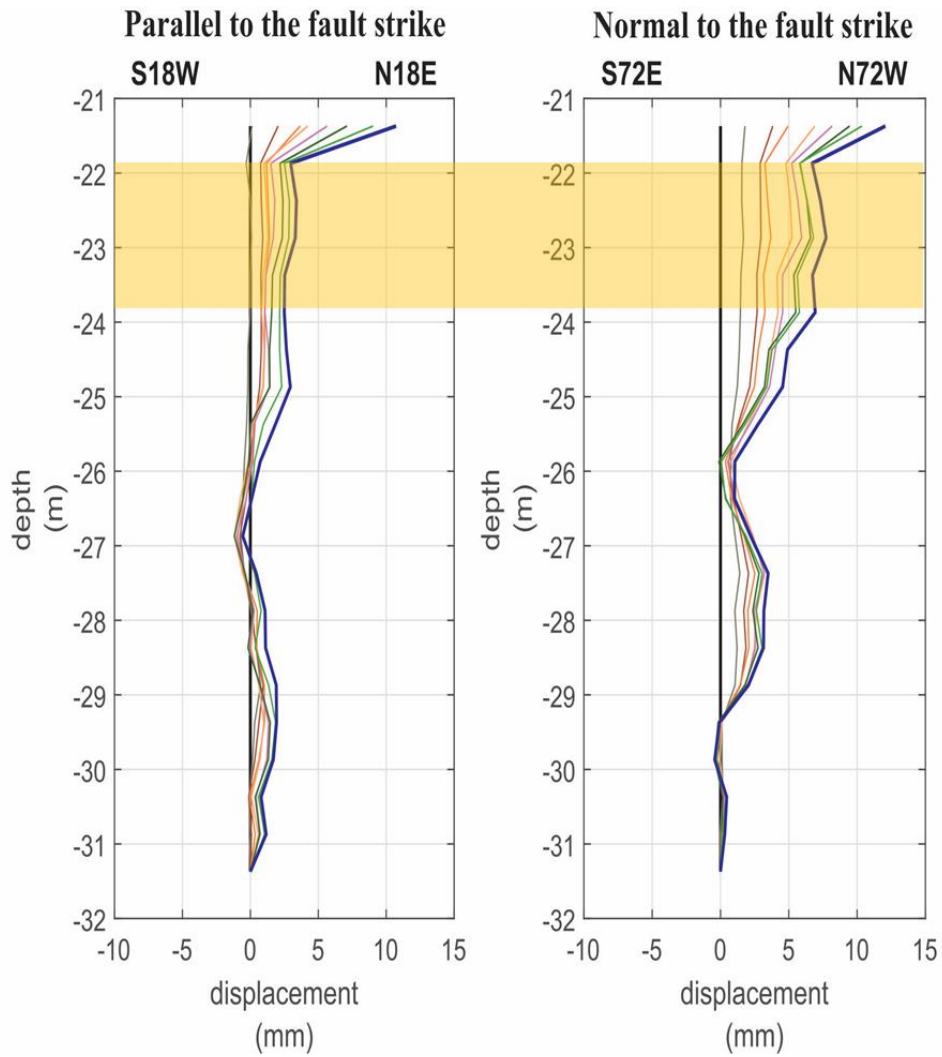**Restoration 16: Undoing the colluvial sand**

Figure 4.17 Schematic diagrams showing the reconstruction of Chihshang Fault evolution related to the major escarpment at Tapo ES area. Red dashed-line indicate the Chihshang main fault.
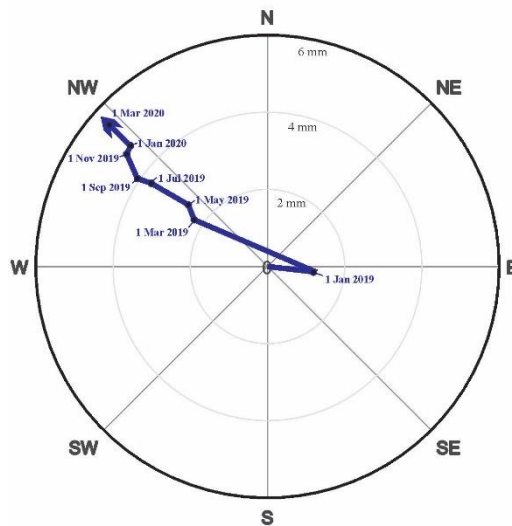
Figure 4.18 Graph of incremental displacement of inclinometer in DP-8 from November 2018 to March 2020. The yellow area indicates the consideration range of depth to approximate the uplift rate of Chihshang main fault.

Chapter 5: Conclusions

By the active movement during co-seismic and interseismic period, the Chihshang Fault may induce significant hazard in the eastern Taiwan. Tracing this main fault will be one of the important things to assess the hazard of the area. However, the study of the two boreholes, which are located on the hanging wall and footwall, respectively, of the inferred trace of Chihshang Fault, barely gives us any clues about the presence of the Chihshang main fault. Regarding to this issue, we aim to study three major topics; those are the trace of the Chihshang Fault, the characteristic of the Chihshang Fault, and the relation between the Chihshang Fault with the surface deformation that occurs at Tapo ES area.

To support this study, we utilized several methods: field observation, rock core observation, ERT survey, radiocarbon dating, and inclinometer monitoring. From the discussion of the result of each method, we conclude the three major conclusions as below:

1. At Tapo ES area, the Chihshang Fault is located of about 55 m to the east from the escarpment.

2. At Tapo ES area, the Chihshang Fault is defined as Lichi mélange that is thrusted over the Holocene deposits with dip angle of about 77º.

3. At Tapo ES area, two mechanisms, those are faulting and slumping, affect the ground surface deformation.

References

Angelier, J., H.T. Chu, J.C. Lee, 1997. Shear concentration in a collision zone: kinematics of the Chihshang Fault as revealed by outcrop-scale quantification of active faulting, Longitudinal Valley, eastern Taiwan. Tectonophysics, 274, 117-143. doi: 10.1016/S0040-1951(96)00301-0

Bird, M. I., 2013. Radiocarbon dating: charcoal. In: Encyclopedia of Quaternary Science. Eds: S. A. Elias, 4, 353-360. doi: 10.1016/B978-0-444-53643-e.00047-9

Biq, C. C., 1972. Dual-trench structure in the Taiwan-Luzon region. Proceeding of the Geological Society of China, 15, 65-75.

Chai, B. H. T, 1972. Structure and Tectonic Evolution of Taiwan. Am. J. Sci., 272, 389-422. doi: 10.1016/0040-1951(75)90090-6

Chang, C. P., J. Angelier, C. Y. Huang, 2000. Origin and evolution of mélange: the active plate boundary and suture zone of the Longitudinal Valley, Taiwan. Tectonophysics, 325, 43-62. doi: 10.1016/S0040-1951(00)00130-X

Chang, C.P., J. Angelier, C. Y. Huang, 2001. Structural evolution and significance of a mélange in a collision belt: the Lichi Mélange and the Taiwan arc-continent collision. In: Geol. Mag., 138, 633-651. Cambridge University Press. doi: 10.1017/S0016756801005970

Chang, P. Y., W. J. Huang, C. C. Chen, H. I. Hsu, I. C. Yen, G. R. Ho, J. C. Lee, … et al., 2018. Probing the frontal deformation zone of the Chihshang Fault with boreholes and high-resolution electrical resistivity imaging methods: A case study at the Dapo site in eastern Taiwan. J. Appl. Geophys., 153, 127-135. doi: 10.1016/j.jappgeo.2018.04.006

Chang, Q., 2013. Evolution of the Holocene Uplifted Terraces along the Chihshang Fault: Interactions between Tectonics Uplift and Fluvial Sedimentation. MS thesis, National of Taiwan University, 124 pp in Chinese with English abstract).

Chen, H. Y., S. B. Yu, L. C. Kuo, C. C. Liu, 2005. Coseismic and postseismic surface displacement of the 10 December 2003 (Mw 6.5), eastern Taiwan, earthquake. Earth Planet and Space, 58, 5-21. doi: 10.1186/BF03351908

Chen, W. S., 2008. The fault slip long-term velocity and recurrence period. In: Report of Central Geological Survey, pp. 31-40.

Cheng, S. N., Y. T. Yeh, M. S. Yu, 1996. The 1951 Taitung earthquake in Taiwan. Journal of the Geological Society of China, 39, 267-285.

Green, G. E., P. E. Mikkelsen, 1986, 1986. Measurement of ground movement with inclinometers. Proceedings of Fourth International Geotechnical Seminar on Field Instrumentation and In-Situ measurement. Pp 235-246.

Horne, G. S., 1970. Complex Volcanic-Sedimentary Patterns in the Magog Belt of Northeastern Newfoundland. Geol. Soc. Am. Bull., 81, 1767-1788.

Hsu, T. L., 1962. Recent Faulting in the Longitudinal Valley of Eastern Taiwan. Memoir of the Geological Society of China, 1, 95-102.

Hsu, Y.J., S. B. Yu, H. Y. Chen, 2009. Co-seismic and postseismic deformation associated with the 2003 Chengkung, Taiwan, earthquake. Geophys. J. Int., 176, 420-430. doi: 10.1111/j.1365-246X.2008.04009.x

Hsu, Y. J., Y. R. Lai, R. J. You, H. Y. Chen, L. S. Teng, Y. C. Tsai, C. H. Tang, H. H. Su, 2018. Detecting rock uplift across southern Taiwan mountain belt by integrated GPS and leveling data. Tectonophysics, 744, 275-284. doi: 10.1016/j.tecto.2018.07.012

Huang, W. H., 2000. Geologic Map of Taiwan. Central Geological Survey, Taiwan.

Jiang, Y. L., H. T. Chu, J. C. Lee, C. Y. Huang, 2012. Investigation and Characterization of Surface Ruptures and Deformation Zone of the Chihshang Fault, Eastern Taiwan. In: Report of Central Geological Survey, pp. 101-138.

Lee J. J., J. Angelier, H. T. Chu, J. C. Hu, F. S. Jeng, 2001. Monitoring active fault creep as a tool in seismic hazard mitigation. Insight from creepmeter study at Chihshang, Taiwan. C. R. Geoscience, 337, 1200-1207. doi: 10.1016/j.crte.2005.04.018

McCalpin, J. P., G. A. Carver, 2009. Paleoseismology of Compressional Tectonic Environments. Geophys. J. Int., 95, 327-330. doi: 10.1016/S0074-6142(09)95005-7

Mikkelsen, P. E., 2003. Advances in Inclinometer Data Analysis. Symposium on Field Measurements in Geomechanics, Norway.

Mu, C. H., J. Angelier, J. C. Lee, H. T. Chu, J. J. Dong, 2011. Structure and Holocene evolution of an active creeping thrust fault: The Chihshang fault at Chinyuan (Taiwan). J. Struct. Geol., 33, 743-755. doi: 10/1016/j.jsg.2011.01.015

Shyu, J. B. H., L. H. Chung, Y. G. Chen, J. C. Lee, K. Sieh, 2007. Re-evaluation of the surface ruptures of the November 1951 earthquake series in eastern Taiwan, and its neotectonics implications. J. Asian Earth Sci., 31, 317-331. doi: 10.1016/j.jseaes.2006.07.018

Slope Indicator Company. Digitilt Inclinometer Probe 50302599. Mukilteo Wash., 2011, 14 pp.

Stark, T. D., H. Choi, 2008. Slope inclinometers for landslides. Landslides, 5, 339-350. doi: 10.1007/s10346-008-0126-3

Tchalenko, J.S., 1970. Similarities between Shear Zones of Different Magnitudes. Geo. Soc. Am. Bull., 81, 1625-1640.

Telford, W. M., L. P. Geldart, R. E. Sheriff, 1990. Resistivity Methods. In: Applied Geophysics. Second Edition. Cambridge University Press, New York.

Tseng, Y.C., 2019. Paleoseismic study of Milun active fault in Hualien, eastern Taiwan. MS thesis, National Central University, 138 pp in Chinese with English abstract).

Yen, I. C., W. S. Chen, S. H. Sung, N. W. Huang, C. C. Yang, Y. C. Liu, C. W. Lin, 2014. Paleoseismological study on the Chihshang segment of the Longitudinal Valley Fault in eastern Taiwan. Central Geological Survey Special Publication, 28, 43-70 (in Chinese with English abstract).

Yu, S. B., C. C. Liu, 1989. Fault Creep on the Central Segment of the Longitudinal Valley Fault, Eastern Taiwan. Proceedings of the Geological Society of China, 32, 209-231.

Yu, M. S., S. N. Cheng, Y. T. Yeh, 1994. Segmentation of the Taitung Longitudinal Valley fault zone. Ti-Chih, 40, 97-120 (in Chinese with English abstract).

Zhang, B. Y., 2018. Survey the near ground deformation induced by active faulting. In: Report of Central Geological Survey, pp. 69-77.
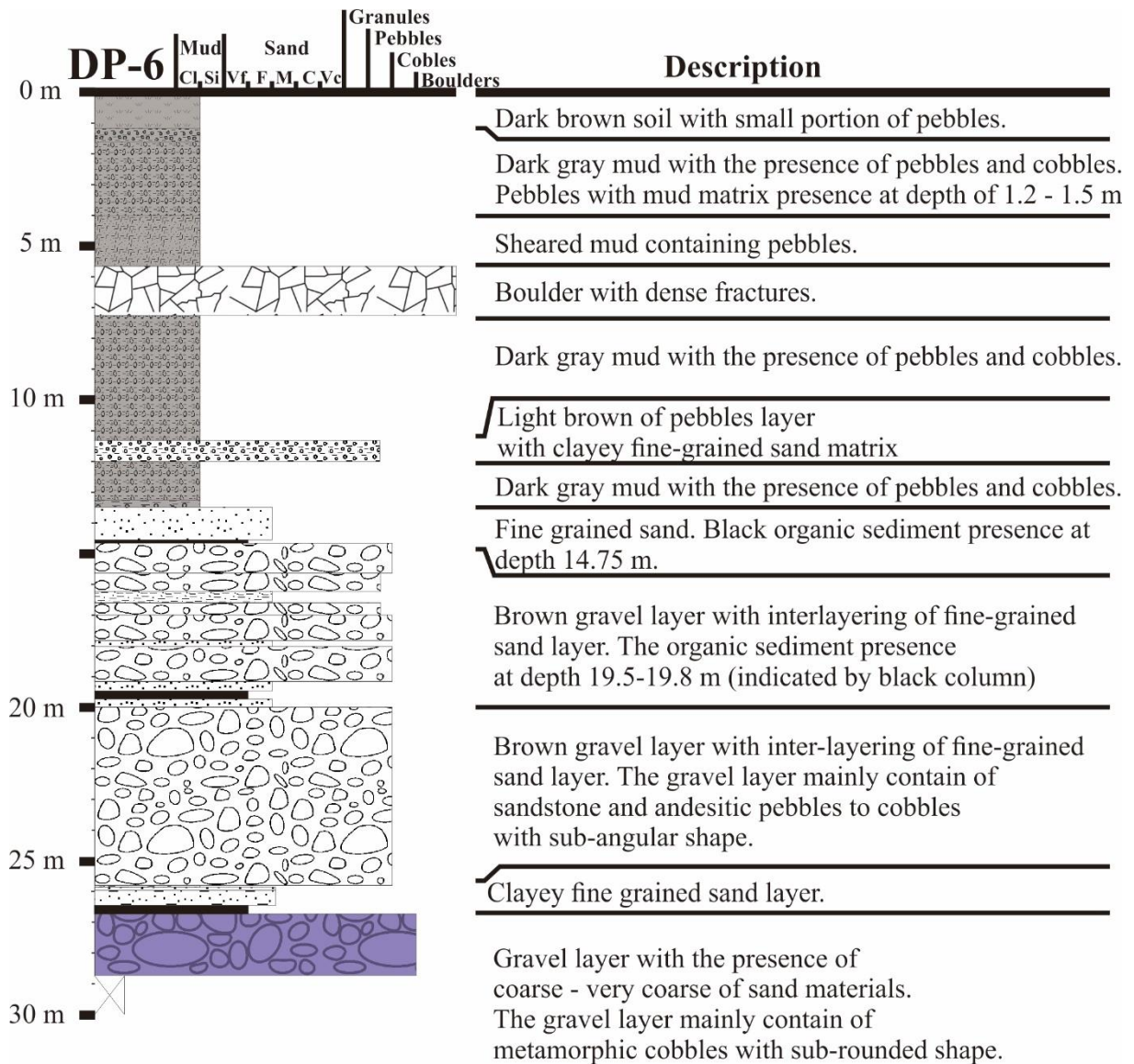
Appendixes

Figure A.1 Core logs of DP-6.

Figure A.2 Core images of DP-6 at depth 0 to 16 m. Each core has one-meter length.

Figure A.3 Core images of DP-6 at depth 16 to 28 m. Each core has one-meter length.
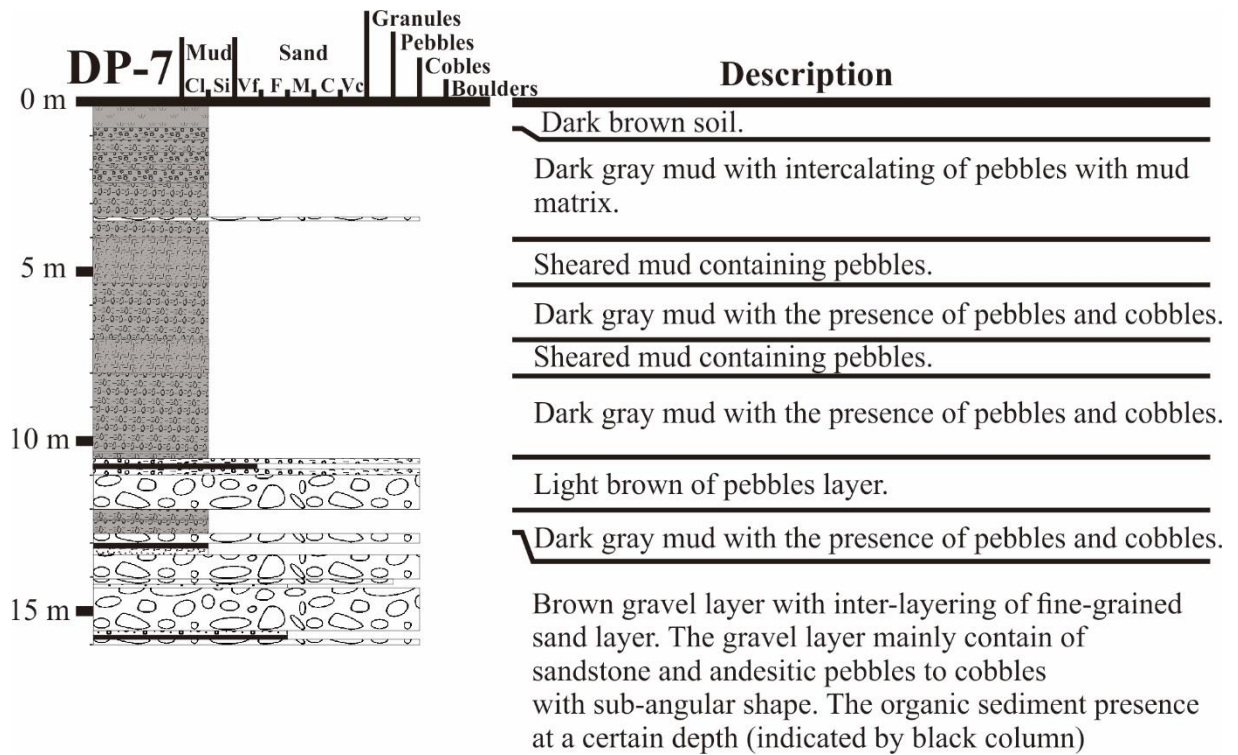
DP-7	Mud	Sand	Granules Pebbles Cobles Boulders	Description

DP-7

0 m

Mud
Cl Si

Sand
Vf F M C Vc

Granules
Pebbles
Cobles
Boulders

Description

Dark brown soil.

Dark gray mud with intercalating of pebbles with mud matrix.

5 m

Sheared mud containing pebbles.

Dark gray mud with the presence of pebbles and cobbles.

Sheared mud containing pebbles.

Dark gray mud with the presence of pebbles and cobbles.

10 m

Light brown of pebbles layer.

Dark gray mud with the presence of pebbles and cobbles.

15 m

Brown gravel layer with inter-layering of fine-grained sand layer. The gravel layer mainly contain of sandstone and andesitic pebbles to cobbles with sub-angular shape. The organic sediment presence at a certain depth (indicated by black column)

Figure A.4 Core logs of DP-7.

Figure A.5 Core image of DP-7 at depth 0 to 16 m. Each core has one-meter length.
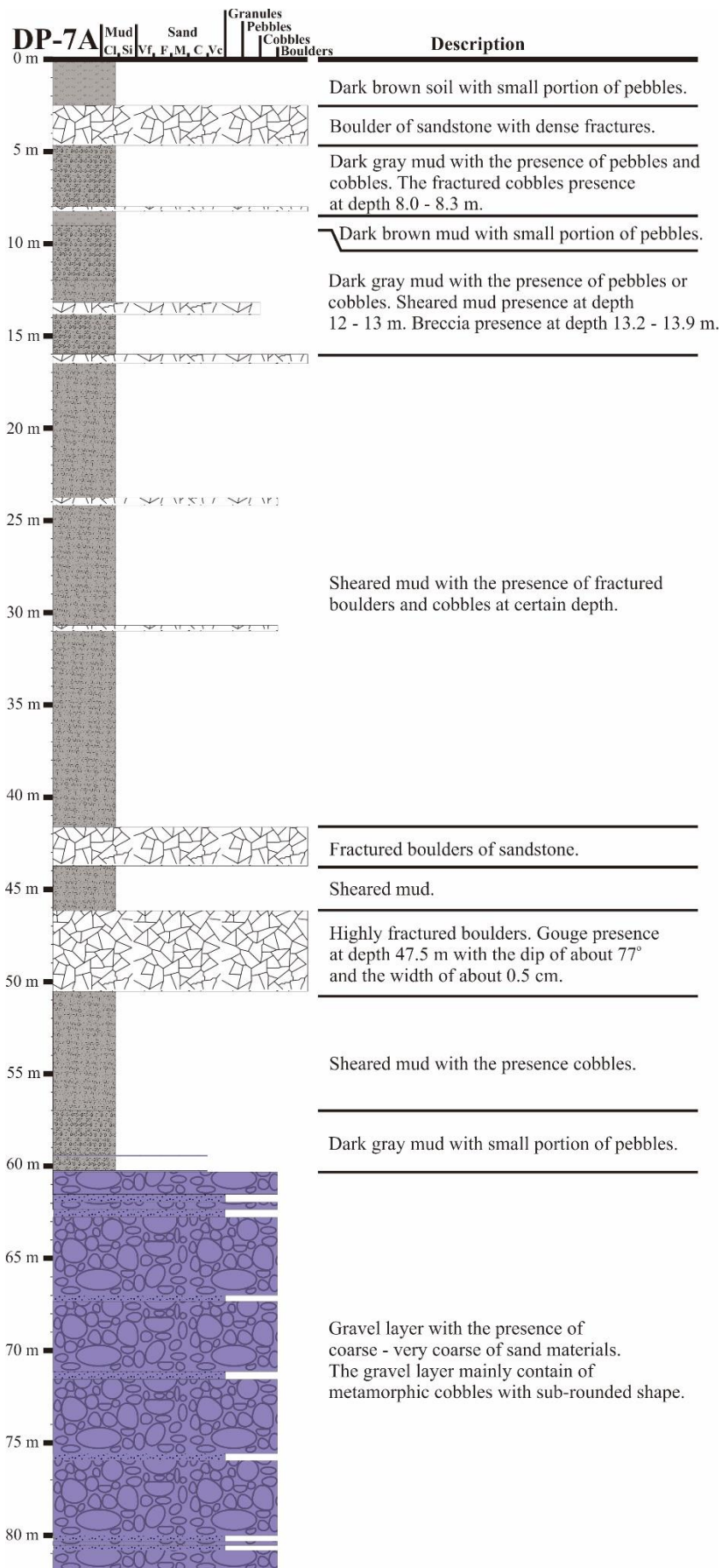
Figure A.6 Core logs of DP-7A.

Figure A.7 Core image of DP-7A at depth 0 to 16 m. Each core has one-meter length.

Figure A.8 Core image of DP-7A at depth 16 to 32 m. Each core has one-meter length.

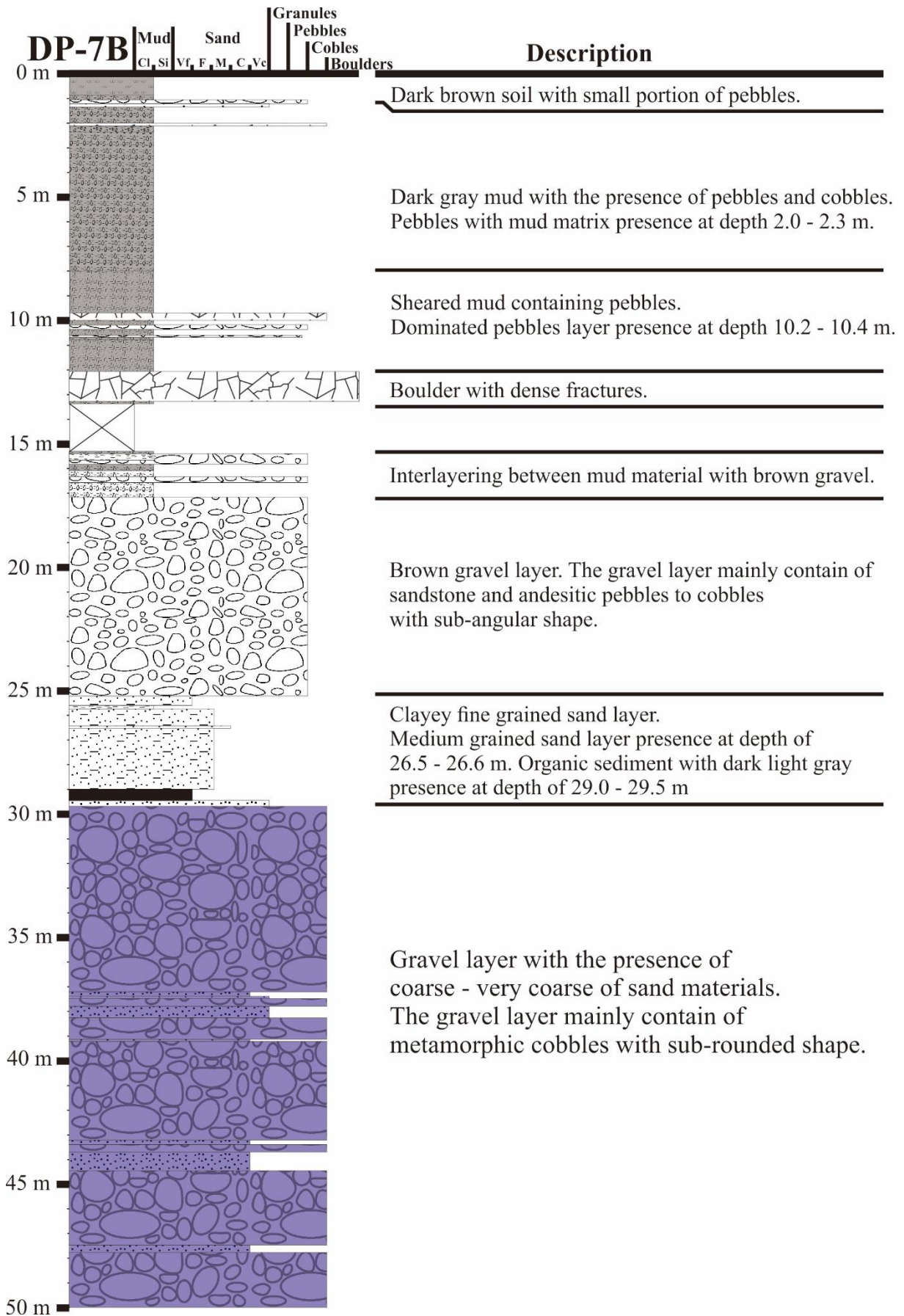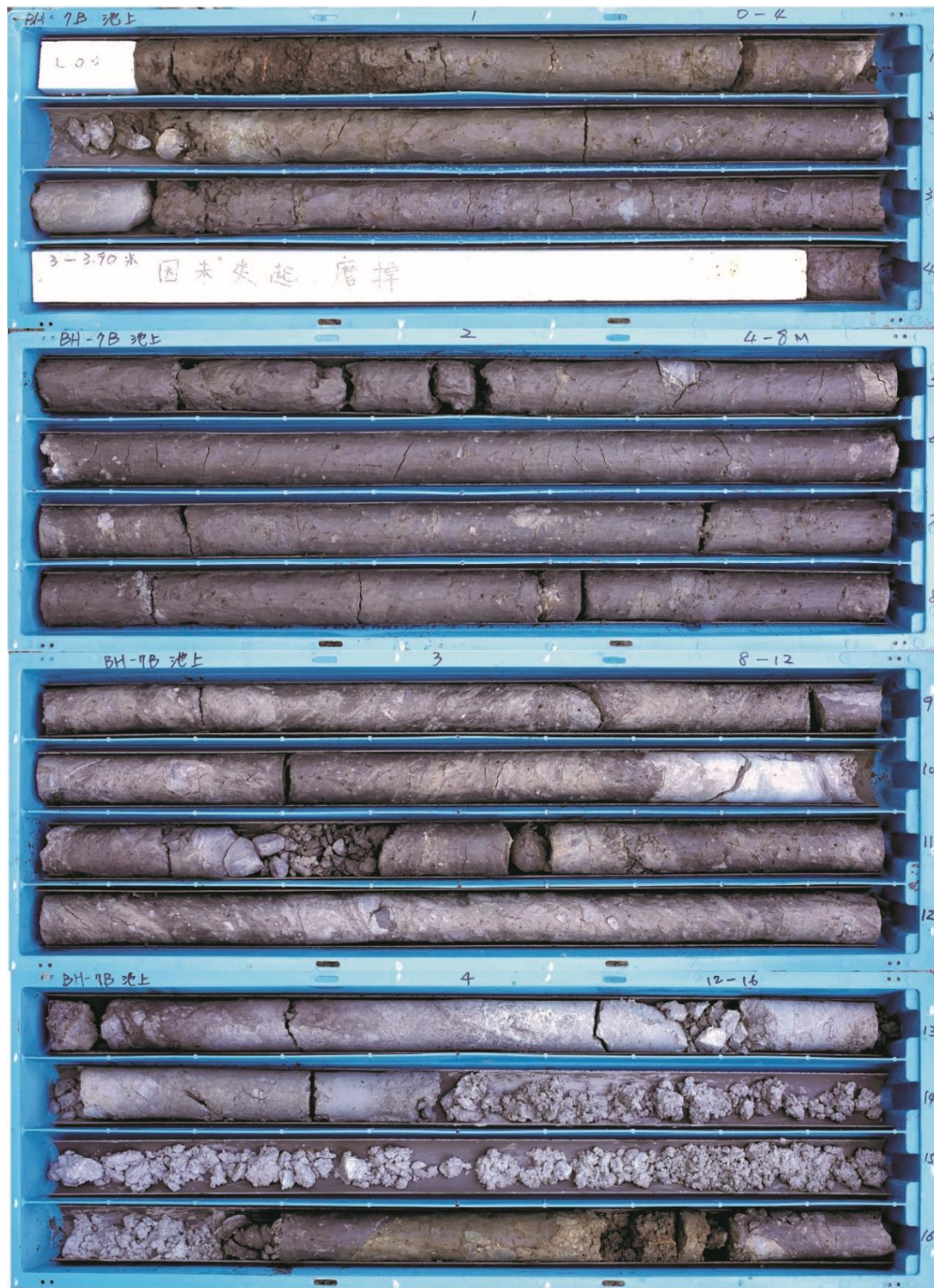Figure A.9 Core image of DP-7A at depth 32 to 48 m. Each core has one-meter length.

Figure A.10 Core image of DP-7A at depth 48 to 60 m. Each core has one-meter length.

Figure A.11 Core image of DP-7A at depth 60 to 72 m. Each core has one-meter length.

Figure A.12 Core image of DP-7A at depth 72 to 82 m. Each core has one-meter length.

DP-7B

Depth	Description
0 m	Dark brown soil with small portion of pebbles.
5 m	Dark gray mud with the presence of pebbles and cobbles. Pebbles with mud matrix presence at depth 2.0 - 2.3 m.
10 m	Sheared mud containing pebbles. Dominated pebbles layer presence at depth 10.2 - 10.4 m.
	Boulder with dense fractures.
15 m	Interlayering between mud material with brown gravel.
20 m	Brown gravel layer. The gravel layer mainly contain of sandstone and andesitic pebbles to cobbles with sub-angular shape.
25 m	Clayey fine grained sand layer. Medium grained sand layer presence at depth of 26.5 - 26.6 m. Organic sediment with dark light gray presence at depth of 29.0 - 29.5 m
30 m – 50 m	Gravel layer with the presence of coarse - very coarse of sand materials. The gravel layer mainly contain of metamorphic cobbles with sub-rounded shape.

Figure A.13 Core logs of DP-7B.

88

Figure A.14 Core image of DP-7B at depth 0 to 16 m. Each core has one-meter length.

Figure A.15 Core image of DP-7B at depth 16 to 28 m. Each core has one-meter length.
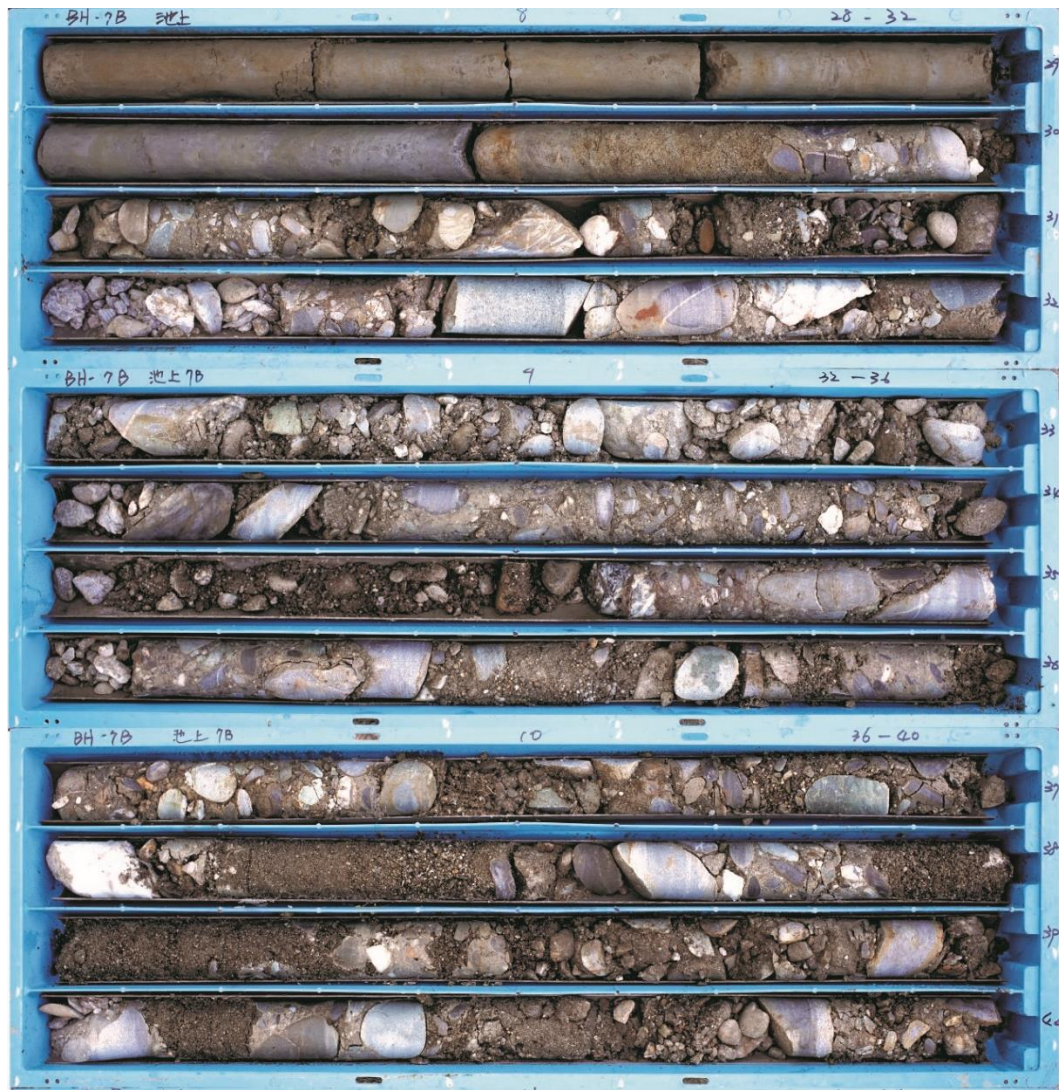
Figure A.16 Core image of DP-7B at depth 28 to 40 m. Each core has one-meter length.

Figure A.17 Core image of DP-7B at depth 40 to 50 m. Each core has one-meter length.
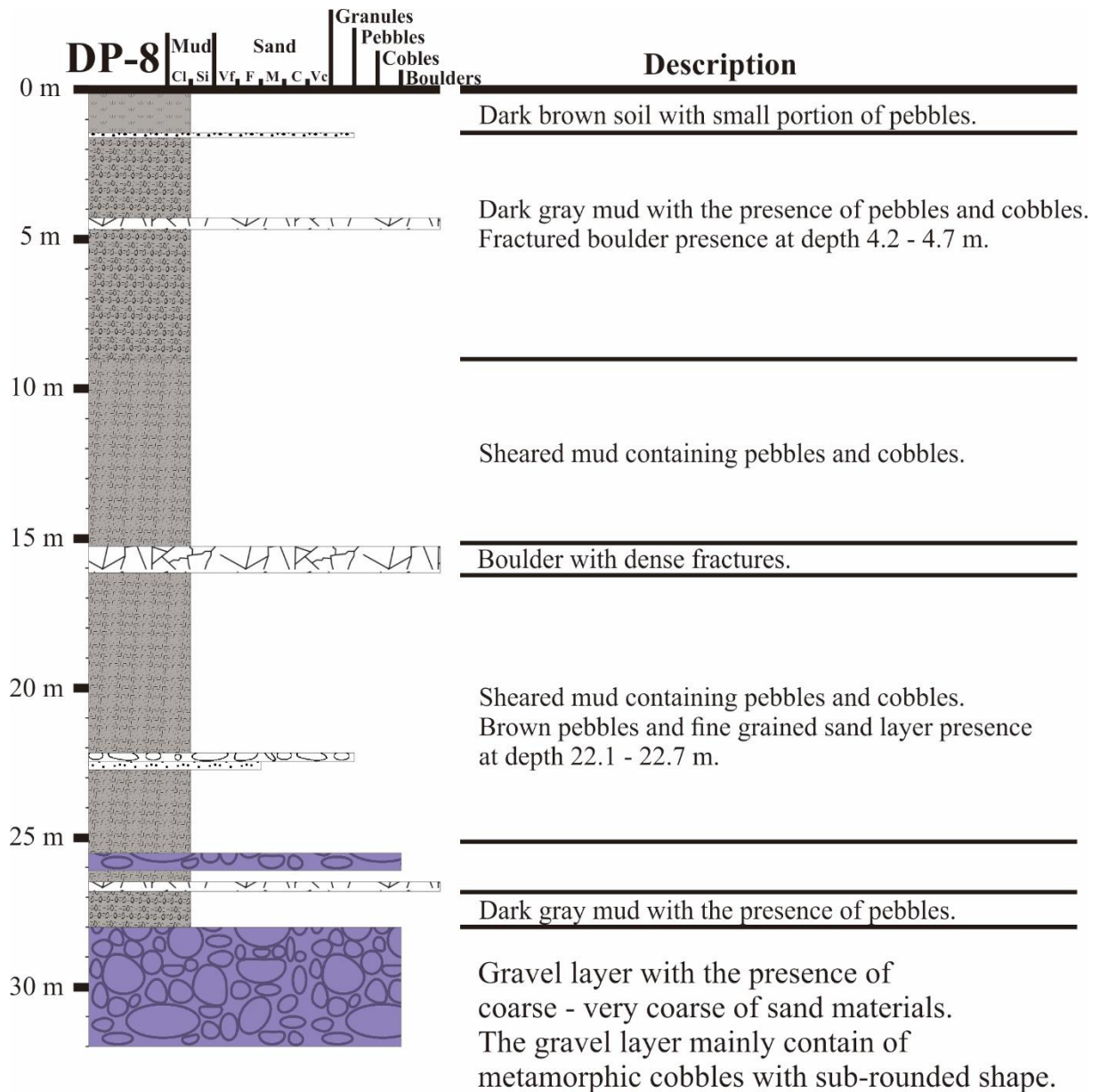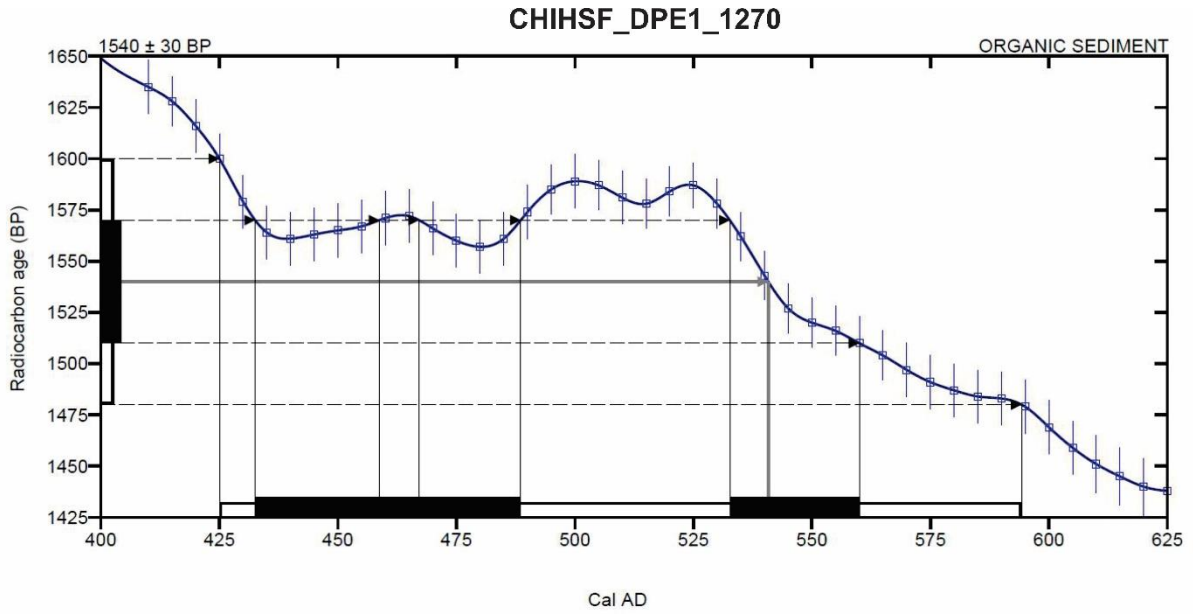
Figure A.18 Core logs of DP-8.

Figure A.19 Core image of DP-8 at depth 0 to 16 m. Each core has one-meter length.

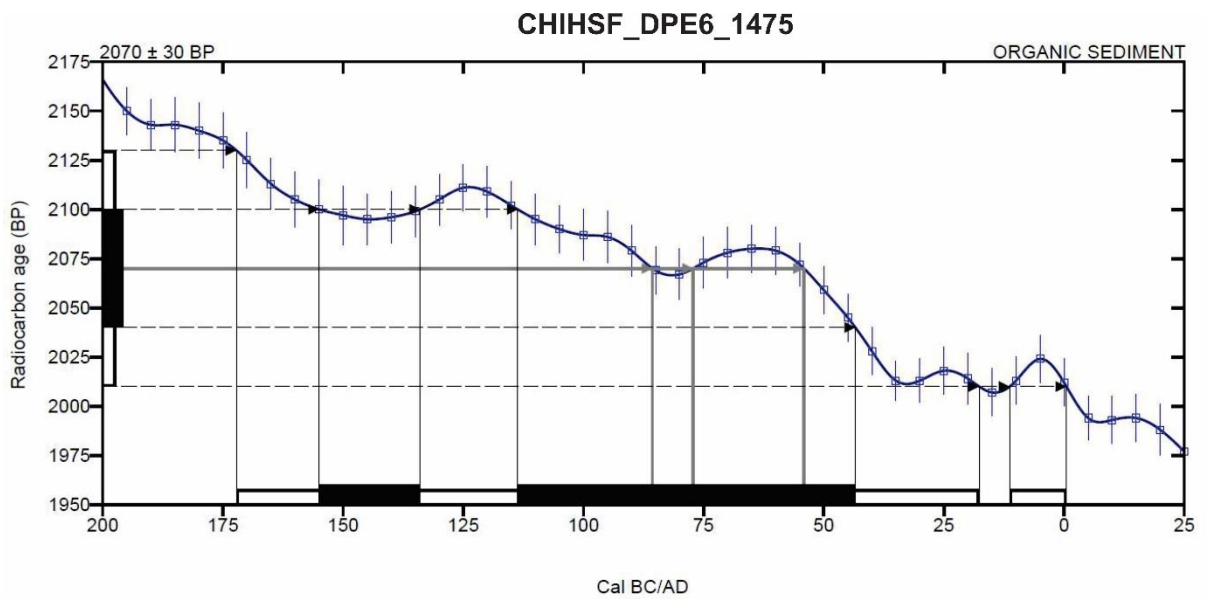Figure A.20 Core image of DP-8 at depth 16 to 32 m. Each core has one-meter length.

Figure A.21 Calibration of radiocarbon age of CHIHSF_DPE1_1270 based on INTCAL13 database.
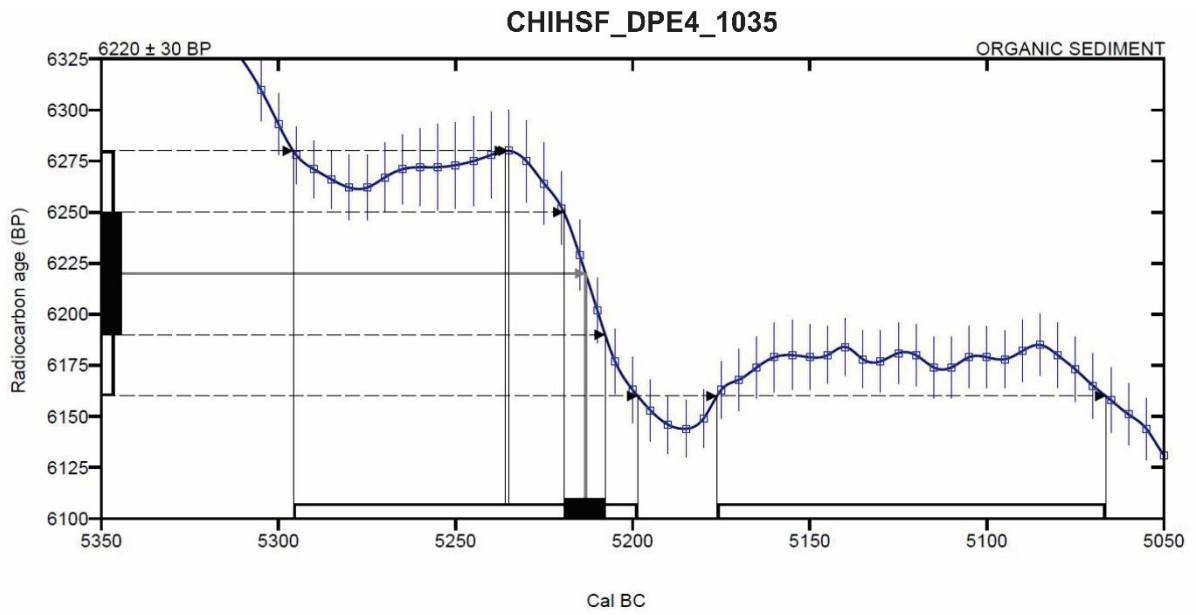
Figure A.22 Calibration of radiocarbon age of CHIHSF_DPE4_1035 based on INTCAL13 database.
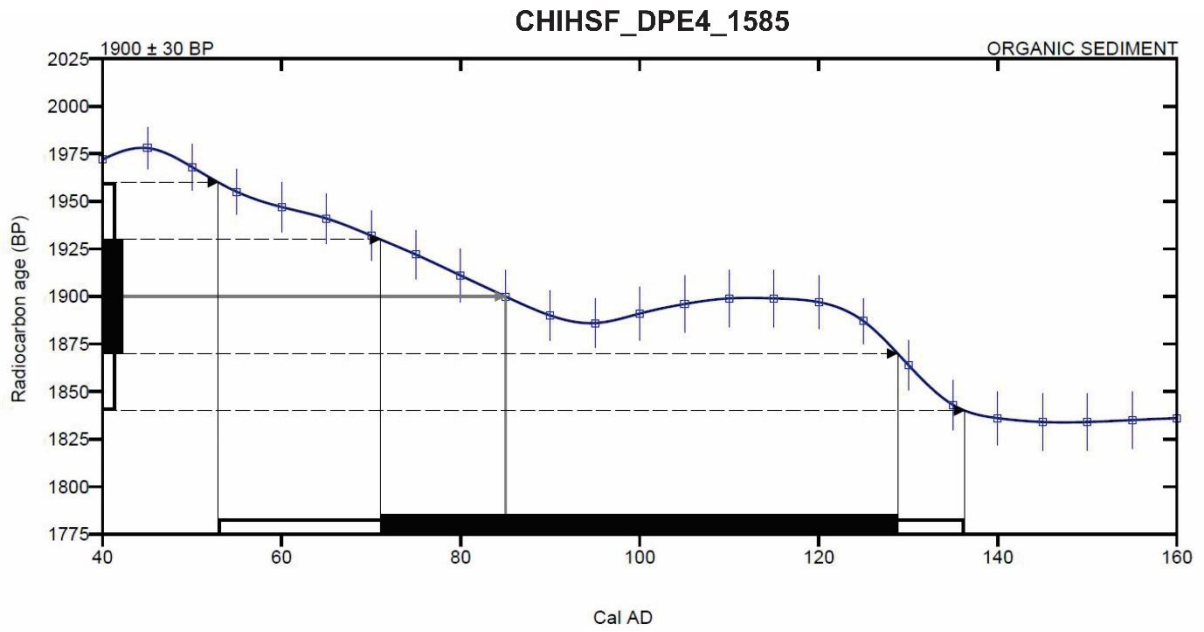
Figure A.23 Calibration of radiocarbon age of CHIHSF_DPE4_1585 based on INTCAL13 database.

Figure A.24 Calibration of radiocarbon age of CHIHSF_DPE6_1475 based on INTCAL13 database.
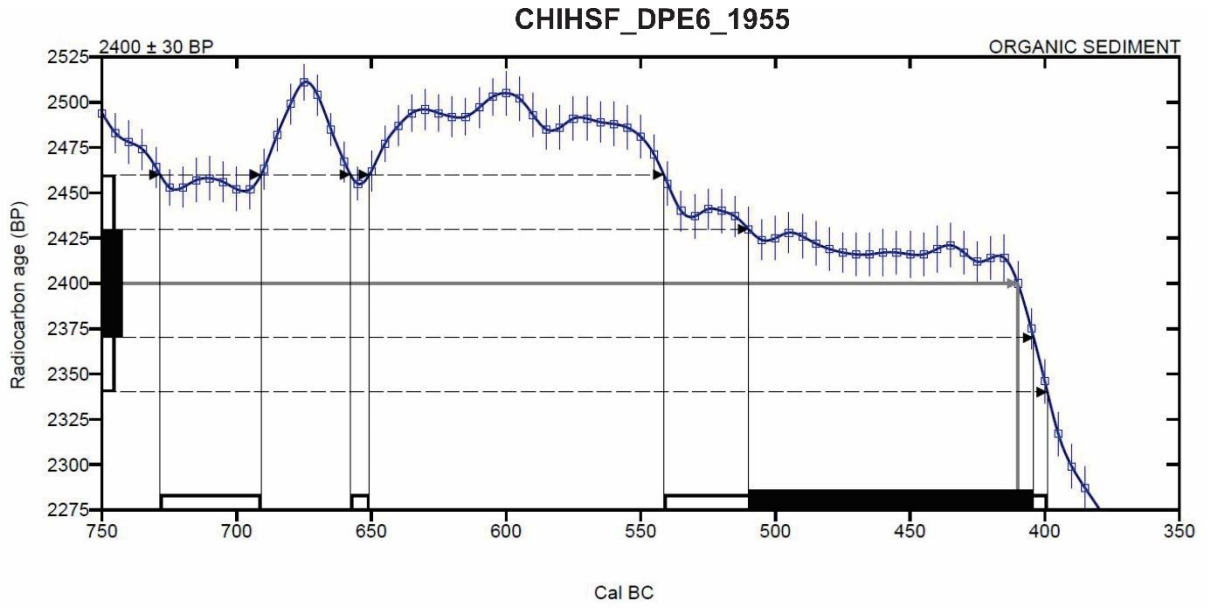
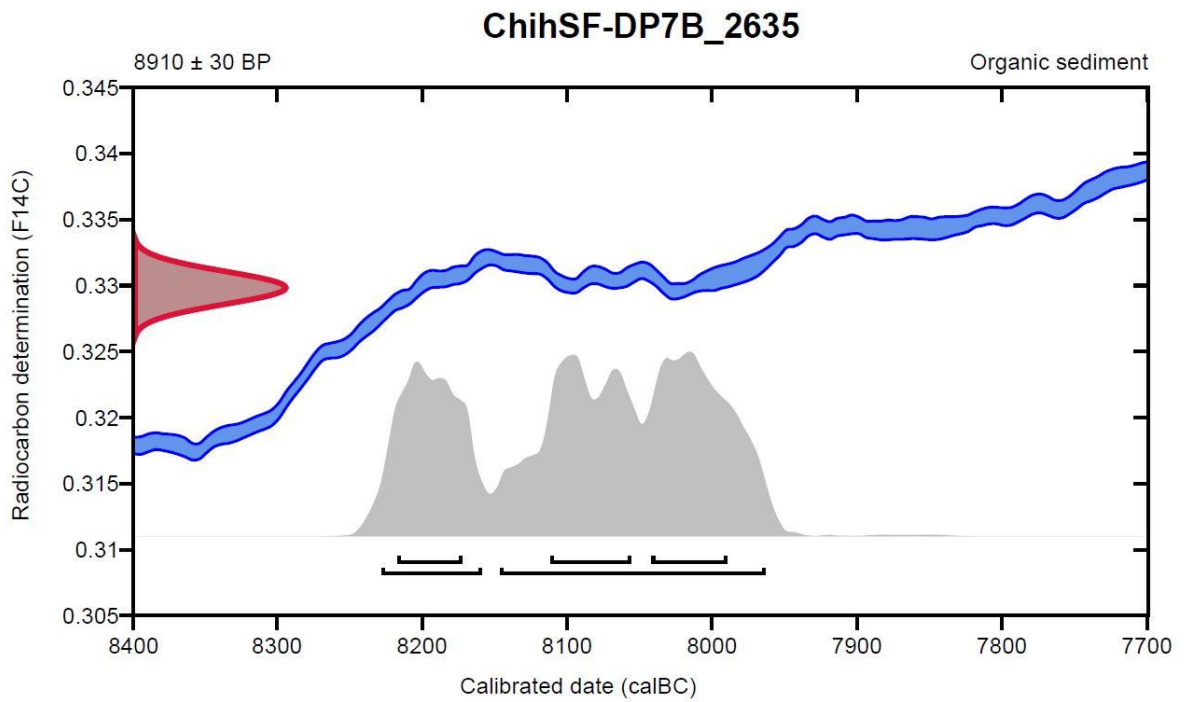Figure A.25 Calibration of radiocarbon age of CHIHSF_DPE6_1955 based on INTCAL13 database.

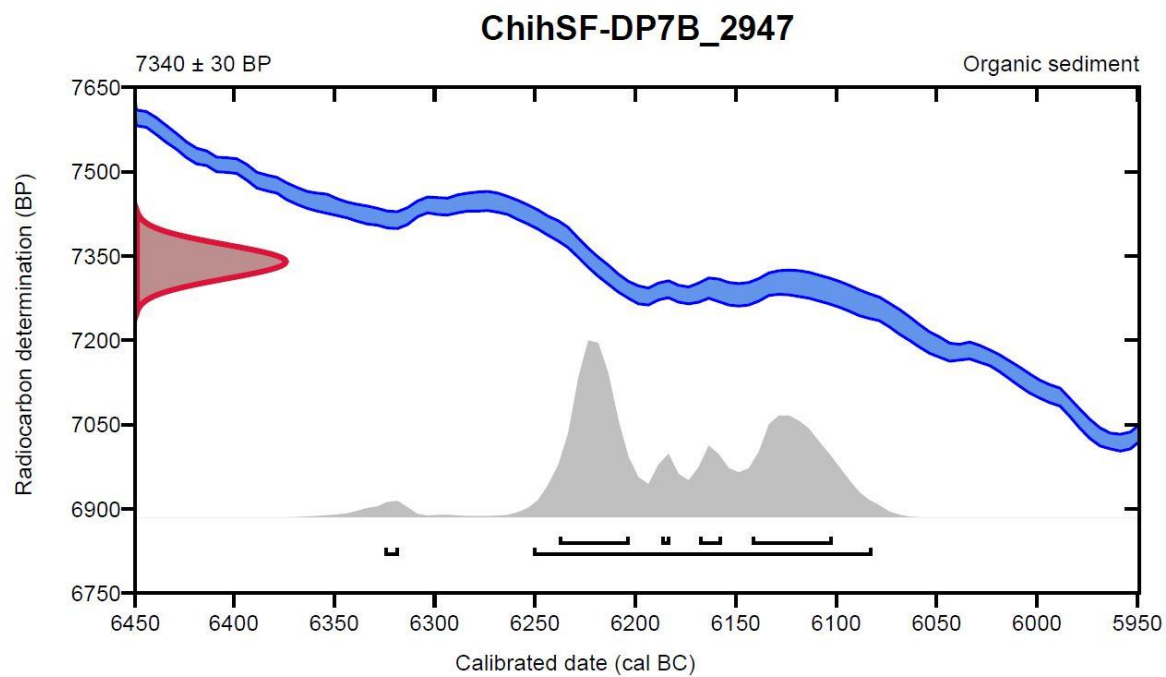Figure A.26 Calibration of radiocarbon age of CHIHSF_DP7B_2635 based on INTCAL13 + NHZ2 database.

Figure A.27 Calibration of radiocarbon age of CHIHSF_DP7B_2947 based on INTCAL13 database.